Doctorate Dissertation

Study on Solar Flare Trigger Process Based on Satellite Observations

Yumi BAMBA

Graduate School of Science,
Division of Particle and Astrophysical Science,
Institute for Space-Earth Environmental Research,
Nagoya University

Supervisor: Prof. Kanya Kusano

February, 2016

Abstract

Solar flares are explosive phenomena driven by magnetic energy stored in the solar corona. It is widely accepted that the magnetic reconnection plays an important role in the magnetic energy release process during flares. However, the physical process and the quantitative conditions to trigger flares are still veiled. Recently, Kusano & Bamba et al. [2012] proposed that two types of small magnetic disturbances, which appear near the polarity inversion line (PIL) of the sheared magnetic loops, as the likely triggers of solar flares, by three-dimensional magnetohydrodynamic (MHD) simulations. These small bipole fluxes are called the "flare trigger fields" and these can be the opposite of the major polarity (Opposite Polarity (OP) type) or reversed to the averaged magnetic shear (Reversed Shear (RS) type). This theoretical model (KB12 model) based on the numerical simulation has revealed the quantitative conditions using two simple and observable parameters: the global shear angle θ_0 in the flaring region and the azimuthal angles φ_e of the small-scale flare trigger field.

In this thesis, we aim to examine whether the quantitative parameters, those combinations, and the two-types of physical processes, which were proposed by the KB12 model, are suitable for flare triggering. We analyzed the several flare events, which were observed by Hinode/Solar Optical Telescope (SOT), Solar Dynamics Observatory (SDO)/Helioseismic and Magnetic Imager (HMI), Atmospheric Imaging Assembly (AIA), and Interface Region Imaging Spectrograph (IRIS). We measured the angles θ_0 and φ_e in the observed data, and compared the results to the flare trigger condition of the KB12 model. As a result, we

confirmed that there was no flare event, which occurred under the condition of "no-flare" in the KB12 model, and found that several events occurred with the conditions of either the OP- or RS-types. The most important observable feature to find out the flare trigger region is the pre-flare brightenings, which are seen on the PILs before the flare onset. We demonstrated that the flare trigger region can be identified using the pre-flare brightenings as a proxy, even in a very complicated active region (AR).

Moreover, we proposed that the "total magnetic flux" contained in the flare trigger field contributes to the critical conditions for flare triggering. We investigated the temporal evolution of the total magnetic flux of the trigger region, and found that it actually increased to the flare onset time. Therefore, our hypothesis is feasible because very small magnetic flux might not inject sufficient magnetic flux into the flux tube to destabilize it for flare onset. Furthermore, we found that the RS-type flare trigger is more flexible for the displacement of the flare trigger field from the PIL. It was consistent with our result of the statistical classification that more flares were triggered by the RS-type trigger than that by the OP-type.

Therefore, our conclusion of the thesis is that the KB12 model can explain the fundamental concepts of the physical process in flare triggering. We confirmed that the two geometrical parameters that characterize the photospheric magnetic field structures are suitable as the flare trigger conditions, and we further suggested another critical parameter for flare triggering. It is expected in the near future that the suitable parameters and the combinations of their values will be determined using the KB12 model for practicable solar flare forecast.

Acknowledgements

I would like to express my sincere gratitude to my supervisor in Nagoya University, Prof. Kanya Kusano, for his continuous guidance, constant encouragement, and endless patience during my PhD work. I am also deeply grateful to my advisor in Institute of Space and Astronautical Science/Japan Aerospace Exploration Agency (ISAS/JAXA), Prof. Toshifumi Shimizu, for kind supports and many suggestions of ideas.

My collaborators, Prof. Shinsuke Imada, Drs. Satoshi Inoue, Takenori Joten Okamoto, Daikou Shiota, Tetsuya Yamamoto, Yusuke Iida, and Shin Toriumi, gave me insightful comments and suggestions. My distinguished colleagues in Institute for Space-Earth Environmental Research (ISEE)/ Nagoya University and in ISAS/JAXA helped me in various ways. Valuable discussions, technical supports of Hinode data analysis, and even usual conversations inspired and encouraged me very much. Especially, Drs. Takuya Hara, Kyoko Watanabe, David H. Brooks, Kyoung-Sun Lee, and Mr. Yuki Tanaka mentally supported me every time. I received generous supports from secretaries and clerical staffs in ISEE and ISAS. I special thanks for their five years continual supports to Mrs. Motoko Kunieda and Miss. Tae Torii, who is a secretary and a clerical staff in ISEE.

During my PhD years, I had a lot of useful discussions with professors, researchers, and students in National Astronomical Observatory of Japan (NAOJ), ISAS, Lockheed-Martin Solar and Astrophysics Laboratory (LMSAL), National

Finally, I would like to express my special appreciation to my family for their continuous supports. I had not imagined that my PhD years become this fruitful. I think, I am never a brilliant student but I have tenacity. I had faced a lot of hard situation that is troublesome enough to make me want to cry, but finally I overcome hardship with many supports from above mentioned people. Without their help, it could not be possible to complete the dissertation and to continue to strive for my PhD work.

Contents

List of Figures

List of Tables

Chapter 1

General Introduction

In this chapter, we briefly introduce the general view of solar flares. In particular, we describe several theoretical models of solar eruptions, including the KB12 model, which is proposed by Kusano & Bamba et al. [2012] and is the focus of this thesis. We then raise questions that are studied in the thesis.

1.1 Solar Flares

Solar flares were first discovered as an enhancement in white light by R. C. Carrington and R. Hodgson in 1859 (Carrington [1859]; Hodgson [1859]). Later, G. E. Hale discovered the solar magnetic field in 1908 (Hale [1908]) and the relationship between the solar magnetic field and solar activity such as flares was extensively investigated. It is widely accepted that solar flares are explosive phenomena that release the magnetic energy stored in the solar corona mainly as thermal and kinetic energy of the plasma. The typical spatial size, duration, and released energy of a flare is about 10^9 cm, $10^3 \sim 10^4$ $sec.$, and $10^{28} \sim 10^{32}$ erg, respectively. Flares usually occur in ARs, and the magnetic energy stored in an

AR is estimated as follows:

$$E_{mag} \simeq \frac{B^2}{8\pi}L^3 \simeq 10^{33}\left(\frac{B}{10^3 \text{ G}}\right)^2\left(\frac{L}{3 \times 10^9 \text{ cm}}\right)^3 \quad [\text{erg}]$$

Here, we assumed a typical spatial scale of an AR: $L \sim 3 \times 10^9$ cm, and averaged the magnetic field strength over an AR: $B \sim 10^3$ G. This indicates that the magnetic energy stored in an AR is sufficient to be an energy source of flares. The scale of flares is defined by soft X-ray (1 - 8 Å) intensity measured by the Geostationary Operational Environmental Satellite (GOES), as summarized in Table 1.1.

Class	Soft X-ray Intensity ($erg \ cm^{-2} \ s^{-1}$)
A	10^{-5}
B	10^{-4}
C	10^{-3}
M	10^{-2}
X	10^{-1}

Table 1.1: The definition of scale of flares by GOES soft X-ray (1 - 8 Å) intensity

From the observations of satellites such as Hinotori (ASTRO-A, Tanaka [1983]) and Yohkoh (SOLAR-A, Ogawara et al. [1992]), it was suggested that magnetic reconnection plays an important role in the magnetic energy release process during flares. Magnetic reconnection is a topological change in the configuration of magnetic field lines, which occurs by electric current dissipation between antiparallel magnetic field lines. The observed features such as a cusp-shaped structure in the corona (Tsuneta et al. [1992]), a hard X-ray source above flare loop-top (Masuda et al. [1994]), plasmoid ejection (Ohyama & Shibata [1998]), and reconnection inflow (Yokoyama et al. [2001]) could be explained by the CSHKP model, which describes the scenario of flares based on magnetic reconnection.

The CSHKP model was named by taking the first letter of H. Carmichael (Carmichael [1964]), P. A. Sturrock (Sturrock [1966]), T. Hirayama (Hirayama [1974]), R. A. Kopp and G. W. Pneuman (Kopp & Pneuman [1976]) in recognition of their pioneering works, in the field. It is now considered a standard flare model, and it generally describes flares as follows and as illustrated in Figure 1.1. First, magnetic reconnection occurs in the solar corona and the stored magnetic energy is released. The coronal plasma is heated and accelerated at that time, and these plasma propagate down into the chromosphere (and photosphere), along the magnetic field lines. The chromospheric plasma is heated and strong brightenings are observed at the foot points of magnetic field lines, such as Hα line or Ca Ⅱ H line (as seen in Figure 1.2). These strong brightenings are called flare ribbons, and propagate on the outer side as magnetic reconnection propagates to outer magnetic field lines. The heated chromospheric plasma goes upward because it has higher gas pressure than that in the corona, and hot plasma fills the magnetic loop in the corona. This is called chromospheric evaporation (Antonucci et al. [1982, 1984]). The coronal magnetic loops, which are filled by dense and hot plasma by chromospheric evaporation, are observed as cusp-shaped flare loops in the X-ray band. Moreover, plasmoids and filaments are sometimes (but not always) ejected into space, and this sometimes causes coronal mass ejections (CMEs). According to the statistical report of Yashiro et al. [2006], the CME association rate of flares clearly increased with their peak soft X-ray flux.

Thus, the overview of flares is now widely accepted. However, the details of several aspects related to flares are still veiled, such as the energy storage process, elementary process of magnetic reconnection, particle acceleration process, and triggering process. In this thesis, we focus on the flare trigger process, which is one of the biggest problems in solar physics.
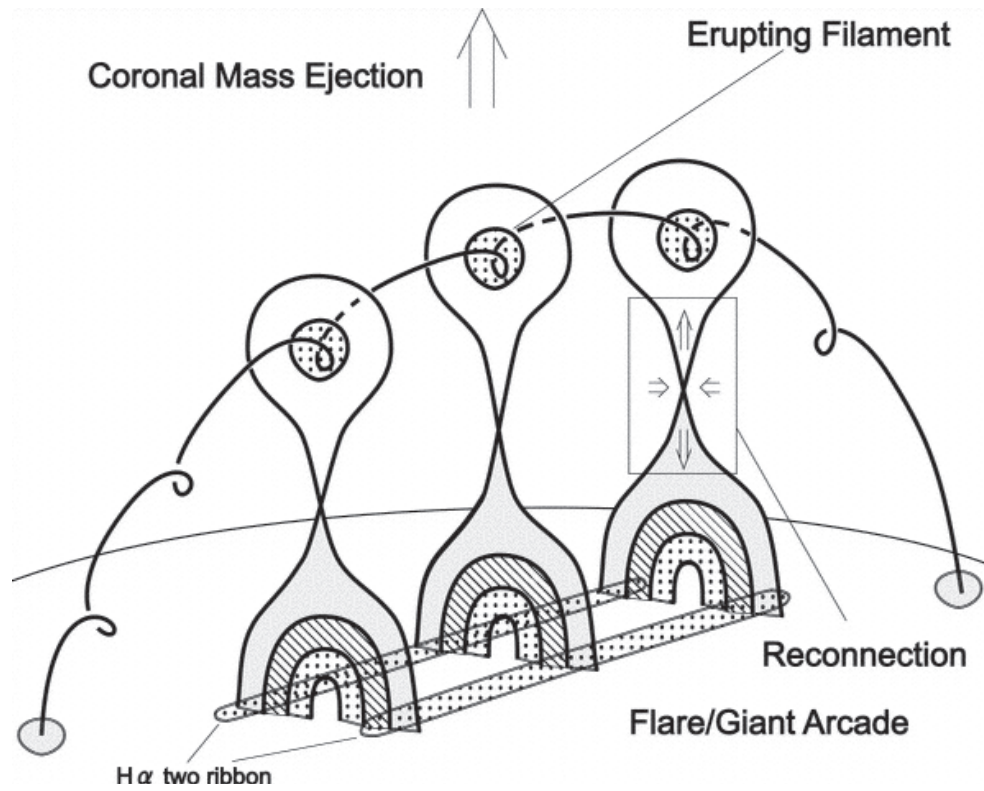
Figure 1.1: Schematic of the CSHKP model (reprinted from Shiota et al. [2005])
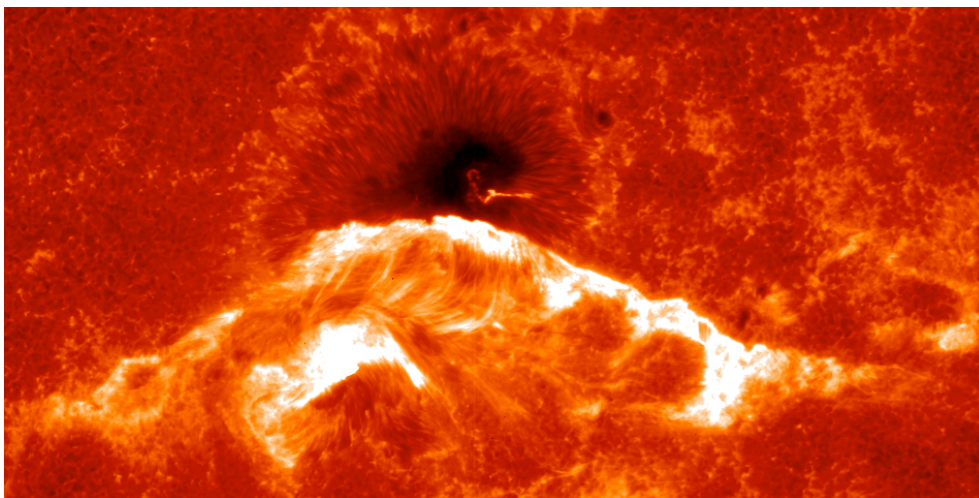
Figure 1.2: Flare ribbons of the X3.4 flare on 2006 December 13, which was taken in the Ca II H line by the Hinode satellite.

1.2 Loss-of-equilibrium and Loss-of-stability

Solar explosive and eruptive phenomena such as flares and CMEs are caused by "loss-of-equilibrium" and "loss-of-stability". Figure 1.3 illustrates the various equilibrium states: (a) stable equilibrium, (b) metastable, (c) unstable equilibrium, and (d) loss-of-equilibrium. In an equilibrium state, the system is at an equilibrium point in which the net force acting on an object equals to zero. Loss of equilibrium means that the equilibrium point is lost by some cause. In contrast, loss of stability means that the system is away from an equilibrium state with even small disturbances.

On the solar surface, a potential magnetic field structure is in stable equilibrium (state (a) in Figure 1.3). Flares and CMEs do not occur under this state because there is no free energy that can be released. State (b), metastable, is equivalent to sheared magnetic fields or flux ropes that store free energy. In this state, loss-of-equilibrium or loss-of-stability can occur owing to some disturbances. The system moves to an unstable equilibrium state (c) by storing more free energy. Finally, the system reaches the non-equilibrium state (d), and the system cannot stay in a static state any longer and moves to a dynamic state. In this case, sheared magnetic arcades reconnect owing to emerging flux or horizontal motion in the photosphere, and flux ropes suddenly rise upward if the system reaches the loss-of-equilibrium state; then, flares and CMEs occur. Flux ropes can be erupted by MHD instability even if they do not reach the non-equilibrium state. When flux ropes are strongly twisted by such horizontal motion in the photosphere, field aligned electric current is formed and it caused helical kink instability. This is called the kink mode destabilization model (Fan & Gibson [2003]; Török & Kliem [2005]).
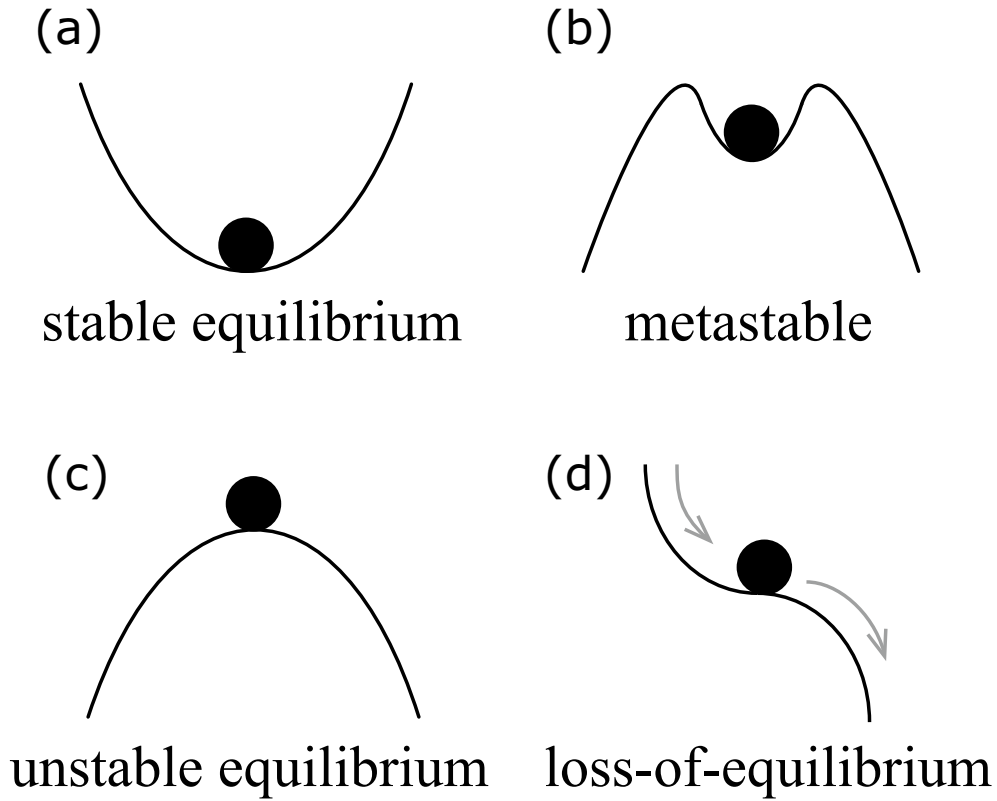
Figure 1.3: Illustration of equilibrium states. The longitudinal direction indicates the free energy stored in the system.

1.3 Force-free Magnetic Fields

As described in the previous section, solar eruptions are generated by the changing of the state of the system from metastable to dynamic. In the corona, the pressure of plasma $P = nk_BT$ is much smaller than magnetic pressure $P_m = B^2/8\pi$, where the typical coronal temperature $T \sim 10^6 \ K$ and the density of coronal plasma $n \sim 10^8 - 10^9 \ cm^{-3}$. Thus, the contribution of P into the force balance can be ignored, and we can only consider the Lorentz force, and the coronal loop structures represent magnetic field lines under the condition. In the corona, magnetic field $\boldsymbol{B} = \boldsymbol{B}_c + \boldsymbol{B}_p$ consists of the magnetic field $\boldsymbol{B}_c$ generated by electric current in the corona and $\boldsymbol{B}_p$ generated by electric current

inside the Sun. In the corona, $\boldsymbol{B}_p$ does not have electric current ($\nabla \times \boldsymbol{B}_p = 0$), and it can be described as $\boldsymbol{B}_p = \nabla\Phi$, where Φ is the potential. The equation can be transformed as a Laplace's equation $\nabla^2\Phi = 0$ by the Maxwell equation $\nabla \cdot \boldsymbol{B}_p = 0$. The potential magnetic field $\boldsymbol{B}_p$, which is the minimum energy state, can be uniquely determined by solving the above Laplace's equation using the distributions of photospheric magnetic field strength as a boundary condition. The large-scale coronal magnetic field can be approximated by the potential magnetic field. However, small-scale or complicated magnetic field structures such as those in an AR are not so consistent with the potential field. Therefore, free-energy released in flares and CMEs are provided by the non-potential magnetic field $\boldsymbol{B}_c = \boldsymbol{B} - \boldsymbol{B}_p$.

The force-free field assumption $(\nabla \times \boldsymbol{B}) \times \boldsymbol{B} = 0$, in which the Lorentz force does not work in the corona, is available as a model of the steady corona. This equation means $\nabla \times \boldsymbol{B} = \alpha\boldsymbol{B}$: the electric current in the corona $\boldsymbol{J} = (c/4\pi)\nabla \times \boldsymbol{B}$ is parallel to the magnetic field $\boldsymbol{B}$, where α is constant along each magnetic field line. When α is constant all over the magnetic structure, it is called a "linear force-free field", otherwise it is called a "non-linear force-free field". This force-free assumption is commonly applied when we consider the coronal magnetic field before flares.

1.4   Various Flare Models

Here, we review several theoretical models of flares which are related to physical processes that cause loss-of-equilibrium and loss-of-stability: tether-cutting model (Moore et al. [2001]), break-out model (Antiochos et al. [1999]), and emerging flux model (Heyvaerts et al. [1977]; Chen & Shibata [2000]). These models are under the Aly-Sturrock conjecture (Aly [1991]; Sturrock [1991]) that the magnetic energy of a force-free magnetic field boundary is at a maximum when the

field is completely open.
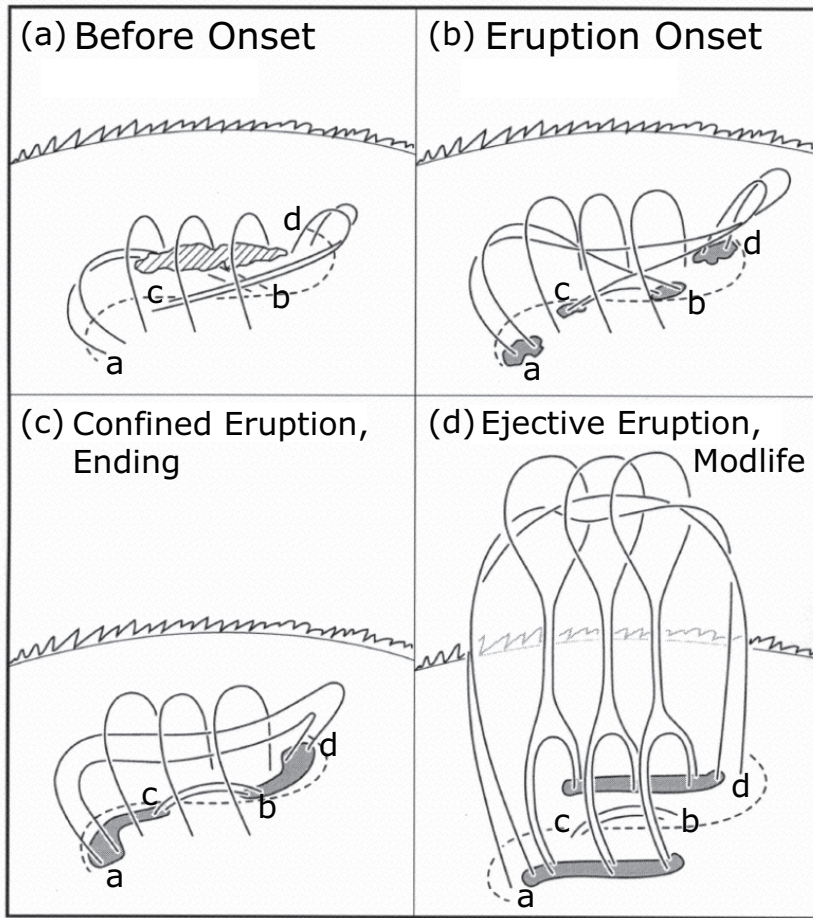
Figure 1.4: The tether-cutting magnetic reconnection (reprinted from Moore et al. [2001])

Figure 1.4 illustrates "tether-cutting magnetic reconnection" proposed by Moore et al. [2001]. The PILs of the photospheric magnetic field and the coronal magnetic arcades are outlined with the broken lines and the solid lines. The magnetic arcades are strongly sheared along the PIL, and a filament (Kippenhahn & Schlüter [1957]), which is filled by diagonal lines, is trapped by the magnetic arcades before the flare onset in panel (a). When tether-cutting magnetic reconnection occurs, the four foot points of the magnetic arcades are brightened, in such as Hα or Ca II H lines, as shown in gray in panel (b). The magnetic arcades a-b and c-d reconnect to a-d and c-b arcades, respectively, and the brightenings

at the foot points grow to the sheared flare ribbons, as shown in panel (c). The magnetic loops connecting a-d grow to long twisted flux ropes as tether-cutting reconnection propagates to outer magnetic arcades. Then, the flux ropes erupt with filaments by loss-of-equilibrium or loss-of-stability, and elongated flare ribbons appear, as shown in gray in panel (d). This model is called the tether-cutting model.
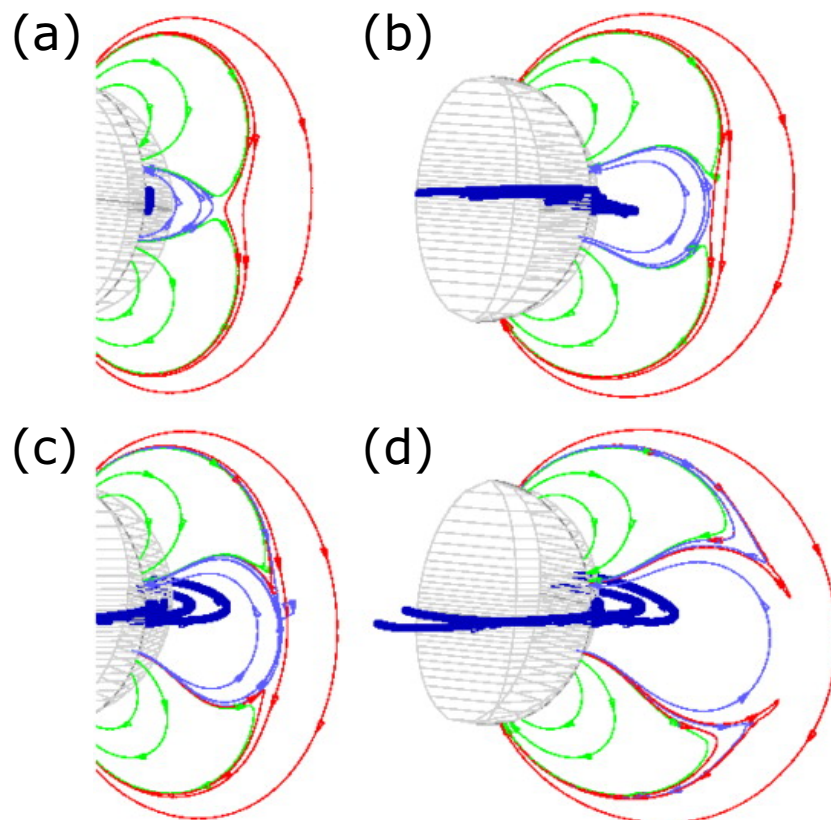
Figure 1.5: The break-out model (reprinted from Antiochos et al. [1999])

In the break-out model (Antiochos et al. [1999]), a multipole structure was considered, as illustrated in Figure 1.5. Blue-, red-, and green-colored thin lines indicate magnetic field lines, and the blue thick lines represent strongly sheared flux ropes. At first, flux ropes are trapped by the blue magnetic arcades, as seen in panel (a). Magnetic pressure at the foot points of the flux ropes increase with

its shearing motion, and overlying magnetic arcades (thin blue lines) are pushed up (see panel (b)). Then, magnetic reconnection occurs between the overlying red arcades and the rising blue arcades because they have an antiparallel component to each other, and the reconnected field lines (green lines) pile up on both sides of the original blue arcades (see panel (c)). The overlying blue magnetic arcades are reduced as reconnection progresses, and the flux ropes are ejected by loss-of-equilibrium or loss-of-stability, as illustrated in panel (d). The electric current sheet vertical to the photosphere is formed by flux rope ejection, and flare occurs.
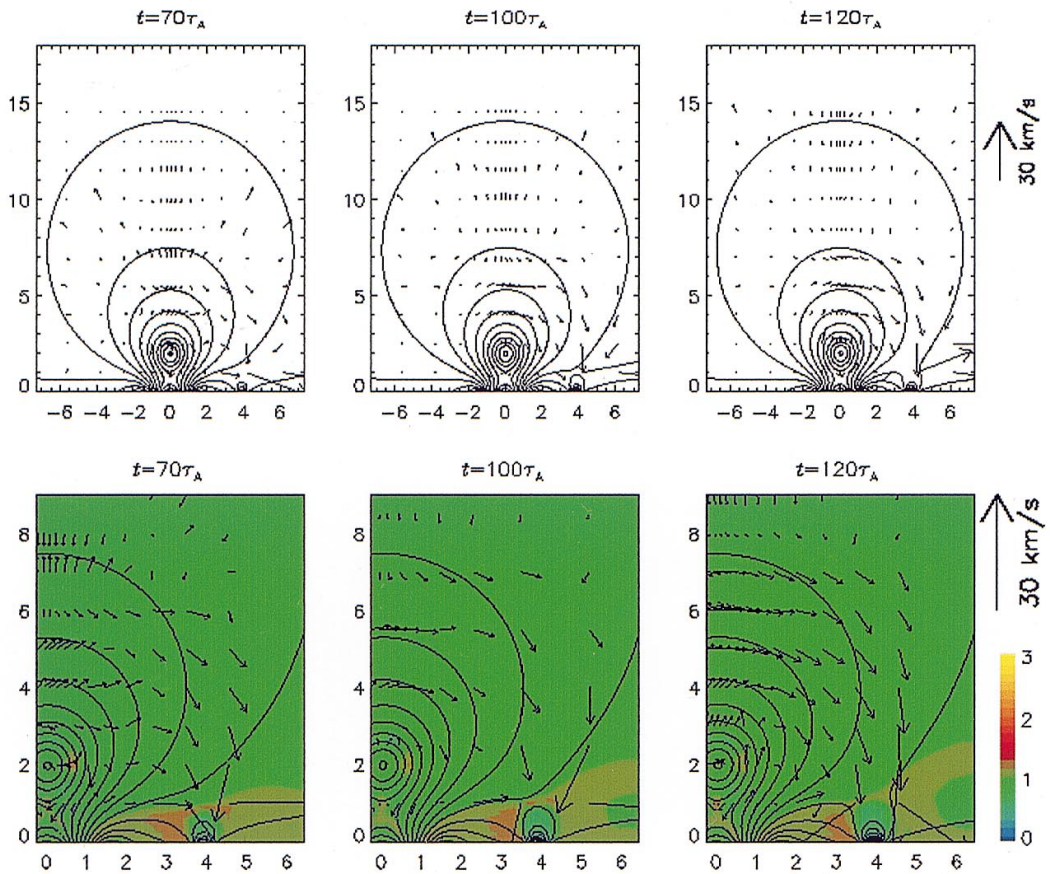
Figure 1.6: Numerical simulation of the emerging flux model (reprinted from Chen & Shibata [2000])

Loss-of-equilibrium or loss-of-stability can be caused by an emerging magnetic flux, which appears near a flux rope, in the emerging flux model. Figure 1.6 shows results of numerical simulation performed by Chen & Shibata [2000]. The global magnetic field lines (black solid lines) and velocity (black arrows) are shown in the upper three panels, and the temperature is colorized in the bottom three panels, which are magnified the region around an emerging magnetic flux. In this model, the magnetic arcades overlying a flux rope are reduced by magnetic reconnection with an emerging magnetic flux, and the flux rope finally erupts.

Thus, various flare models have been proposed thus far, and these models can explain a part of the physical processes of solar explosive/eruptive phenomena, such as flares, CMEs, and filament eruptions. However, it is still unclear what "triggers" magnetic reconnection, loss-of-equilibrium, or loss-of-stability. Moreover, observational verification of these models is insufficient, and the model that can uniformly explain solar flares and CMEs is still not established.

1.5   A Flare Trigger Model: KB12 Model

Here, we describe a flare trigger model, which is recently proposed by Kusano & Bamba et al. [2012]. This section is reconstructed from the previous paper. The model, referred to as the "KB12 model" for short in this thesis, focuses on the trigger mechanism of solar flares based on numerical simulations. In the previous research, it was considered that the interaction of a large-scale magnetic field and a small-scale bipole magnetic field in AR can trigger solar flares. Three-dimensional MHD simulations were performed and, the quantitative conditions of solar flares were investigated.

Figure 1.7 illustrates the simulation setup in Kusano & Bamba et al. [2012]. It assumes a very simple magnetic field structure of an AR, and the white/black

region represents positive/negative magnetic polarity. In the simulation, the pre-existing large-scale magnetic field, which is represented by the red arrows, is given by the linear force-free field:

$$\mathbf{B}_{init}(\alpha; y, z) = B_0 \begin{pmatrix} \alpha k^{-1} \cos ky \\ -K k^{-1} \cos ky \\ \sin ky \end{pmatrix} \exp\left(-Kz\right)$$

where $k = 2\pi/L$, $K = (k^2 - \alpha^2)^{1/2}$, and B_0 is a constant value. The magnetic field is characterized by the parameter α and the shear angle $\theta_0 = \tan^{-1} \alpha/K$, which is defined as the azimuthal rotation of the magnetic field with respect to the potential magnetic field $\mathbf{B}_{init}(0; 0, 0) = (0, -B_0, 0)$. A small-scale bipole field $\mathbf{B}_e$ (indicated by the blue arrow) is injected onto the PIL, and it is characterized by the azimuthal orientation φ_e.
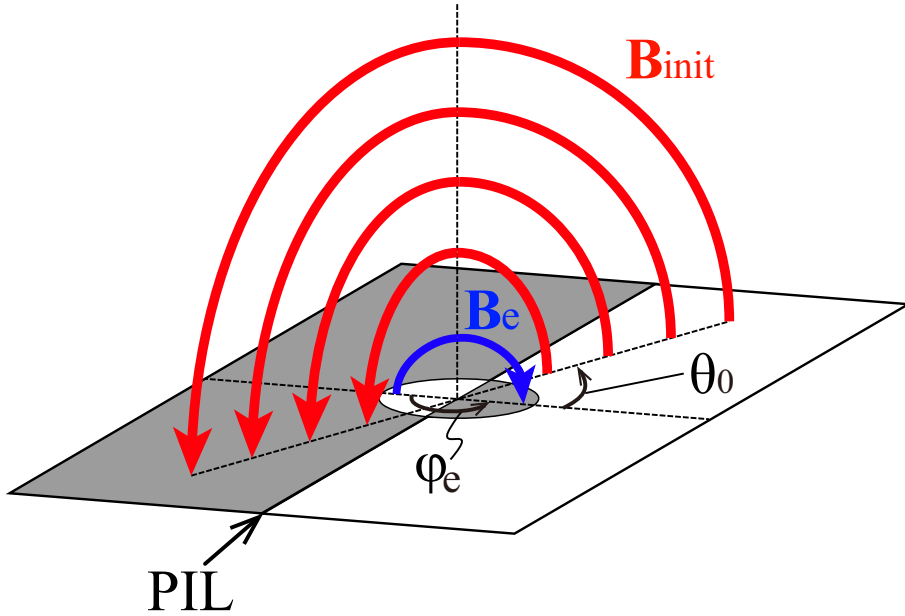
Figure 1.7: Illustration of the simulation setup in Kusano & Bamba et al. [2012]. The white/black region represents positive/negative polarity of the z component of magnetic field. Red and blue arrows indicate magnetic field lines of the pre-existing large-scale magnetic field $\mathbf{B}_{init}$ and that of the small-scale injected bipole field $\mathbf{B}_e$.

The conditions of eruption occurrence were surveyed using the parameters θ_0 and φ_e, which are the shear angle of large-scale force-free field and the azimuthal orientation of the small-scale injected bipole field. The simulation result with the parameters $(0, 0) \leq (\theta_0, \varphi_e) \leq (85°, 360°)$ is summarized in Figure 1.8. The cases $\varphi_e = 0°$, $0° < \varphi_e < 180°$, $\varphi_e = 180°$, $180° < \varphi_e < 360°$ correspond to the small-scale injected bipole field of the right polarity, normal shear, opposite polarity, and reversed shear, respectively, compared with the pre-existing large-scale field. The eruptions occurred only in the condition represented with the colored diamond symbol, while the open square symbol represents the case where eruptions do not occur under the conditions. Moreover, the color contours show the maximum total kinetic energy E_k produced by eruptions, and it is clearly seen that a large-scale eruption is possible only in the condition of $\theta_0 > 75°$. In contrast, the occurrences of solar eruptions are decided by the azimuthal orientation φ_e of the small-scale injected bipole field. Therefore, these results indicate that a strongly sheared field stores a greater amount of free energy as a non-potential field but the onset condition of solar eruptions is governed by small magnetic structures. Moreover, it was found that the two typical magnetic structures could trigger solar eruptions: the Opposite Polarity (OP) and Reversed Shear (RS) types.
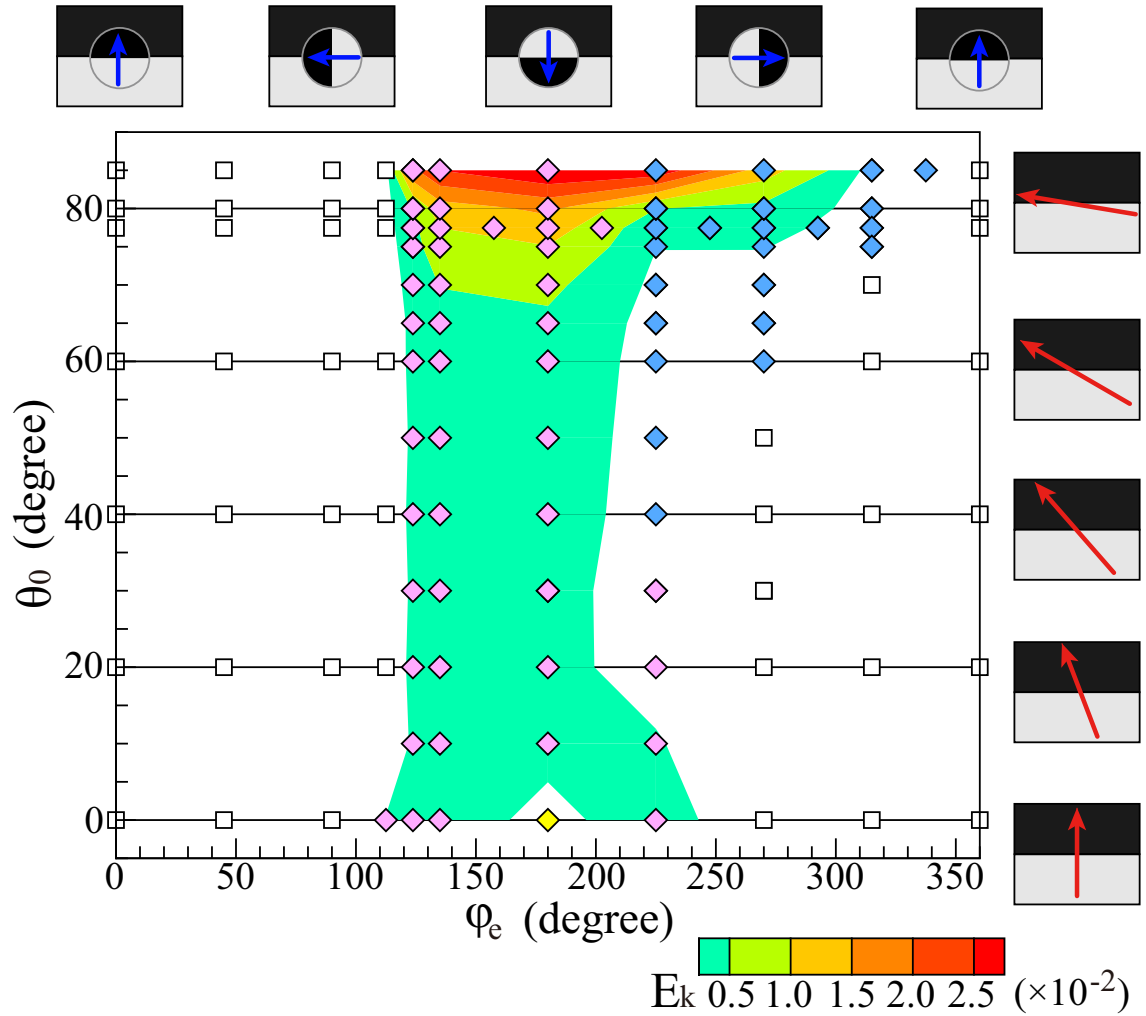
Figure 1.8: Flare Phase Diagram (reprinted from Kusano & Bamba et al. [2012]) summarizing the simulation results. The diamond mark indicates that the eruption has occurred under the θ_0 and φ_e conditions. Pink/blue indicates the types of dynamics: "eruption-induced reconnection (OP-type)" and "reconnection-induced eruption (RS-type)". The yellow diamond corresponds to a special case where the potential field collapses because of reconnection with the small-scale injected field, which exhibits a completely antiparallel polarity compared with the initial potential field. The open square symbol means eruptions do not occur under the conditions, and the color contours show the maximum total kinetic energy E_k released by eruption.

(a) Opposite Polarity type   (b) Reversed Shear type
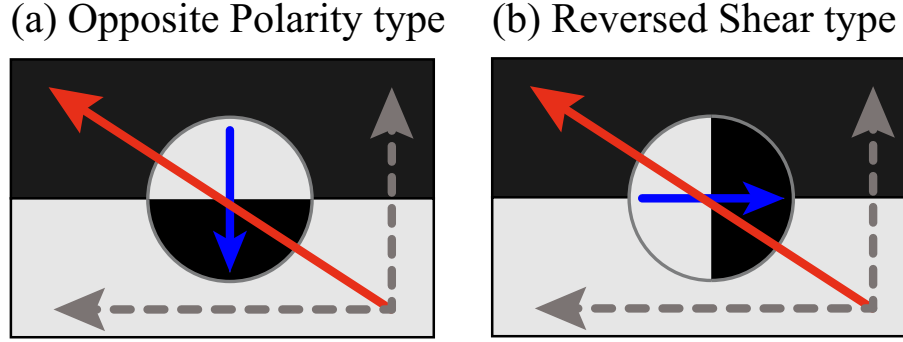
Figure 1.9: Geometrical concepts of the Opposite Polarity type and the Reversed Shear type in the KB12 model. The white/black region corresponds to positive/negative polarity of the line-of-sight (LOS) magnetic field, and these are the top views of Figure 1.7. Red arrows indicate the pre-existing large-scale magnetic field $\mathbf{B}_{init}$, and blue arrows represent the small-scale injected bipole field $\mathbf{B}_e$. Gray broken arrows represent the potential component (horizontal arrows) and the shear component (vertical arrows) of $\mathbf{B}_{init}$.

Figure 1.9 illustrates the geometrical concepts of the OP- and RS-types. In case of the OP-type, a small-scale injected magnetic field is opposite to the potential component of the large-scale field. Conversely, in the RS-type case, a small-scale injected magnetic field is reversed to the shear component of the large-scale field. Moreover, these two-types have different physical processes leading to flux rope eruption: "eruption-induced reconnection" and "reconnection-induced eruption" processes.

Figures 1.10 and 1.11 show the snapshots of the numerical simulation in Kusano & Bamba et al. [2012] for the OP- and RS-types, respectively. Figure 1.10 shows the case of the OP-type magnetic field structure; $(\theta_0, \varphi_e) = (180°, 77.5°)$, and the eruption process is as described below in this case:

1. First, two sheared magnetic field lines (blue tubes in panel (a)) exist, and the small-scale bipole field of the OP-type is injected at the foot point. Then the pre-existing sheared fields reconnect via the OP-type small-scale bipole, and twisted flux ropes (green tubes in panels (b - d)) are formed. The initial flare ribbons F/F' appear at the foot points of twisted flux ropes.

2. Twisted flux ropes are piled up as reconnection goes on (panel (e)), and these are suddenly start to erupt upward (panel (f)). Overlying field lines (such as the blue tubes in panel (d)) are stretched vertically as flux ropes erupt, and new vertical current sheets (red surface in panel (f)) are generated below them.

3. Magnetic reconnection starts on the vertical current sheets, and a cusp-shaped post-flare arcade along with more twisted ropes is formed, and it accelerates the eruption (see panels (g, h)). The extended flare ribbons R1 and R2 (R1' and R2') appear at the foot points of the post-flare arcades.
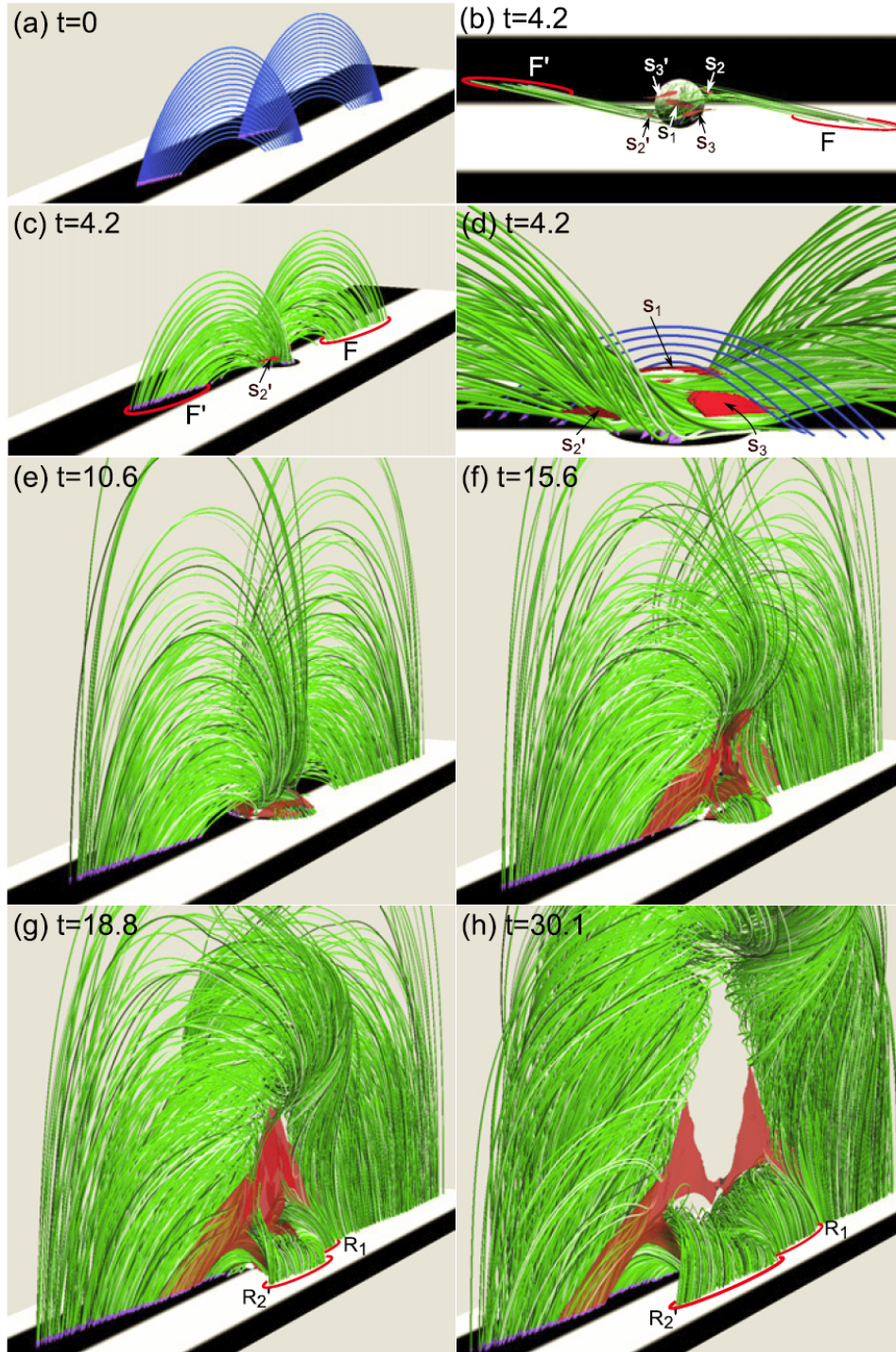
Figure 1.10: Images of the Opposite Polarity type numerical simulation with the condition of $(\theta_0, \varphi_e) = (180°, 77.5°)$ (reprinted from Kusano & Bamba et al. [2012]). (a, c, e - h) are the bird's eye views and (b, d) are the top views. The white/black part corresponds to positive/negative polarity of the LOS magnetic field. Blue tubes indicate the magnetic field lines of the pre-existing large-scale field, and green tubes represent those of the reconnected magnetic field. Red contours correspond to strong electric currents produced by magnetic reconnection.

On the other hand, the eruption process in the RS-type case of $(\theta_0, \varphi_e) = (180°, 77.5°)$ is as follows:

1. A small-scale injected bipole field interacts with the pre-existing sheared field (blue tubes in Figure 1.11 (a)), and an electric current sheet is formed between them (panels (a - c)). The reconnected fields pile up on both sides of the injected bipole as green tubes in panels (b, c), and the sheared field is reduced from the upper region of the injected RS-type field.

2. Then, the pre-existing fields (such as sky-blue tubes in panel (d)) collapse to the central region, where the magnetic pressure decreased because of the reduction of the sheared field, and the vertical electric current sheet is generated. The sheared magnetic fields are reconnected and twisted flux ropes are formed. The flare ribbons F and F' appear at the foot points of the twisted flux ropes.

3. These twisted flux ropes gradually rise upwards, and it vertically stretches the overlying fields, and new vertical electric current sheets are generated below them (panels (e, f)). Magnetic reconnection occur on this current sheets and flare ribbons are enhanced to connect R - F (R' - F') at the foot points of the twisted flux ropes (panels (g, h)).
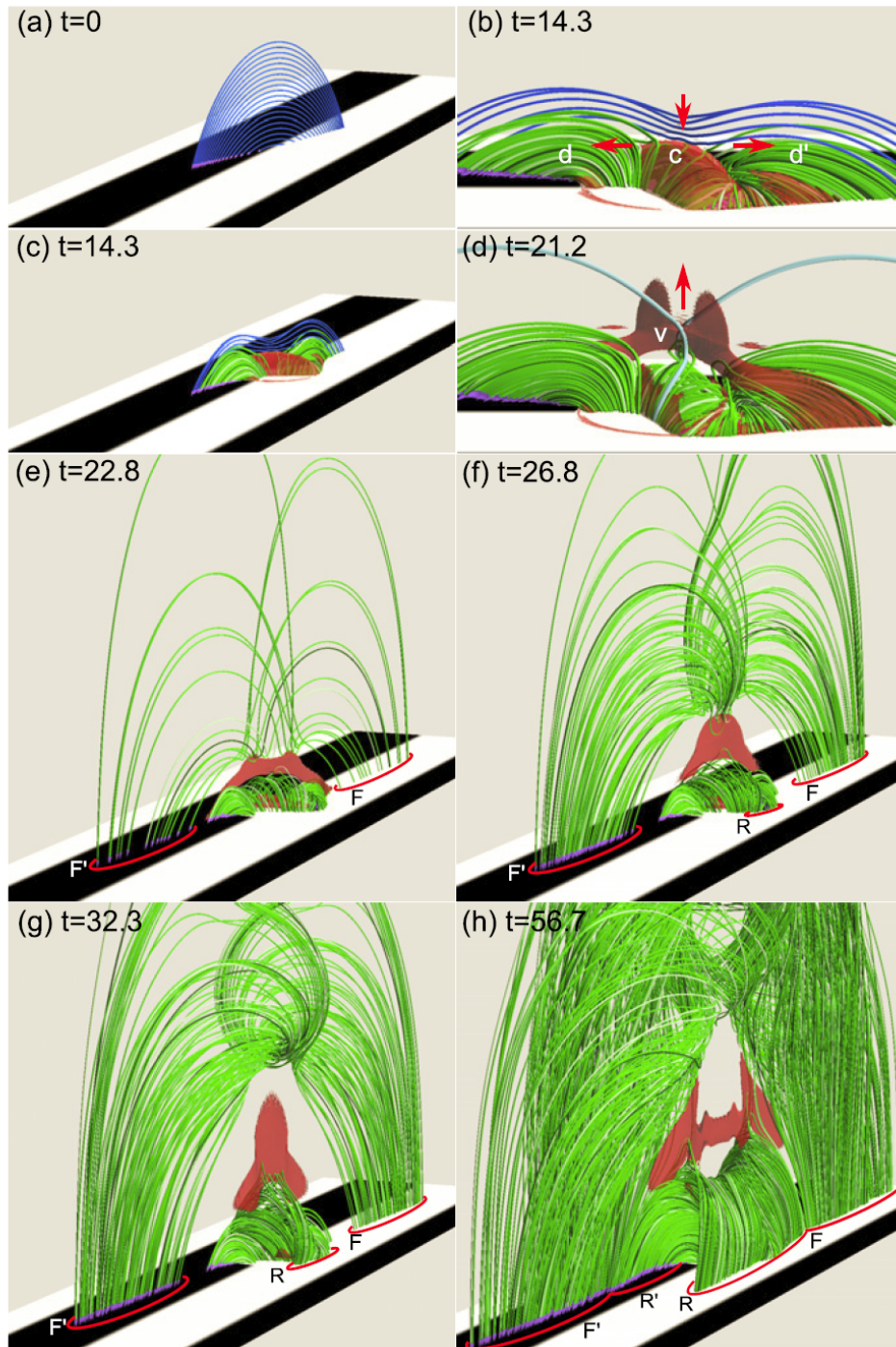
Figure 1.11: Images of the Reversed Shear type numerical simulation with the condition of $(\theta_0, \varphi_e) = (270°, 77.5°)$ (reprinted from Kusano & Bamba et al. [2012]). Both blue and sky-blue tubes indicate the magnetic field lines of the pre-existing large-scale field in panels (a - d). Other symbols are formatted the same as for Figure 1.10.

Therefore, the eruption leads flare reconnection in the OP-type process, whereas flare occurs prior to flux rope eruption in the RS-type process. We should note that the morphology of the magnetic field in the latter phase (after the onset of flare reconnection) of both processes is consistent with the CSHKP model, and it is consistent also with tether-cutting model. Moreover, the picture of the KB12 model, that the reconnection between the injected small-scale bipole field (the blue arcade $\mathbf{B}_e$ in Figure 1.7) and the pre-existing large-scale sheared field (the red arcade $\mathbf{B}_{init}$ in Figure 1.7) can trigger solar flare, is basically the same to that of emerging flux model. The subsequent reconnection of the pre-existing large-scale field is also the common physical process to the tether-cutting model (cf. Section 1.4). However, the small-scale bipole field $\mathbf{B}_e$ is not necessarily an emerging flux in the KB12 model, and it may be formed by horizontal motion on the solar surface. The KB12 model has novelty from the viewpoint of that it proposed the specific conditions (i.e. the specific combinations of the parameters θ_0 and φ_e) for flare triggering. Furthermore, the KB12 model can explain the mutual relation between the flare and CME, without regard to order.

Henceforth, we call the magnetic reconnection between the injected small-scale bipole field and the pre-existing large-scale sheared field "internal reconnection", and the reconnection between the large-scale sheared fields "flare reconnection". We also call the small-scale bipole field $\mathbf{B}_e$ the "flare trigger field", and the region, where the flare trigger region appear, the "flare trigger region".

1.6 The Aim of the Thesis

As we described earlier in this chapter, the triggering process of solar flares are still veiled. The motivation of this thesis is to gain understanding of the physical process and to elucidate the conditions related to solar flare triggering. The KB12 model explains the physical process and shows the quantitative conditions

leading to solar flares as summarized in Figure 1.12. Thus, we aim to examine (1) whether the quantitative parameters and these combinations of the KB12 model are suitable as the flare trigger condition, and (2) whether the two-types of physical processes of the model are consistent with observed features. To achieve the objective, we investigate the following features using the satellite observations: the large-scale and small-scale magnetic field structures in the flaring ARs, which are characterized by the parameters θ_0 and φ_e, and the pre-flare brightenings and initial flare ribbon structures.
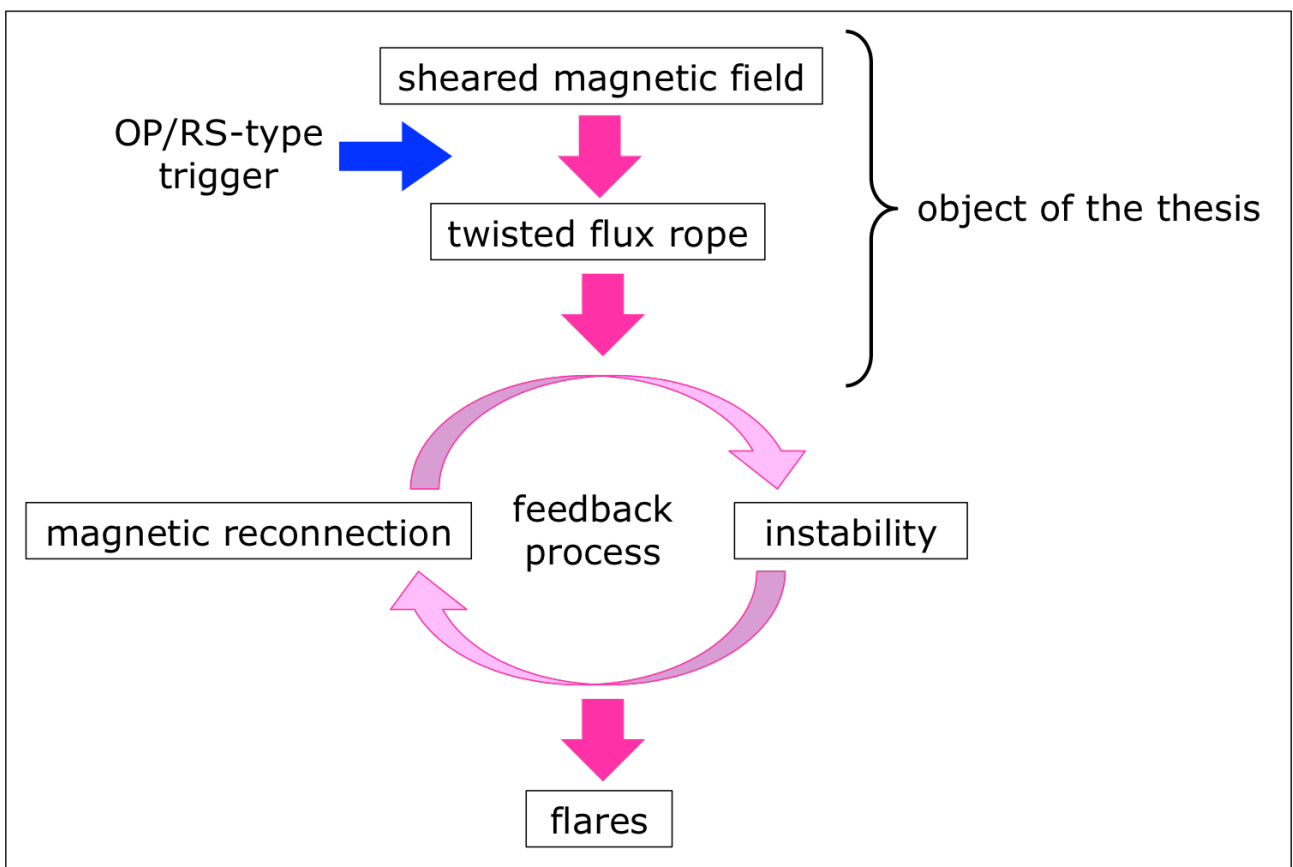
Figure 1.12: Chart illustrating physical process of the KB12 model. This indicates the object of the thesis.

We investigate the spatial and temporal correlation between the photospheric magnetic field structures and the chromospheric brightenings, for several flare events, which clearly shows the sheared two flare ribbons in the bipole region, in chapter 2. Then, we expand the analysis to a complicated AR, whose magnetic field structure is away from the simulation setup of the KB12 model, in Chapter 3. In Chapter 4, we discuss the three issues. We first discuss the plasma dynamics in the flare trigger region, with the aim to confirm that the chromospheric brightenings are caused by the internal reconnection between the pre-existing sheared magnetic field and small-scale flare trigger field. Second, we propose a possibility of an additional parameter that should be considered as flare trigger conditions. Third, we discuss the consistency between the various flare events and the flare trigger process of the KB12 model, by statistically investigate the events which did not satisfy the important observable features predicted by the model. In Chapter 5, we finally summarize the conclusions of the thesis and mention future direction of the study using the KB12 model.

Chapter 2

Identification of Flare Trigger Region

2.1 Introduction

As we introduced in Section 1.5, the KB12 model proposed that two-types of small-scale magnetic fields can trigger solar flares. In this chapter, we aim to find out the "flare trigger region": the small-scale bipole of the OP- and RS-types (i.e. the "flare trigger field") appears. Here, we summarize the procedure to identify the flare trigger region.

1. To investigate whether there is the characteristic magnetic field structure at the center of the sheared two flare ribbons in the initial flare phase. It is because the small-scale bipole magnetic field was injected just above the global PIL of the AR, and the initial flare ribbons appear at the foot points of the overlying sheared magnetic field, in the numerical simulation of the KB12 model.

2. To check the pre-flare brightenings over the characteristic magnetic field structure before the flare onset. Because it is inferred that the chromospheric brightenings are caused by the internal magnetic reconnection between the pre-existing sheared magnetic field and the flare trigger field in the flare trigger region.

3. To measure the global magnetic shear angle θ_0 and the azimuthal angle φ_e in the flare trigger region, and to confirm whether the combination of the angles θ_0 and φ_e is consistent with either the OP- or RS-types of the KB12 model.

In order to confirm the existence of the flare trigger region through the above procedure, we analyzed several major flare events, which were observed by the Hinode satellite (Kosugi et al. [2007]), and compared the observed features and the results of the numerical simulations of the KB12 model.

2.2 Overview of Hinode/SOT and Data Description

First of all, we introduce Hinode, which is mainly used for the analysis in this chapter. Hinode (Figure 2.1) is a Japanese satellite and the Solar Optical Telescope (SOT: Tsuneta et al. [2008]; Suematsu et al. [2008]; Ichimoto et al. [2008]; Shimizu et al. [2008]), which is 50 cm aperture Gregorian reflecting telescope, is the main observation apparatus. Hinode orbits a sun-synchronous polar orbit with the altitude of ~ 680 km, and it can continuously observe the Sun nine months a year. SOT has attained the diffraction limit and it has the highest accuracy for the photospheric magnetic field measurements, and the spatial resolution is $0.2''$ - $0.3''$ for the range of 3880 - 6302 Å. SOT performs two observations: imaging observations by the filtergraph (FG) and spectro-polarimetric observations by the Spectro-Polarimeter (SP; Lites et al. [2013]). FG has two channels called the Broadband Filter Imager (BFI) and the Narrowband Filter Imager (NFI), and the field of view (FOV) is $217'' \times 108''$ and $327'' \times 163''$, respectively. NFI can take filtergrams, dopplergrams, and polarimetric images of some photospheric and chromisoheric lines such as Fe I (6303 Å) or Na I D1 (5896 Å) lines, while BFI takes filtergrams of chromospheric lines (e.g. Ca II H line (3968 Å)) or continuum lines. SP observes the full-polarization states (Stokes-I,

Q, U, and V) of two magnetically sensitive Fe lines at 6301.5 and 6302.5 Å, and we can derive three components of the photospheric magnetic field (B_x, B_y, B_z).
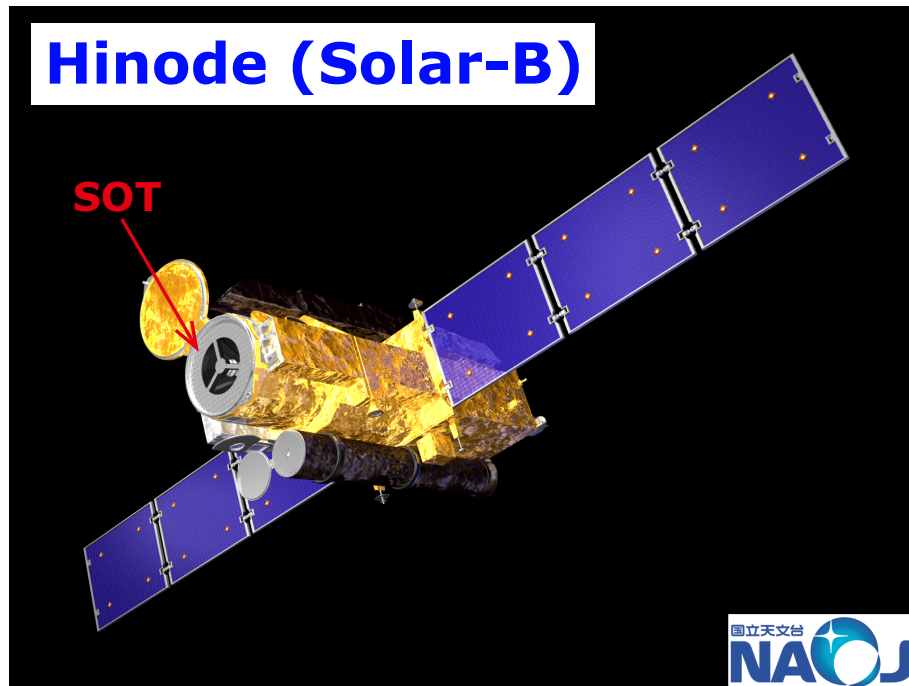
Figure 2.1: The Hinode satellite (copyright by NAOJ, ISAS/JAXA).

Flare events were selected from the Hinode Flare Catalogue[1] (Watanabe et al. [2012]) based on the following criteria.

1. GOES class is larger than M5.0.

2. The event was observed by Hinode/SOT from 2006 October 1 to 2011 July 31.

3. Both the pre-flare and main flare phases were well covered by Hinode/SOT observation.

4. The flaring site was located within $\pm$ 750″ from the solar disk center.

---

[1] http://st4a.stelab.nagoya-u.ac.jp/hinode_flare/

Because it was inferred that the flare trigger region for the large event, which releases higher energy, is spatially large and easy to find, we chose the major flare events. Moreover, we limited the location width of the flaring AR to $\pm\,750''$ from the solar disk center, in order to use accurate LOS magnetic field data. These criteria were satisfied by the four events occurring in ARs NOAA 10930 and 11158, and these events were analyzed in this chapter. The information of the date, start time, class, and locations for each event is listed in Table 2.1.

No.	Date	Start Time (UT) [a]	Class [a]	NOAA AR	Location [b]
1	2006 December 13	02:14	X3.4	10930	S07W22
2	2006 December 14	22:07	X1.5	10930	S06W46
3	2011 February 13	17:28	M6.6	11158	S20E05
4	2011 February 15	01:44	X2.2	11158	S20W10

Table 2.1: List of flare events

AR 10930 appeared on the east limb on 2006 December 5 and produced a number of flares during disk passage. Among the four X-class flares occurring in the AR, two of those were observed by Hinode/SOT, namely X3.4 at 02:14 UT 2006 December 13 (e.g. Kubo et al. [2007]) and X1.5 at 22:07 UT 2006 December 14 (e.g. Watanabe et al. [2010]). At the time of these events, designated as Events 1 and 2, respectively, the AR was around 0° - S10° latitude and W20° - W45° longitude.

AR 11158 appeared on the moderate southeast limb and produced one X-class flare and five M-class flares during the disk passage from 2011 February 11 to 19. We have analyzed the M6.6 flare (Event 3; e.g. Liu et al. [2012], Toriumi et al. [2013]) and the X2.2 flare (Event 4; e.g. Wang et al. [2012]), which were observed by the SOT at 17:28 UT 2011 February 13 and at 01:44 UT 2011 February 15, respectively. Between these two major events, numerous C-class flares occurred

---

[a]The start time and class are defined from X-ray observations of the GOES satellite.
[b]http://www.solarmonitor.org/

in the AR. During flaring, the AR was located around S15° - S25° latitude and E10° - W10° longitude.

We used filtergams obtained by the BFI in Ca Ⅱ H line (3968 Å) and Stokes-V/I images obtained by the NFI in Fe I line (6303 Å) or Na I D1 line (5896 Å). The circular polarization signal was measured by NFI at the only one wavelength point shifted from the Fe I line by -120 mÅ/from the Na I D1 line by 140 mÅ, respectively. Ca Ⅱ H line images sensitively sample the chromospheric atmosphere, whereas Fe I and Na D1 lines are sensitive to the LOS magnetic field in the photosphere and the base of chromosphere, respectively. The analyzed Ca-line images and Stokes-V/I images were almost continuously collected for approximately 24 hours prior to the flare onset. The cadence of filtergrams was two minutes for AR 10930 and approximately five minutes for AR 11158. The spatial resolution was $0.3''$ for Stokes-V/I images and $0.2''$ for Ca-line images in both case.

We also used vector magnetograms derived by SP scan data. The SP scan data were calibrated by the `sp_prep` procedure (Lites & Ichimoto [2013]) in the Solar Soft-Ware (SSW) package, then the Milne-Eddington inversion assuming a parallel-plane atmosphere to the calibrated data. The inversion code MEKSY (developed by Dr. Takaaki Yokoyama) was adopted, and 180° ambiguity in the vector magnetograms is resolved using the AZAM utility (Lites et al. [1995]). In this study, the Stokes-V/I signal of filterams is converted to the photospheric LOS magnetic field using SP scan data listed in Table 2.2. The vector magnetogram was used also to evaluate the averaged shear angle θ_0.

AR	Date	Scan Time (UT)	FOV	Propose of Use
10930	2006 Dec 12	20:30:05 - 21:33:17	$195'' \times 162''$	Measurement of the shear angle
10930	2006 Dec 13	04:30:05 - 05:36:08	$195'' \times 162''$	Conversion of Stokes-V/I signals
10930	2006 Dec 14	17:00:05 - 18:03:17	$195'' \times 162''$	Measurement of the shear angle
11158	2011 Feb 13	16:00:04 - 16:32:25	$151'' \times 162''$	Measurement of the shear angle Conversion of Stokes-V/I signals
11158	2011 Feb 14	06:30:04 - 07:02:25	$151'' \times 162''$	Measurement of the shear angle

Table 2.2: SOT/SP data used in the analysis

2.3 Analysis Method

2.3.1 Superposition of Ca II H Line and Stokes-V/I Images and Detection of Flare Trigger Regions

It has been proposed by the KB12 model that the internal reconnection between a small-scale bipole field and overlying sheared magnetic arcade is a precursor of flare reconnection. If the magnetic structure in the flare trigger region satisfies the OP-type, the internal reconnection conjoins two sheared loops into an unstable twisted flux rope. In contrast, if it satisfies the RS-type magnetic field structure, the internal reconnection partially cancels the sheared field and causes inward collapse of the magnetic arcade as well as initiating flare reconnection. In both cases, the internal reconnection probably manifests as the pre-flare brightening in chromospheric lines.

Therefore, spatial and temporal correlation analysis between the magnetic field and Ca II H brightening is a powerful means of detecting the structure most likely to trigger a flare. To determine the flare trigger region, we carefully superimposed Stokes-V/I images obtained by FG in Fe- or Na-lines (indicating

the configuration of the photospheric LOS magnetic field) and Ca-line images. We first calibrated each image by dark-current subtraction and flat fielding using the `fg_prep` procedure the SSW package. We then removed spatial fluctuations by cross-correlating two consecutive images. Selecting a Ca-line image temporally closest to a Stokes-V/I image, the two images were reconstructed to the same size as shown in Figure 2.2, because the pixel scales of the BFI and the NFI are different (Shimizu et al. [2007]). We repeatedly aligned a Stokes-V/I and a Ca-line images by cross-correlating, at each time (Figure 2.2 (3)), and drew the PILs and Ca-line strong brightening contours onto the Stokes-V/I images, where the PILs are defined as the lines of zero Stokes-V/I value.

The numerical simulation of the KB12 model has predicted that flare trigger regions of either type (OP or RS) are located between the initially brightening two-ribbons, which basically form a sheared configuration. We first examined whether a magnetic structure consistent with the model exists, by analyzing the superimposed Ca-line brightening and Stokes-V/I images. As we discuss in Section 2.4, we successfully identified the required flare trigger regions and the magnetic structures underlying all four events.

(1) original images

Fe I

1024 pixel

2048 pixel

0.16"/pixel

Ca II H

1024 pixel

2048 pixel

0.108"/pixel

(2) resized images

1024 pixel

2048 pixel

701 pixel

1402 pixel

(3) alignment

Fe I
         ...
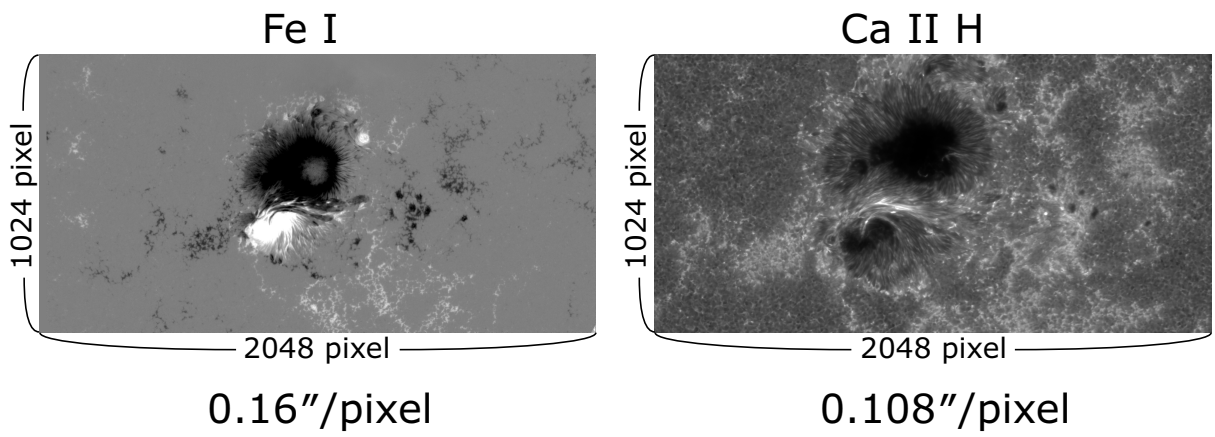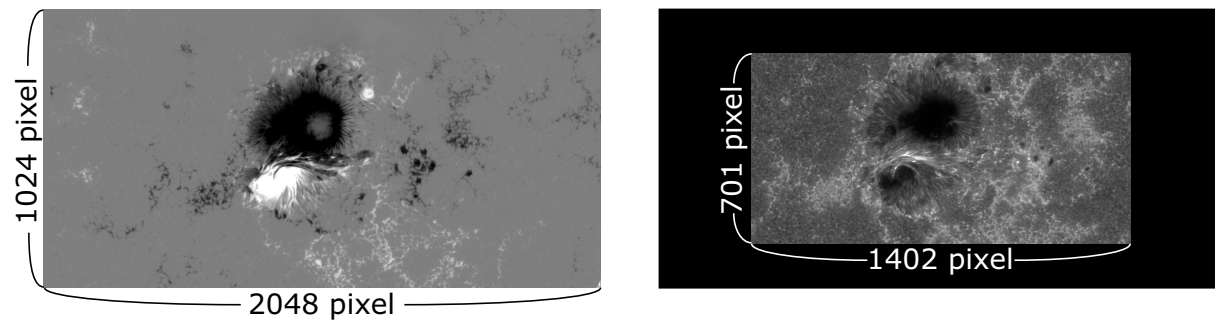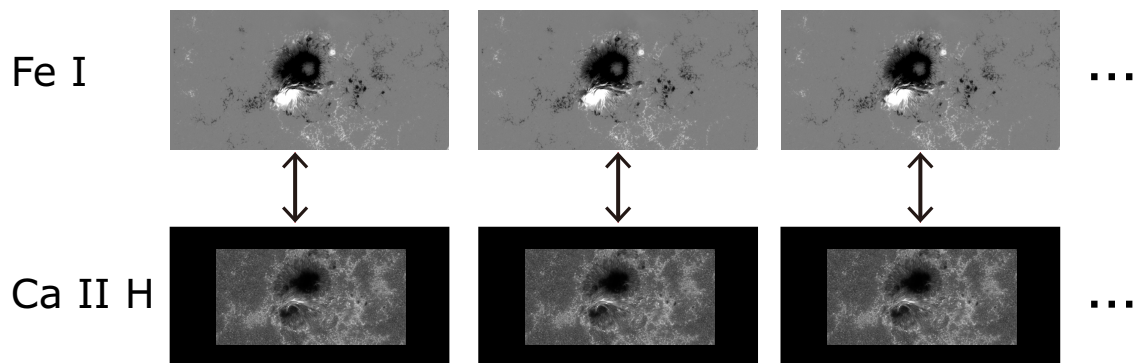
Ca II H
         ...

Figure 2.2: The method of alignment between Stokes-V/I images and Ca II H line images obtained by Hinode/SOT FG.

2.3.2   Measurement of Magnetic Shear and Orientation
of the Flare Trigger Region

Having determined the flare trigger region, we measured the magnetic shear angle θ_0 in the flaring site and the azimuth orientation φ_e of the flare trigger region. As shown in Figure 2.3, θ_0 is defined as the counterclockwise twist angle of the transverse magnetic field observed by SOT/SP from the direction $\boldsymbol{N}$ normal to the averaged PIL, defined as the line where the smoothed LOS component of the magnetic field $< B_{LOS} >= 0$. Low-pass filtering yields the smoothed magnetic field

$$< B_{LOS} >= \sum_{|k_x|<k_{x0},|k_y|<k_{y0}} \tilde{B}_{LOS}(\boldsymbol{k})e^{i\boldsymbol{k}\cdot\boldsymbol{r}},$$

where $\tilde{B}_{LOS}(\boldsymbol{k})$ is the complex Fourier component of mode $\boldsymbol{k}$. The critical scale $2\pi/k_{x0} = 2\pi/k_{y0} = 4.8 \times 10^7 \ cm$ for Events 1, 2, and 4, and $2\pi/k_{x0} = 2\pi/k_{y0} = 2.4 \times 10^7 \ cm$ for Event 3. The shear angle θ_0 is averaged over flaring region, as shown in the following sections.

The azimuth angle of flare trigger region φ_e is also defined as the anti-clockwise angle between $\boldsymbol{N}$ and the local normal vector $\boldsymbol{n}$, which is orthogonal to the (non-averaged) PIL $< B_{LOS} >= 0$. When the PIL is meandering, however, the vector $\boldsymbol{n}$ as well as angle φ_e is sensitive to where $\boldsymbol{n}$ is defined. In our analysis, we determined the center of flare trigger region O using Ca-line brightening data.

According to the KB12 model, solar flares can be caused by internal reconnection and it is likely produces chromospheric brightenings. Therefore, to determine the position where we should define $\boldsymbol{n}$, we sought the region of PIL where the intense brightening of Ca-line was observed just prior to the onset of flare. Then, assuming that the position O exists within the region of PIL with Ca-line brightening, we measured the average and range of $\pm \phi$, and adopted them as

the orientation of a small-scale bipole field and the error range, respectively. The error in φ_e was evaluated as the difference between minimum and maximum of multiple n measurements, whereas the error in θ_0 was the standard deviation.

(a)

(b)
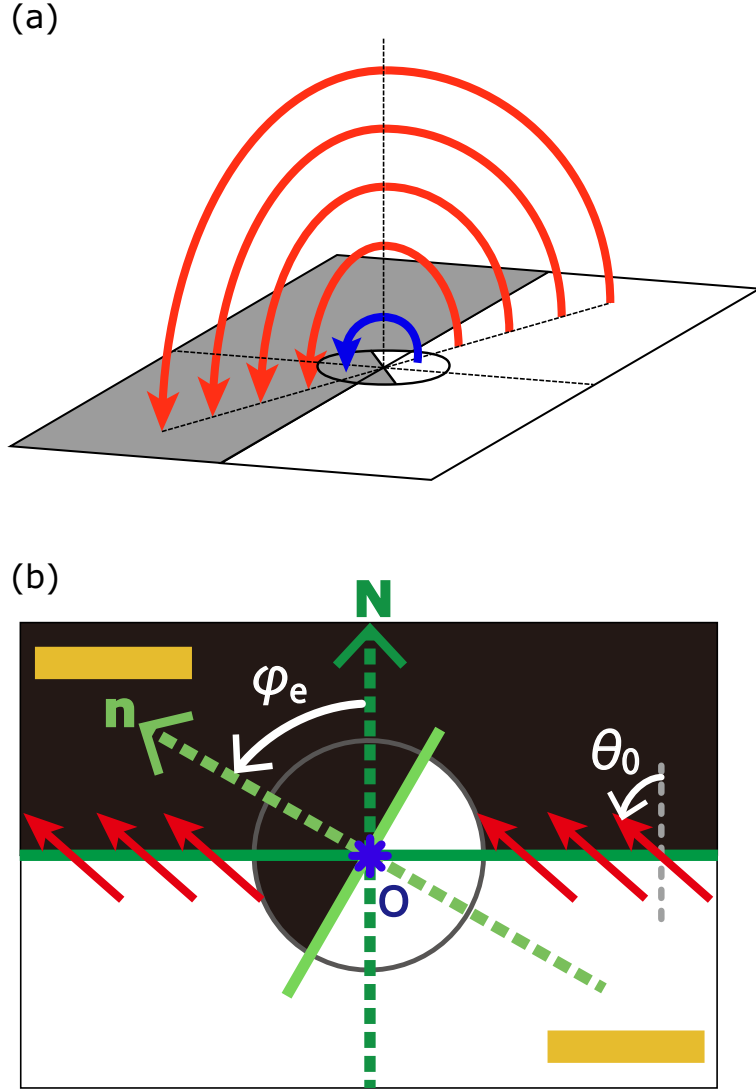
Figure 2.3: Definitions of the azimuth φ_e and the shear angle θ_0. White/black (gray) corresponds to positive/negative polarity of the LOS magnetic field. (a) Bird's eye view of an AR presented in the simulation setup of Kusano & Bamba et al. [2012]. (b) Top view of (a). The yellow lines indicate the sheared flare ribbons and the red arrows are the transverse magnetic field. We defined the center of flare trigger region O (blue asterisk), which should be located on the center of the initial flare ribbon and on the PIL. The vectors $\boldsymbol{N}$ and $\boldsymbol{n}$ are normal to the PIL of the averaged magnetic field and the PIL on the flare trigger region. The azimuth φ_e is measured as the mean angle of the transverse magnetic field over the flare trigger region.

2.4 Results

2.4.1 Event 1: X3.4 Flare in AR 10930 on 2006 December 13

Figure 2.4 shows the temporal variations of Stokes-V/I and Ca-line brightening for the X3.4 flare (Event 1). Green lines indicate the PILs (zero Stokes-V/I value), and red contour is strong Ca-line brightening such as pre-flare brightenings and flare ribbons. The initial flare ribbons had sheared structure as seen in panel (d), and it suggests that the trigger region is located around the yellow circle. There is an elongated bipole field between the major magnetic poles, and it was originally a small positive island in the negative sunspot, as indicated by yellow arrow in panel (a). The small isolated positive pole was slowly grew since 23:00 UT on December 12, and it separated negative pole and formed elongated bipole field structure. Ca-line brightenings were frequently observed over the PIL of the elongated bipole field as seen in panel (b). The initial flare ribbons appeared as seen in panel (c) just after the flare onset (02:18 UT December 13), and simultaneously, an elongated Ca-line brightening was seen between the initial flare ribbons. These features are consistent with the OP-type simulation results of the KB12 model, assuming that these features appears on the intensive electric current sheets formed on the top, bottom, and lateral side of the twisted flux rope, which is created by the internal magnetic reconnection. Then the central, elongated brightening disappeared and flare ribbons enhanced in panel (d). From these observed features, we inferred that the elongated positive pole is the trigger of the X3.4 flare.
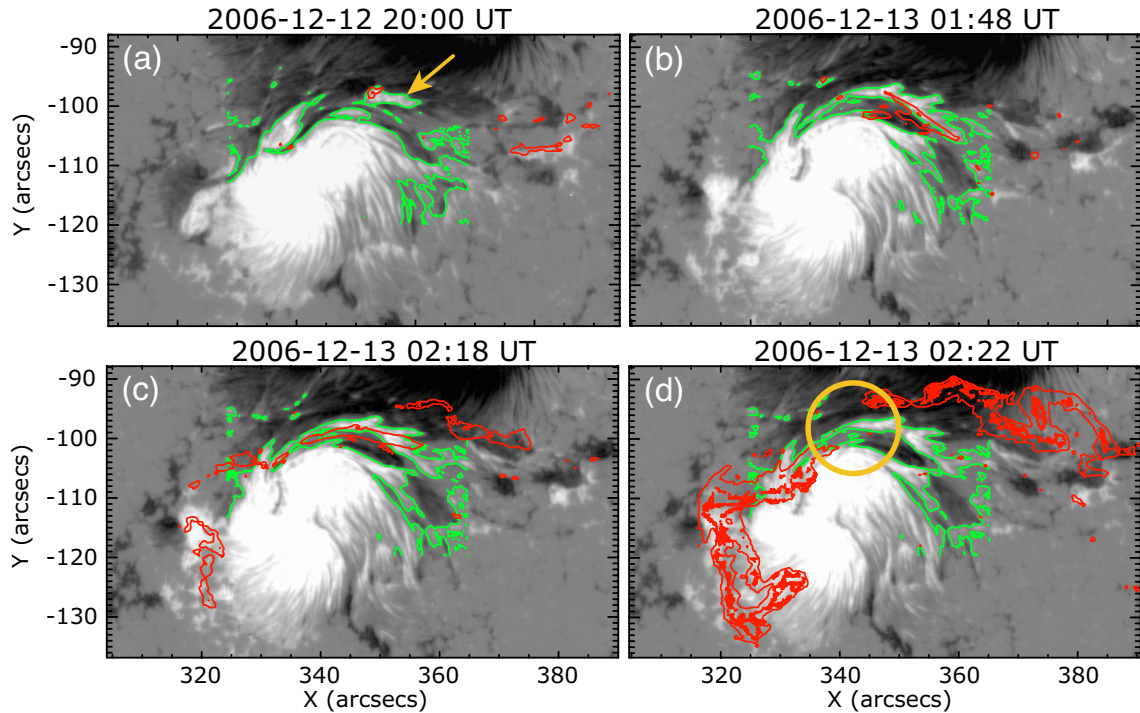
Figure 2.4: Temporal variations of Stokes-V/I preceding the X3.4 flare (Event 1) on December 13, 2006. Grayscale corresponds to positive/negative polarity of the LOS magnetic field, and the intensity scale is ± 0.1. Green lines indicate the PIL (zero Stokes-V/I value), and red contours are Ca-line brightening at 1800 DN. Yellow arrow in panel (a) indicates the small isolated positive pole, which will grow to the flare trigger field.

Next, we defined the trigger point O and vectors $\boldsymbol{N}$ and $\boldsymbol{n}$, as seen in Figure 2.5, in order to measure the azimuth φ_e and the shear angle θ_0. The small-scale bipole field was decomposed from the large-scale magnetic field by low-pass filtering of the LOS magnetic field, which yielded the smoothed magnetic field $< B_{LOS} >$. In panel (b), the grayscale images correspond to the positive/negative polarity of $< B_{LOS} >$, while green lines indicate the PILs of $< B_{LOS} >$ on which Ca-line brightening (red contours) are overlaid. The trigger point O was defined as the point where the smoothed PIL overlaps with last Ca-line brightening contour at 02:14 UT December 13. O should be located at the center of the initial flare ribbons and on the smoothed PIL, and the vector $\boldsymbol{N}$ was normal to the smoothed PIL at point O and directed from positive to negative $< B_{LOS} >$. $\boldsymbol{N}$ denotes the reference orientation of the large-scale magnetic field of the AR.

Figure 2.5 (c) is an enlarged view of the flare trigger region at 02:14 UT. The vector $\boldsymbol{n}$ was defined to be normal to the (unsmoothed) PIL at the last Ca-line brightening contours which were immediately prior to the flare onset, and directed from positive to negative $< B_{LOS} >$. Panel (d) shows the final vector magnetogram obtained by SOT/SP (20:30 UT on December 12) before the flaring event. The region over which the shear angles were averaged to derive θ_0 is enclosed within the yellow square.
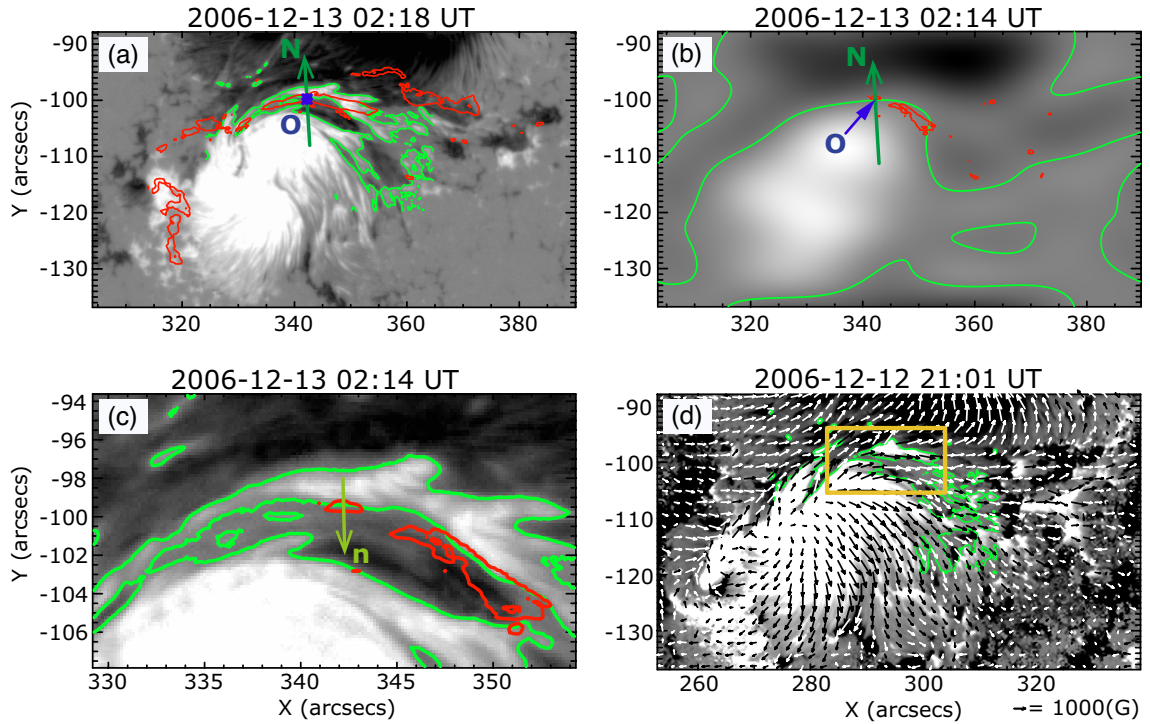
Figure 2.5: Images of AR 10930, and vectors $\boldsymbol{N}$ and $\boldsymbol{n}$ on the flare-trigger region in Event 1. The grayscale part of the image corresponds to positive/negative polarity of the LOS magnetic field (Stokes-V/I), and green lines indicate the PIL. Red contours show the Ca-line brightenings. (a) The Stokes-V/I image at 02:18 UT, when the sheared flare ribbons first appeared. The format is same to Figure 2.4. (b) The smoothed Stokes-V/I image and the normal vector $\boldsymbol{N}$ at the point O. (c) The enlarged image of (unsmoothed) Stokes-V/I and the normal vector $\boldsymbol{n}$ at 02:14 UT. (d) The vector magnetic field obtained by SP at 20:30 UT December 12. Shear angle θ_0 was calculated as the angle averaged over the yellow square. The gray scale intensity scale is ± 0.1 (Stokes-V/I) in (a - c), and at $\pm 1000\ G$ in (d).

The measurement results $\varphi_e = 180° − 186°$ and $\theta_0 = 70° \pm 15°$ are plotted in Figure 2.6. Because the extent of the last Ca-line brightening was different from each event, it was not able to perform the statistical procedure for φ_e. From these results, the flare trigger region governing Event 1 possesses an OP-type magnetic structure, consistent with the KB12 model.
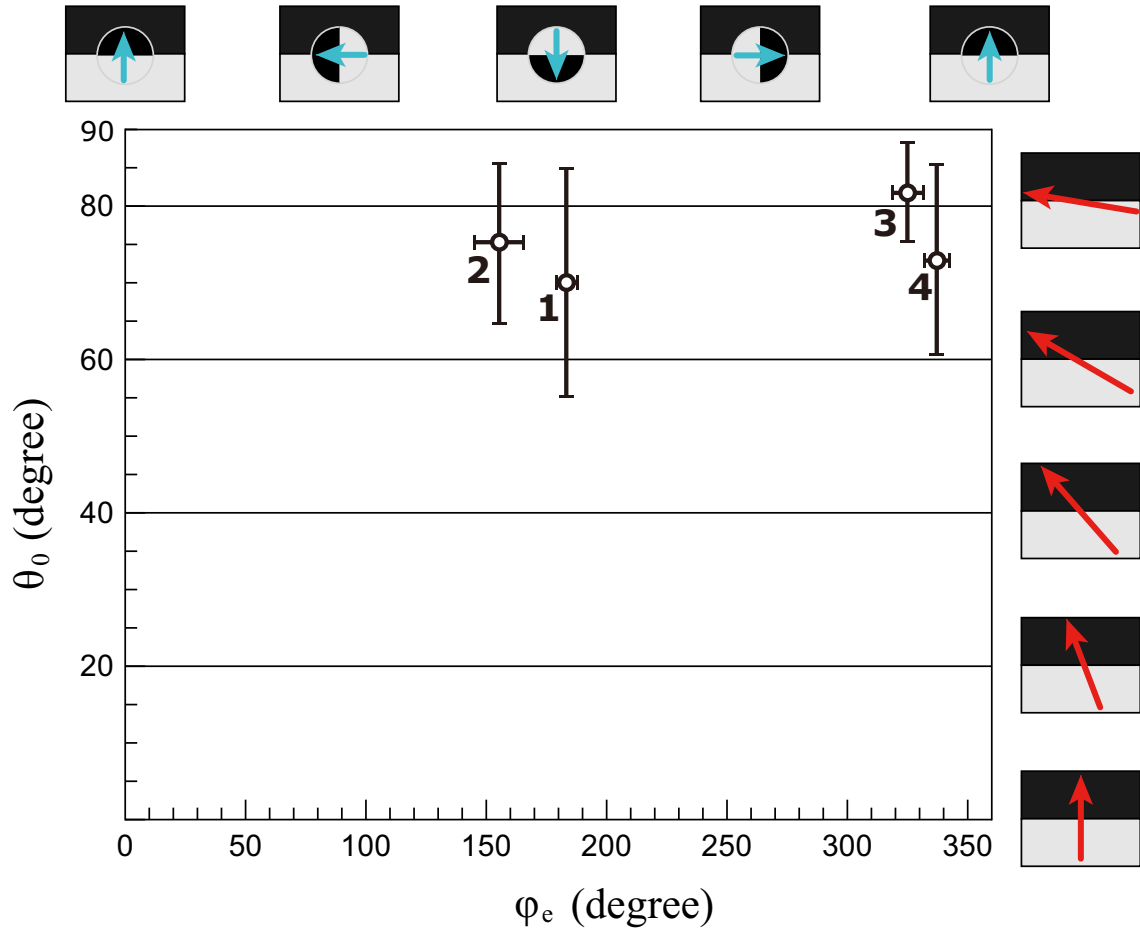
Figure 2.6: Summary plot of the actual flare trigger condition for Events 1 - 4. The black crosses indicate the shear angle θ_0 and the azimuth φ_e. White circles indicate the mean of θ_0 and φ_e for each Events 1 - 4 case. The error-bars show the standard deviation of θ_0 and the range of φ_e. Right hand and top images indicate the averaged sheared field and orientation of flare trigger region, respectively.

2.4.2 Event 2: X1.5 Flare in AR 10930 on 2006 December 14

Figure 2.7 shows the time variations of Stokes-V/I and Ca-line brightenings during pre-flare phase in the X1.5 flare (Event 2) region. The initial flare ribbons were sheared (panel (d)) and the trigger region is likely located within the yellow circle. In fact, a small-scale, isolated, positive magnetic island is detectable in the negative sunspot (indicated by the yellow arrow in panel (a)). This island slowly approached the PIL after 20:57 UT and a small Ca-line brightening appeared on its southeast side. The small island appeared to be of the OP-type magnetic configuration. Panels (e - h) are filtergrams of the Ca-line; enlarged views of the region bordered by the yellow square in panel (b), in which panels (e, h) are imaged at the time of (b, c), respectively. The yellow arrows in panel (b, e) indicate the continuous bright segments, which rapidly moved southeast, as shown in panel (f). The small, fiber-like structure on the Ca-line was weakened in panel (g), whereas an elongated Ca-line brightening along the PIL immediately prior to the flare onset was likely caused by current sheets forming in the chromosphere as the flux rope ascended, as noted by Kusano & Bamba et al. [2012]. From these observed features, we inferred that the small magnetic island is a flare trigger for the X1.5 flare.

Figure 2.7: Temporal variations of Stokes-V/I preceding the X1.5 flare (Event 2) on December 14, 2006. Panels (a - d) are formatted identically to Figure 2.4, except the intensity level of Ca-line is 1500 DN. The bottom four panels (e - h) show the sequential images of filtergrams on the Ca-line between times for panels (b, c). The FOV corresponds to the region bordered by yellow square in panel (b), and the yellow arrows in panels (b, e) indicate the same bright point.

The Stokes-V/I images corresponding to the LOS magnetic field, PIL, and Ca-line brightening of the initial flare ribbons in Event 2 at 22:03 UT are plotted in Figure 2.8 (a). Panel (b) shows the smoothed Stokes-V/I image. This image is formatted identically to Figure 2.5 (b), and the trigger point O and vector $\boldsymbol{N}$ at 21:49 UT were defined as in Figure 2.5. Panel (c) is an enlarged image of the trigger region, including the local normal vector $\boldsymbol{n}$. The azimuth $\varphi_e = 145° - 167°$ is the angle between vectors $\boldsymbol{N}$ and $\boldsymbol{n}$. Panel (d) shows the final magnetic vector field prior to the flare onset, collected by SOT/SP (17:31 UT December 14). The averaged shear angle $\theta_0 = 75° \pm 11°$. Therefore, the small isolated positive pole satisfies the conditions of the OP-type flare trigger region.
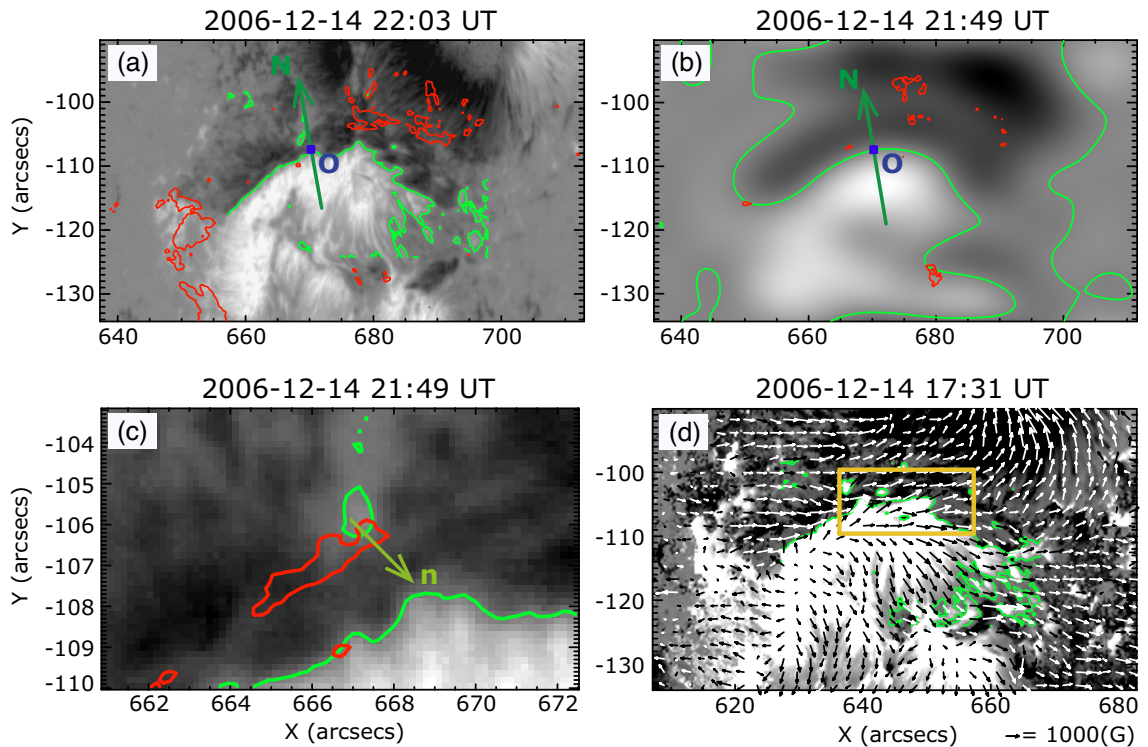
Figure 2.8: Images from which the azimuth φ_e and the shear angle θ_0 were measured in Event 2. The respective panels are formatted as for Figure 2.5. The trigger point O, vectors $\boldsymbol{N}$ and $\boldsymbol{n}$ were defined as shown in panels (a - c) of Figure 2.5. Shear angle θ_0 was measured in the region indicated by the yellow square in panel (d). The intensity scale is ± 0.1 in panels (a - c), and at ± 1000 G in panel (d).

2.4.3   Event 3: M6.6 Flare in AR 11158 on 2011 February 13

The time variations of Stokes-V/I and Ca-line brightening are shown in Figure 2.9. The initial, sheared flare ribbons were seen in panel (f), and it is suggested that the flare trigger region is located within the yellow circle. There was a wedge-like structure in the yellow circle, and it was formed between 13:00 UT to 15:00 UT February 13. Unfortunately, there was a data-gap between 13:00 UT to 15:00 UT, Toriumi et al. [2013] showed that small positive patches transported from northern positive region to the region which is indicated by yellow arrow in panel (a) between 07:00 UT to 16:00 UT. They have suggested that the flux transportation created the wedge-like structure. In fact, we can see the Ca-line brightening along the path of the flux transportation from 15:00 UT to 16:00 UT (panel (b)). Once the Ca-line brightening disappeared after the flux transportation stopped (panel (c)), isolated Ca-line brightening was again observed in the northeast side of the PIL (panel (d)). This Ca-line brightening was weakened just before the M6.6 flare onset as seen in panel (e), then the sheared flare ribbons suddenly appeared (panel (f)). In the RS-type simulation of the KB12 model, the electric current intensity on the current sheet, which is formed between the pre-existing sheared fields and the RS-type magnetic field, was weakened just prior to eruption of twisted flux ropes. Therefore, the observed features of pre-flare brightenings and flare ribbons are consistent with the RS-type flare trigger scenario.
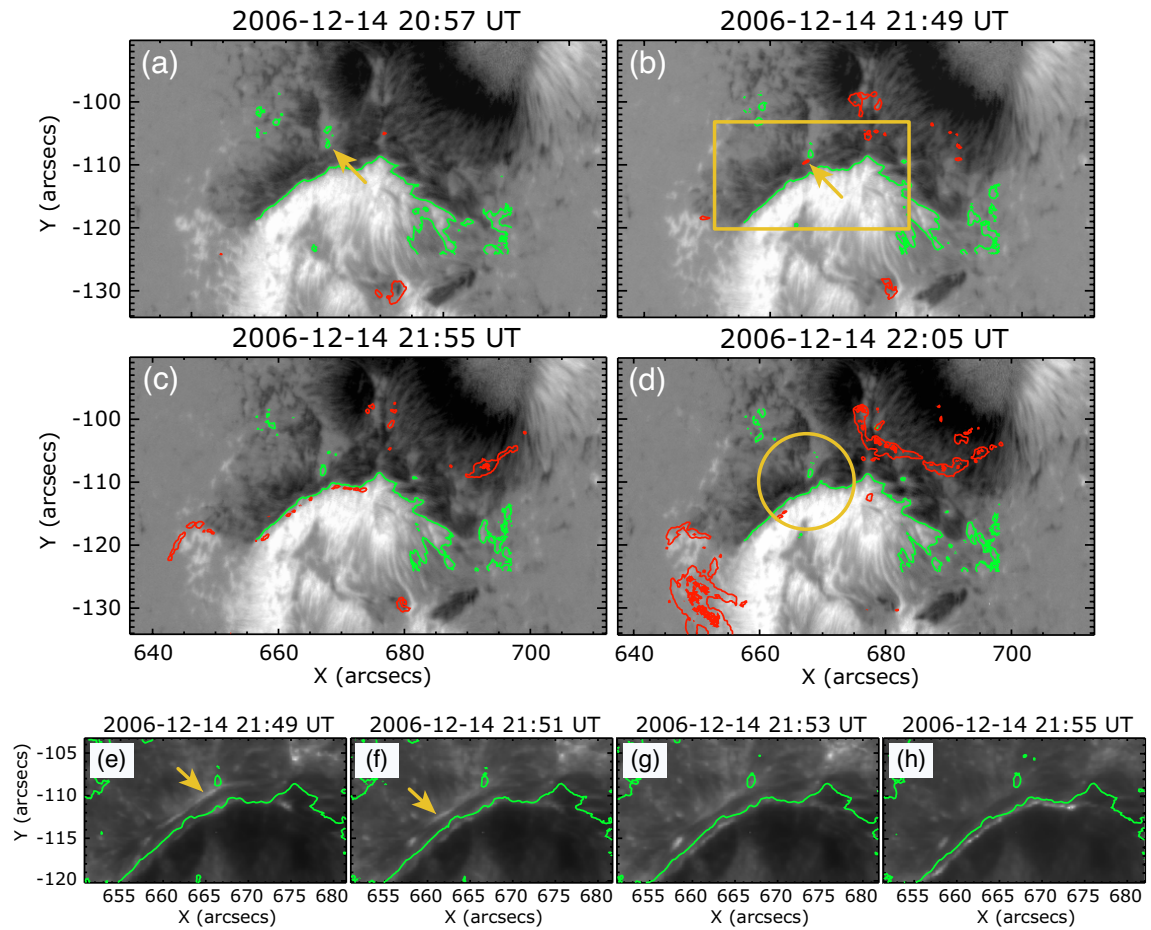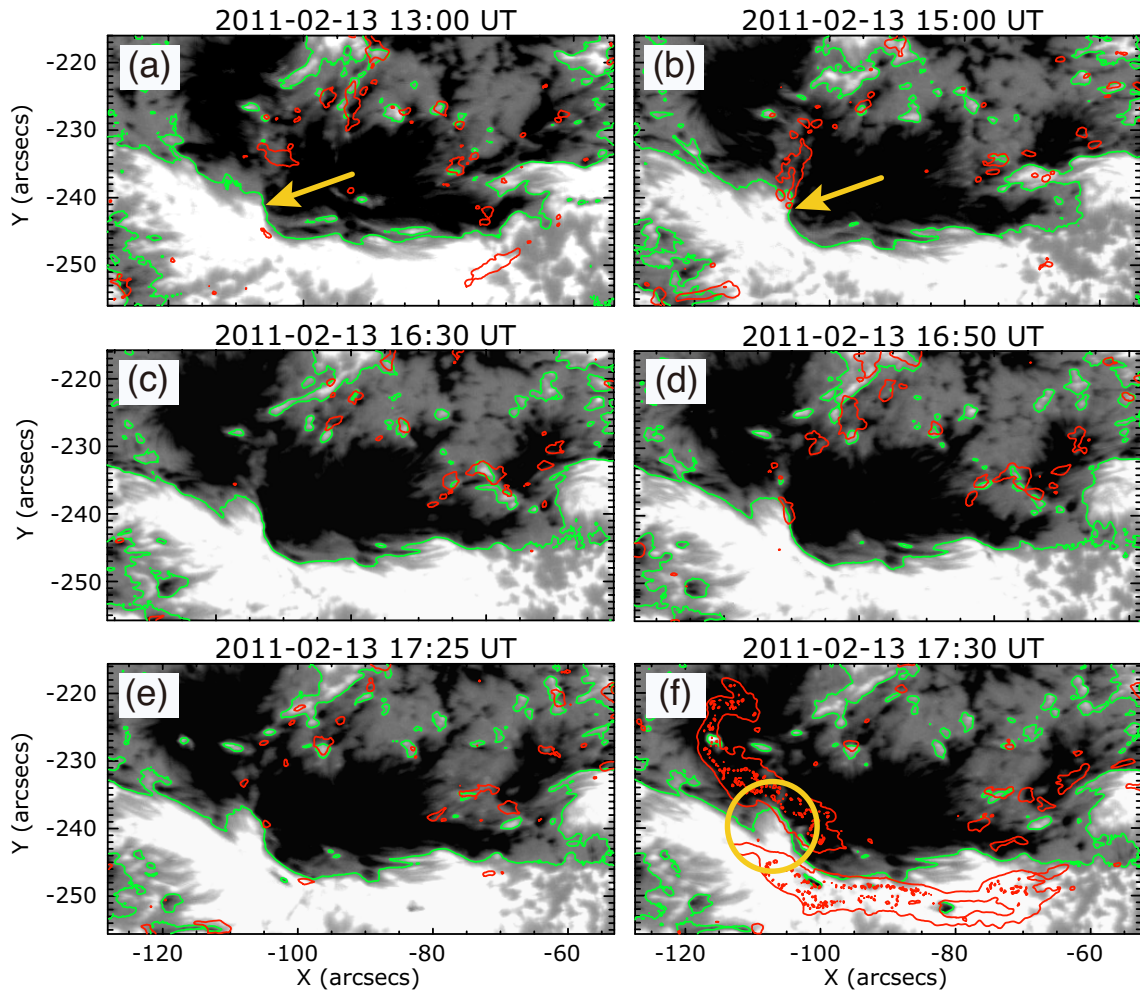
Figure 2.9: Temporal variations of Stokes-V/I preceding the M6.6 flare (Event 3) on February 13, 2011. Panels (a-f) are formatted identically to Figure 2.4, except the intensity levels of Stokes-V/I and Ca-line are $\pm$ 0.1 and 1250 DN, respectively. Yellow arrow in panels (a, b) indicate a wedge-like structure, which is inferred to be a flare trigger field.

The smoothed and original Stokes-V/I images, an enlargement of the flare-trigger region, and the vector magnetogram are shown in Figure 2.10. The panels in this figure are formatted identically to the corresponding panels in Figure 2.5. The origin of the flare trigger region O and normal vectors $\boldsymbol{N}$ and $\boldsymbol{n}$ at 17:25 UT were defined as shown in panels (a - c). Panel (d) shows the vector magnetogram at 16:16 UT on February 13. From these images, the azimuth and shear angles were measured as $\varphi_e = 318° - 331°$ and $\theta_0 = 82° \pm 7°$. These measurements (also plotted in Figure 2.6) indicate that Event 3 was triggered by a small-scale bipole field with the RS-type characteristics, again consistent with the KB12 model.
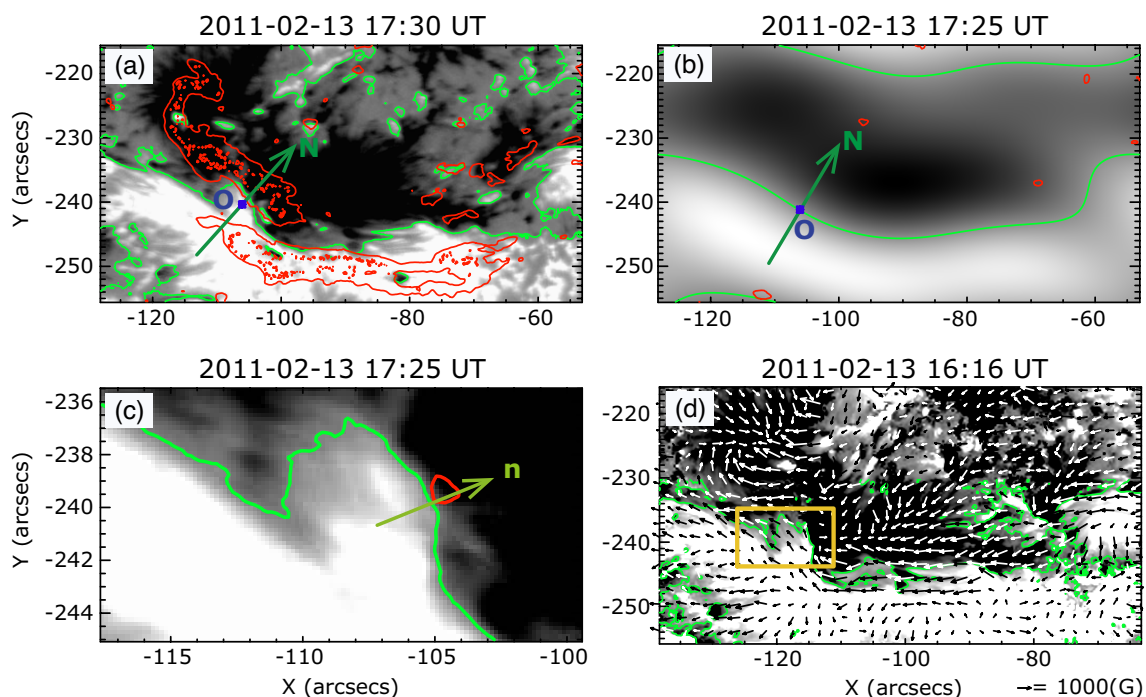
Figure 2.10: Images from which the azimuth φ_e and the share angle θ_0 were measured in Event 3. The format is identically to Figure 2.5. The intensity scale is ± 0.1 in panels (a - c), and $\pm 1000\ G$ in panel (d).

2.4.4 Event 4: X2.2 Flare in AR 11158 on 2011 February 15

The upper four panels of Figure 2.11 show the time variations of Stokes-V/I signals and Ca-line brightening in Event 4. The lower two panels show the filtergrams of the Ca-line overlaid with PILs (green lines), formatted as for the lower four panels of Figure 2.7. The right columns are enlarged images of the regions bounded by yellow squares in the left columns.

Because the initial flare ribbons had a sheared structure (R1 and R2 in Figure 2.11 (e)), the trigger is inferred to locate in the region bordered by the yellow square, as shown in Figure 2.11 (e). A small, wedge-like structure was observed at the center of the ribbon in panel (f). This structure began as a small, isolated island of positive magnetic field with Ca-line brightening shown in panels (a, b). This small, positive island slowly developed into the small, wedge-like structure of panels (c, d) from 22:30 UT on February 14, and the Ca-line brightenings brightened on the northwest of PIL (whose polarity orientation reverses to the northeastward shear of the AR; see panel (d)). Thus, it is inferred that this small, wedge-like structure triggered the X2.2 flare.
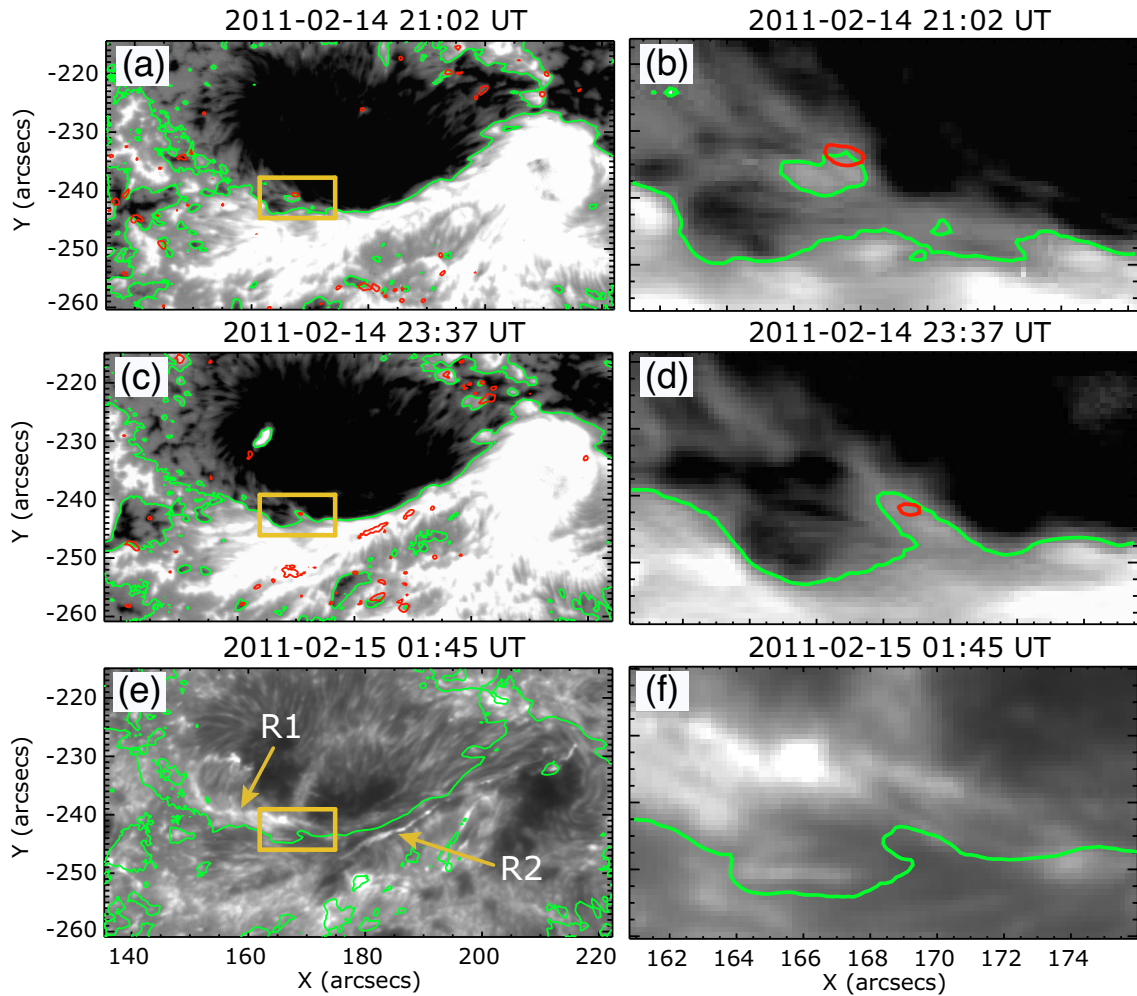
Figure 2.11: Time variation of Stokes-V/I preceding the X2.2 flare (Event 4) on February 15, 2011. Panels (a-d) are formatted identically to Figure 2.4, except the intensity levels of Stokes-V/I and Ca-line are $\pm$ 0.1 and 1250 DN, respectively. Panels (e, f) are Ca-line filtergrams which are formatted identically to Figure 2.7 (e - f). The right column shows enlarged images around the flare trigger regions (bordered by yellow squares in the left columns).

The trigger origin O and vectors $\boldsymbol{N}$ and $\boldsymbol{n}$ at 00:40 UT were defined as in Figures 2.12 (b, c), respectively. Panel (d) displays the vector magnetogram prior to flare onset, observed at 06:46 UT, February 14. The yellow square delineates the region of averaged shear angle θ_0. The azimuthal and shear angles were measured as $\varphi_e = 334° - 342°$ and $\theta_0 = 73° \pm 13°$ and are plotted in Figure 2.6. Because the SP was observed approximately one day preceding the onset of the X2.2 flare, during which time magnetic helicity was continuously injected into the AR (Jing et al. [2012]), the measured θ_0 likely underestimates the shear angle in the flare phase. Nevertheless, magnetic structural characteristics and the Ca-line brightenings before the flare imply that the central flaring region is the RS-type.
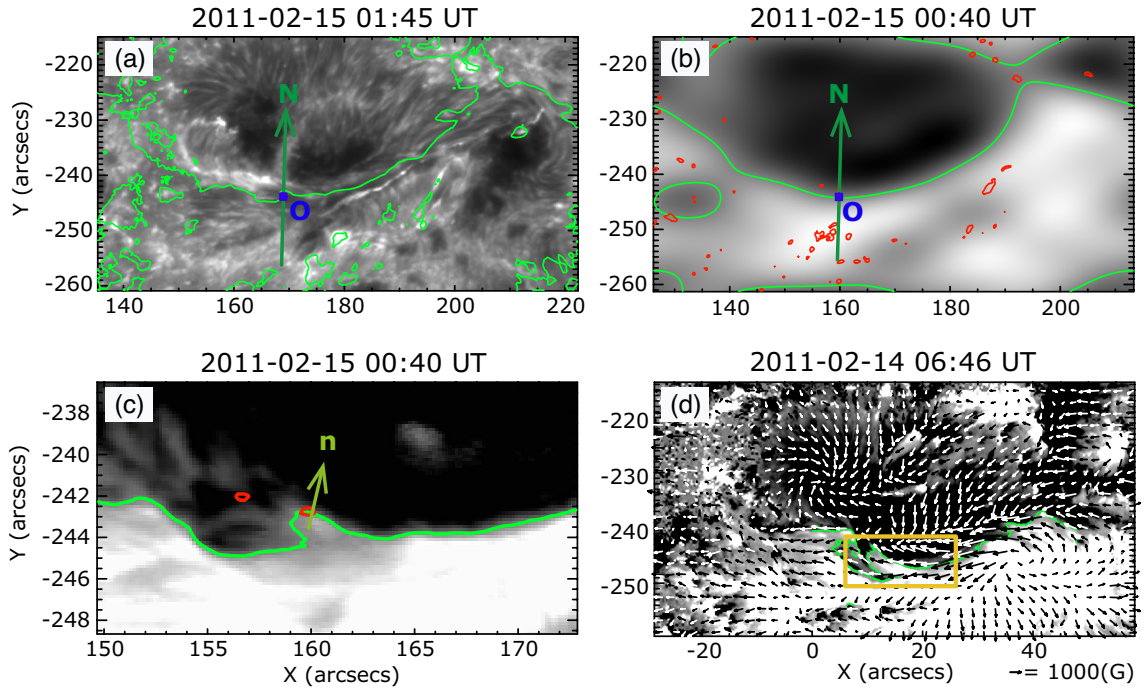
Figure 2.12: Images from which azimuth φ_e and shear angle θ_0 were measured in Event 4. Panels (b - d) are formatted as described for Figure 2.5 (b - d), respectively. Because the initial flare ribbons were very faint, the grayscale shows the filtergram on Ca-line in panel (a), where the green curves indicate the PILs. The intensity scale is ± 0.1 in panels (a - c), and $\pm 1000 \, G$ in panel (d).

2.5   Summary

In this chapter, we analyzed four major flares in order to examine the existence of either the OP- or RS-type flare trigger regions proposed in the KB12 model. Using Hinode/SOT data, we quantitatively measured the typical two parameters of the KB12 model. The results of this study are summarized below.

1. All of the flares were characterized by the flare trigger region at the center of the initial sheared flare ribbons. Intermittent Ca-line brightenings, which may indicate internal magnetic reconnection between the small-scale bipole field (i.e. the flare trigger field) and the large-scale sheared magnetic field in the flaring AR, were also observed on the PILs of the trigger region for several hours preceding the flare onset. Moreover, the flare trigger fields potentially responsible for solar flares could be classified as either OP or RS.

2. The spatial size of the flare trigger region, the timing of the pre-flare brightening in Ca-line, and its duration were different between all the events, as summarized in Table 2.3. It is inferred that these differences depends on how magnetic fields in the pre-flare phases were likely to be less stable. We will discuss it in Chapter 4.

	Flare Trigger Region	Last Pre-flare Brightening	
Event No.	Spatial Size	Start Timing [a]	Duration
1	$\sim 35''$	$\sim 15\ min.$	$\sim 15\ min.$
2	$\sim 2''$	$\sim 20\ min.$	$\sim 2\ min.$
3	$\sim 5''$	$\sim 50\ min.$	$\sim 50\ min.$
4	$\sim 3''$	$\sim 60\ min.$	$\sim 10\ min.$

Table 2.3: Summary of the size of the flare trigger region and timing and duration of the last pre-flare brightening.

---

[a]It indicates how long ago did the Ca-line brightening start before the flare onset time.

Chapter 3

Flare Trigger Process in a Complicated Active Region

3.1 Introduction

In Chapter 2, we analyzed four flares and confirmed the existence of the flare trigger regions. The flare trigger regions satisfied qualitative and quantitative conditions which were predicted by the KB12 model. Those active regions had relatively simple magnetic structure, and two flare ribbons clearly appeared on both sides of the PIL which shaped single line. However, solar flares generally occur in complicated active regions that are very different from the simple structure assumed in the simulation results of the KB12 model. Therefore, it is important to examine whether the theoretical model is applicable to more complex ARs. In this chapter, we analyzed the X1.0 flare occurred on 2014 October 25. This flare showed three flare ribbons, and it is difficult to infer the location of the trigger region in the AR and to reveal the physical process of the flare trigger. Here, we aim to clarify the X1.0 flare trigger process to examine whether the KB12 model is applicable even to a complicated AR, through the same procedure which is summarized at the beginning of Chapter 2.

3.2 Overview of SDO/HMI, AIA and Data Description

We used both Hinode and SDO (Solar Dynamics Observatory, Pesnell et al. [2012], Figure 3.1) data. SDO is developed and launched by NASA as a mission of Living With a Star (LWS) program. It regularly observes the full disk of the Sun ($2000'' \times 2000''$) from a geosynchronous orbit with the altitude of $\sim 35,800\ km$. SDO equips HMI (Helioseismic and Magnetic Imager, Schou et al. [2012]) and AIA (Atmospheric Imaging Assembly, Lemen et al. [2012]). HMI is a 14 cm aperture telescope, and it observes polarization states Stokes-I, Q, U and V using a polarization calibration unit and quarter-wave plate (Schou et al. [2012]), with photospheric the Fe I line (6173 Å). Calibrated LOS magnetograms, vector magnetograms, and Dopplergrams can be downloaded from the Joint Science Operations Center (JSOC)[1] in the Stanford University. AIA is four 20 cm aperture, dual-channel, normal-incidence telescopes, and it observes the solar atmosphere in ten EUV and UV channels, which are sensitive to $6,000\ K$ to 1 MK. In this chapter, we used AIA images taken in 1600 Å (continuum and C IV line), 171 Å (Fe IX line), 131 Å (Fe VIII and Fe XXI lines), and 304 Å (He I I line) and the region of the atmosphere and the related formation temperatures of each wavelength are summarized in Table 3.1. Using the combination of these images, we investigated the spatial and temporal correlation between the pre-flare brightenings and the initial flare ribbons in lower temperature (in 1600 Å and 304 Å) and the pre-existing magnetic arcade in the corona seen in cool and hot temperature (171 Å and 131 Å). The spatial resolution and the cadence were $1''$ and 45 $sec.$ for HMI, $1.5''$ and 12 $sec.$ for AIA (except AIA 1600 Å where the cadence was 24 $sec.$).

---

[1]http://jsoc.stanford.edu/ajax/lookdata.html
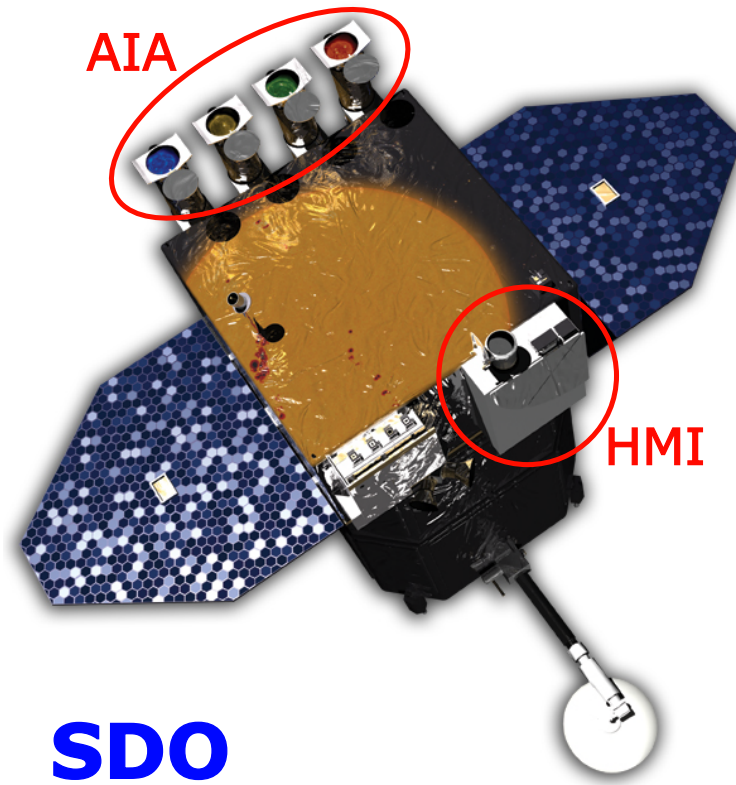
Figure 3.1: The SDO satellite (copyright by NASA).

Wavelength	Primary Ion(s)	Region of Atmosphere	Temperture (log (T))
304Å	He II	chromosphere, transition region	4.7
1600Å	continuum, C IV	upper photosphere, transition region	5.0
171Å	Fe IX	upper transition region, quiet corona	5.8
131Å	Fe VIII, Fe XXI	transition region, flaring corona	5.6, 7.0

Table 3.1: Summary of SDO/AIA wavelength. The information in this table are excerpted from Lemen et al. [2012].

AR NOAA 12192 was the biggest sunspot in the solar cycle 24[2]. The AR stayed on the solar surface through three Carrington rotations, and it was numbered NOAA 12172 (and 12173), 12192, and 12209 in each rotation. AR 12192 had the most complicated magnetic structure including a δ-type sunspot in which several umbras share a penumbra. The major bipole extended from east to west, and emerging flux was seen in the middle of the major biple. More than 130 flares, which were larger than C1.0, including six X-class flares occurred in the AR during disk passage. Table 3.2 lists the X-class flares that occurred in the AR.

Date	Start Time (UT) [a]	GOES X-ray Class	Location [b]
2014 October 19	04:17	X1.1	S14E64
2014 October 22	14:02	X1.6	S14E13
2014 October 24	21:07	X3.1	S22W21
2014 October 25	16:31 [c]	X1.0	S10W22
2014 October 26	10:04	X2.0	S14W37
2014 October 27	14:02	X2.0	S16W56

Table 3.2: List of X-class flares that occurred in AR 12192

In this chapter, we focused on the X1.0 flare on 2014 October 25, which is the fourth X-class flare in the AR, because the flare showed three flare ribbons and it is inferred that the magnetic structure related to the flare was complicated. The flare was simultaneously observed by Hinode and SDO. The AR was located at S10° - 20° latitude and W15° - 25° longitude during the flare. Figure 3.2 shows the soft X-ray light curve observed by GOES (1 - 8 Å and 0.5 - 4 Å). The onset time of the X1.0 flare was 16:31 UT, and it is indicated by the blue vertical line in Figure 3.2. The C9.7 flare occurred at 15:44 UT before the X1.0 flare onset, and it is shown by the red vertical line.

---

[2]As of 2015 December 22.

[a]The start time is defined from X-ray observations of GOES satellite.

[b]http://www.solarmonitor.org/

[c]This time was defined from X-ray observation by the RHESSI satellite (Reuven Ramaty High Energy Solar Spectroscopic Imager; Lin et al. [2002]) because GOES likely released wrong time for this event.
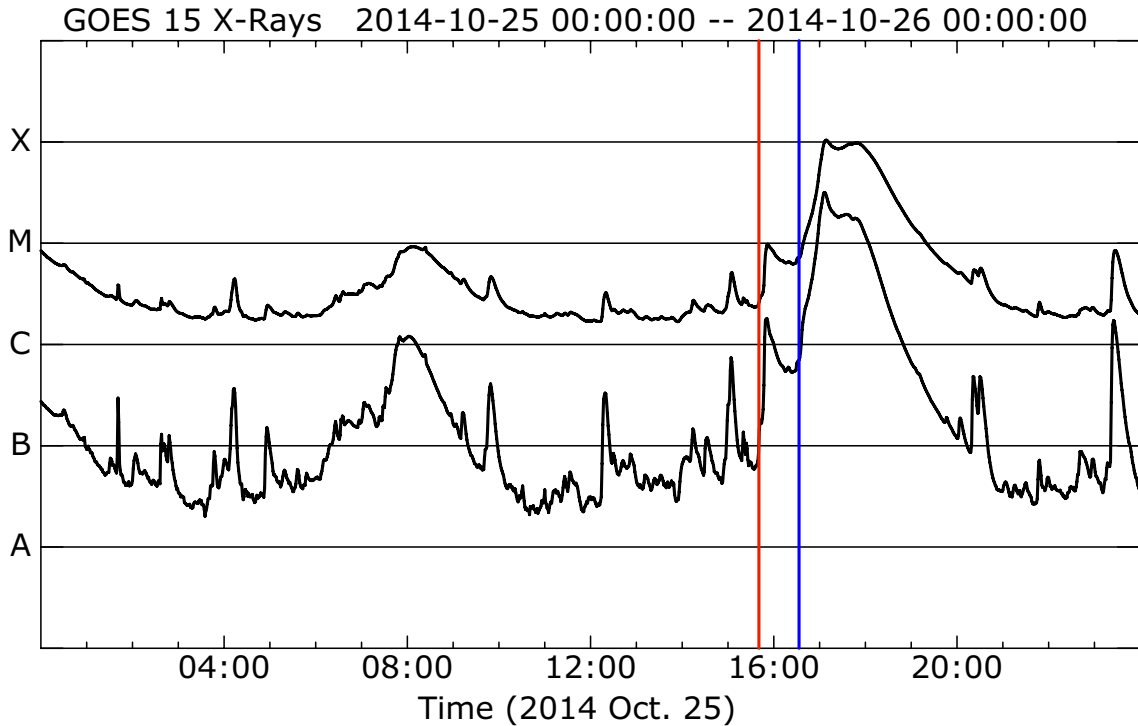
Figure 3.2: The soft X-ray light curve observed by GOES (1 - 8 Å and 0.5 - 4 Å) from 00:00 UT on October 25 to 00:00 UT on October 26. The red/blue vertical line indicates the onset time of the C9.7 (15:44 UT)/X1.0 (16:31 UT) flare, respectively.

We analyzed SDO data from 13:00 UT to 18:00 UT on October 25. We used HMI filter magnetograms taken at 6173 Å (Fe I line), AIA 1600 Å (continuum and C IV line), 171 Å (Fe IX line), 131 Å (Fe VIII and Fe XXI lines), and 304 Å (He II line) filtergrams. We investigated the spatial and temporal correlation between the evolution of the photospheric magnetic field, brightening in the chromosphere and the transition region, and coronal loops. We also used Hinode/SOT data to precisely analyze the magnetic field. We used the full polarization states (Stokes-I, Q, U, and V) at 6301.5 and 6302.5 Å (Fe I line) with a sampling of 21.5 mÅ, obtained by SP. The SP scanned the central part of the AR at 11:00 - 11:33 UT with a $164'' \times 164''$ FOV, and the spatial resolution was $0.3''$.

3.3 Analysis Method

3.3.1 Method of SDO/HMI, AIA Analysis

We basically used the analysis method developed in Section 2.3 (Bamba et al. [2013]). The analysis method was developed for Hinode/SOT data, but it has examined the applicability to the SDO data sets in Bamba et al. [2014]. They analyzed M6.6 in AR 11158 (Event 3 in Chapter 2), which was observed by both Hinode and SDO, as a sample event, using the same analysis method. As a result, they confirmed the consistency of the qualitative and quantitative features of the flare trigger field with both satellite data sets. Here, we briefly summarize the procedures of the analysis method.

We used HMI level 1.5 LOS magnetograms (`hmi.M_45s` series) and AIA level 1 (`aia.lev1_euv_12s` and `aia.lev1_uv_24s` serieses) data, which are already calibrated by dark-current subtraction and flat fielding. We first calibrated all the HMI LOS magnetograms and all the AIA images using the `aia_prep` procedure in the SSW package. By this process, spectral fluctuations were removed, and the images were rotated so that the solar EW and NS axes are aligned with the horizontal and vertical axes of the image, respectively. Moreover, LOS magnetograms and AIA images were resampled to the same size because the pixel scales of HMI and AIA are different. Thus, the axes and the pixel scales of HMI and AIA became the same, and the positions of the LOS magnetograms and AIA images were aligned, because both HMI and AIA take images of the full disk of the Sun. Next, we chose a HMI LOS magnetogram and an AIA image closest in time, and these two images were superimposed onto each other. We drew PILs and strong brightening contours in an AIA images onto the LOS magnetograms at each time.

3.3.2　Method of Hinode/SOT Analysis

The SP scan data were calibrated using the `sp_prep` procedure in the SSW package assuming the Milne-Eddington atmosphere. The inversion code MEKSY was adopted and the 180° ambiguity in the vector magnetograms in resolved using the AZAM utility. This procedure is same to that was explained in Section 2.2.

We investigated the distribution of the magnetic shear over the AR before the flare onset, using a vector magnetogram obtained by SP. We first calculated the potential field using the `fff` procedure in the `nlfff` package (developed by Dr. Fan Yuhong) in SSW. Then we measured the angles between a potential field vector $\boldsymbol{B}_p$ and a transverse field vector $\boldsymbol{B}_t$ in each pixel, and we defined these angle as the relative shear angle χ. The relative shear angles are defined between $\pm\,180°$, where 0° means vectors $\boldsymbol{B}_p$ and $\boldsymbol{B}_t$ are oriented in the same direction. The direction of vector $\boldsymbol{B}_t$ deviates from vector $\boldsymbol{B}_p$ to counter-clockwise (clockwise) when the magnetic helicity is positive (negative) and the value of χ is positive (negative). We colorized the relative shear angles as shown in Section 3.4.3.

3.4　Results

3.4.1　Overview of the Flares

The temporal evolution of the strong brightenings and flare ribbons in AIA 1600 Å images, which is sensitive to the emission from upper chromosphere and the transition region, are shown in Figure 3.3. We can see those brightenings with the magnetic field structure in Figure 3.4, where the white/black region indicates positive/negative polarity of the LOS magnetic field. The green lines and the

red contours denotes the PIL (line of 0 G) and outlines the strong brightenings (2000 DN) in AIA 1600 Å, respectively. The green lines in Figure 3.3 are the same to these in Figure 3.4. The intruding positive polarity (IPP) and the weak negative region N2 are located between the major bipole P1 and N1, as seen in Figure 3.4 (a).

We can also seen the small brightening B1, which is indicated by the yellow arrow in panel (a) of both Figures 3.3 and 3.4. This brightening was seen intermittently at the west side of the IPP at 14:48 - 14:58 UT. Another brightening B2 was also seen in the IPP (panel (a)). The initial flare ribbons of the C9.7 flare appeared about one hour later as shown in panel (b), and the three ribbons CR1, CR2, and CR3 were clearly seen. B1 disappeared at the last minute before the C9.7, while B2 enhanced as CR2 in panel (b). It suggests that B1 was caused by the local magnetic reconnection occurred at the west side of the IPP before the C9.7 flare. The three-ribbons of the C9.7 flare did not propagate to the outer side with time.

Once the three-ribbons CR1, CR2, and CR3 disappeared, a faint ribbon-like brightening remained at the region where CR1 was seen. It is clearly seen in Figure 3.3 (c). Panel (d) show the initial flare ribbons from the X1.0 flare that appeared about one hour after the C9.7 flare. In this phase, the XR1 (positive ribbon) and the XR2 (negative ribbon) at the west side/middle were more clearly seen that the XR3 (negative ribbon) at the east side. These three-ribbons slowly grew as shown in panel (e) at 16:35 - 17:10 UT. Especially, XR1 and XR3 got longer to the southward and northward directions, respectively, and these propagated to outer side with time. XR2 disappeared first in the late phase while XR1 and XR3 remained more than one hour after the onset, as seen in panel (f).
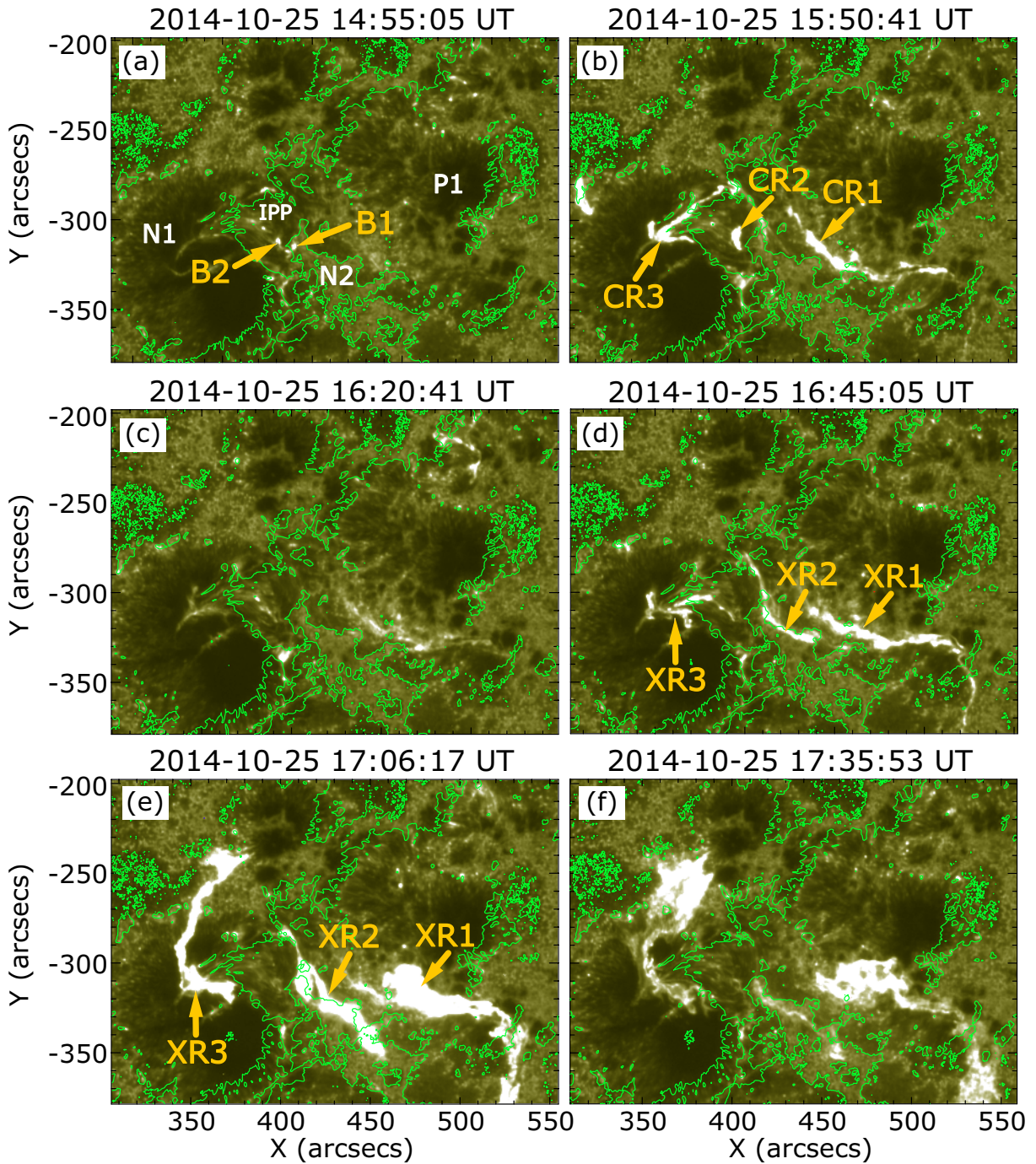
Figure 3.3: Temporal evolution of the strong brightenings and the flare ribbons in AIA 1600 Å images. Green lines indicate the PILs in HMI LOS magnetograms at each time. The intensity scale range is $0 - 2000\ DN$. Strong brightenings seen in before the flare onset, three-ribbons of the C9.7 and the X1.0 flares are indicated by yellow arrows.
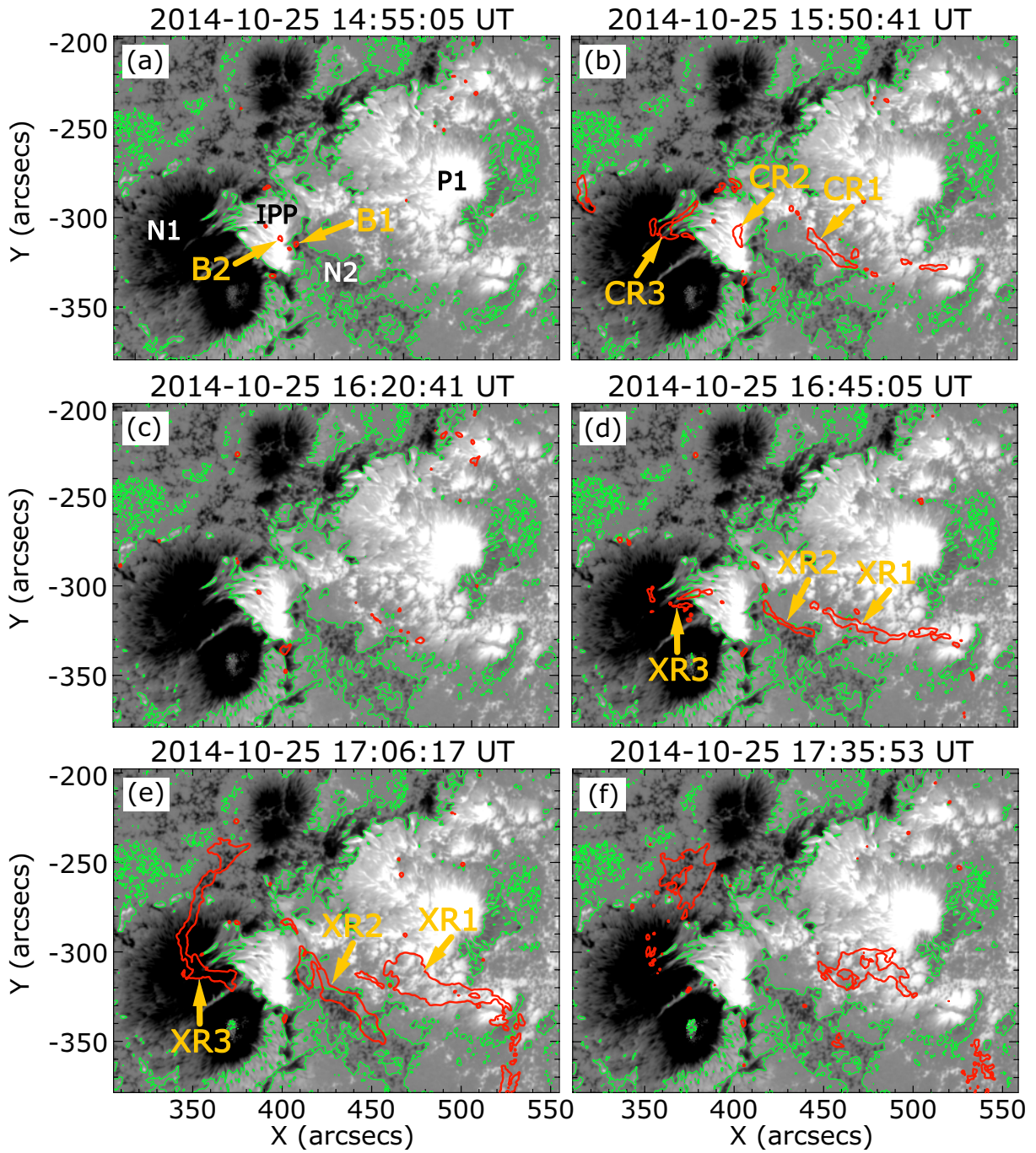
Figure 3.4: Temporal evolution of the HMI LOS magnetic field at $\pm$ 1000 G. White/black indicates positive/negative polarity of the LOS magnetic field, and green lines indicate the PILs. The red contours outline the strong brightenings in AIA 1600 Å images with an intensity of 2000 DN. The time of each panel is same to that of the AIA 1600 Å images. Panels (a - f) show the same features as Figure 3.3 together the LOS magnetic field.

Figure 3.5 shows the AIA 304 Å images of the same FOV and almost the same time to Figures 3.3 and 3.4. The filament, fibril, and strong brightenings in the chromosphere and the transition were seen in the central part of the AR. The PILs are over plotted only in panel (a). The intermittent brightening B1 is indicated by the yellow arrow in panel (a), and it was seen at the west side of the IPP as well as shown in AIA 1600 Å image of Figure 3.3 (a). The brightening B1 shapes a small arcade striding over the local PIL at the west side of the IPP, and it was clearly seen at 14:48 - 15:09 UT although it persisted from 13:00 UT to just before the onset of the C9.7 flare. It suggests the existence of a small magnetic arcade which connects IPP and N2 in the west side of the IPP. In contrast, the brightening B2 connected IPP and N1 where CR3 will appears, as clearly seen in Figure 3.5 (a) and (b). The three flare ribbons appeared on both sides of the filament located along the PIL between the positive (P1) and negative (N2) region as shown in panel (b). The positive ribbon CR1 remained more clearly than that seen in Figure 3.3 (c), and the negative ribbon CR3 also remained in Figure 3.5 (c). The three flare ribbons of the X1.0 flare (XR1, XR2, and XR3) gradually appeared from 16:30 UT and grew as seen in panels (d) and (e). The post flare loop connecting XR1 and XR2 was seen in panel (f), although XR2 had already disappeared at the time.
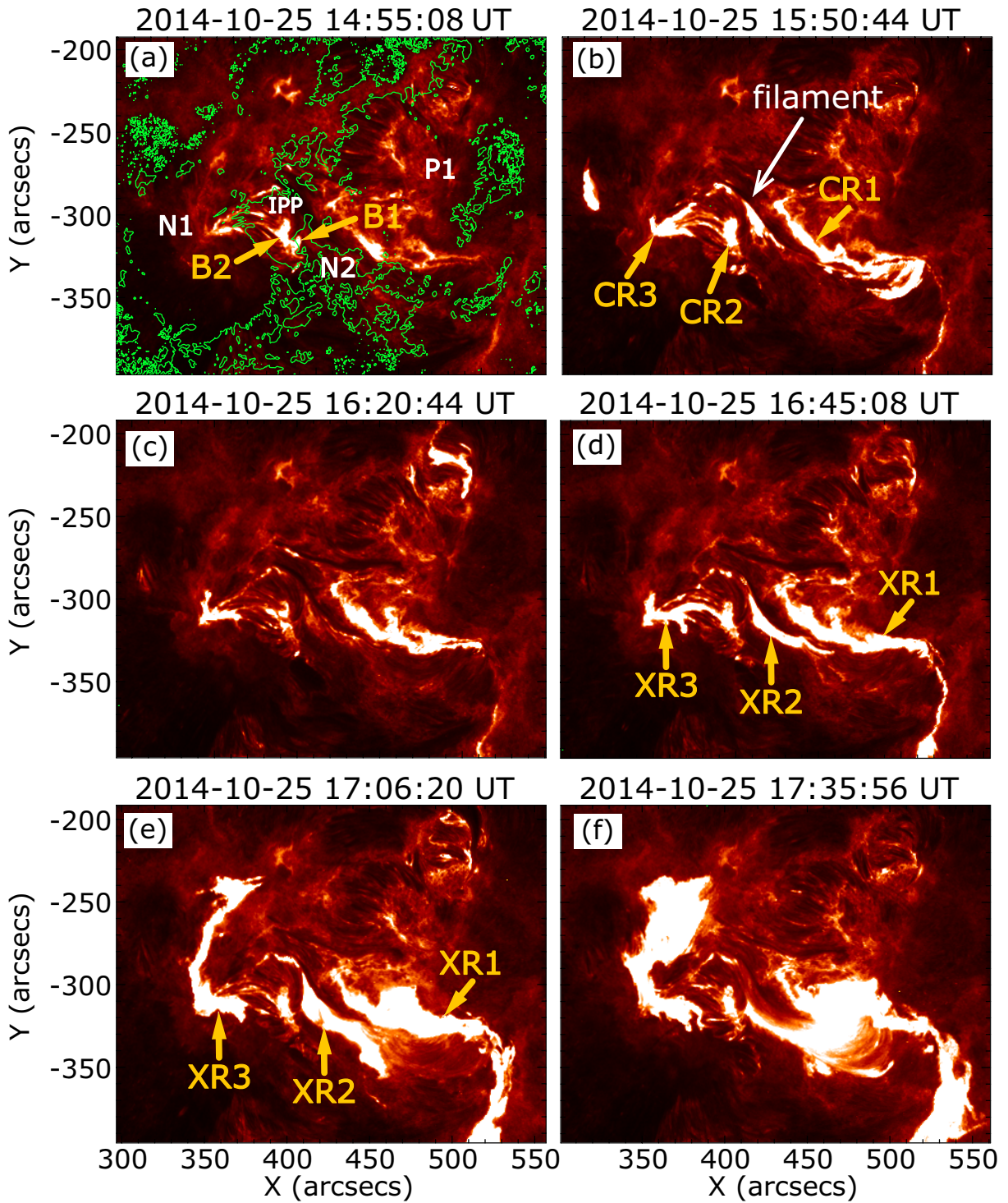
Figure 3.5: Temporal evolution of the strong brightenings and the flare ribbons in AIA 304 Å images. The PILs are over plotted with green lines on panel (a). The intensity scale range is $0 - 1000 \ DN$. Panels (a - f) show almost the same features as Figure 3.3, but the brightening B1 shapes a small loop striding over the local PIL at the west side of the IPP. Moreover, CR1 remained more clearly than that seen in Figure 3.3 (c), and CR3 also remained in panel (c).

The coronal loops in AIA 131 Å images are shown in Figure 3.6, with the PILs only shown in panel (a). In the early phase (panel (a)), bright loops L1 and L2 connected IPP - N1 and P1 - N1, respectively. IPP have continuously emerged from October 19, and it was gradually intruding into the negative sunspot (N1). Therefore, it is suggested that the strong electric current layer was formed in between L1, L2, and the overlying magnetic arcade which connects P1 and N1 (it locates higher/outer than L2). In this layer, coronal loops could be heated by magnetic reconnection between L1, L2, and overlying magnetic arcades, even though the field directions of magnetic arcades do not differ strongly. The foot points of L1 and L2 brighten as seen in Figure 3.5 (a). These heated loops L1 and L2 were gradually enhanced before the C9.7 flare onset as seen in Figure 3.6 (b). Once the intensity of the coronal loops decreased at 15:15 - 15:35 UT, loops L1 and L2 became bright again and three flare ribbons of the C9.7 flare appeared as indicated by the yellow broken lines in panel (c). Then the intensity of the coronal loops continuously increased until the onset time of the X1.0 flare (panel (d)). The coronal loops connecting XR1 and XR2 enhanced (panel (e)), then XR3 appeared and faint coronal loops connected XR1 and XR3 as can bee seen in panel (f).
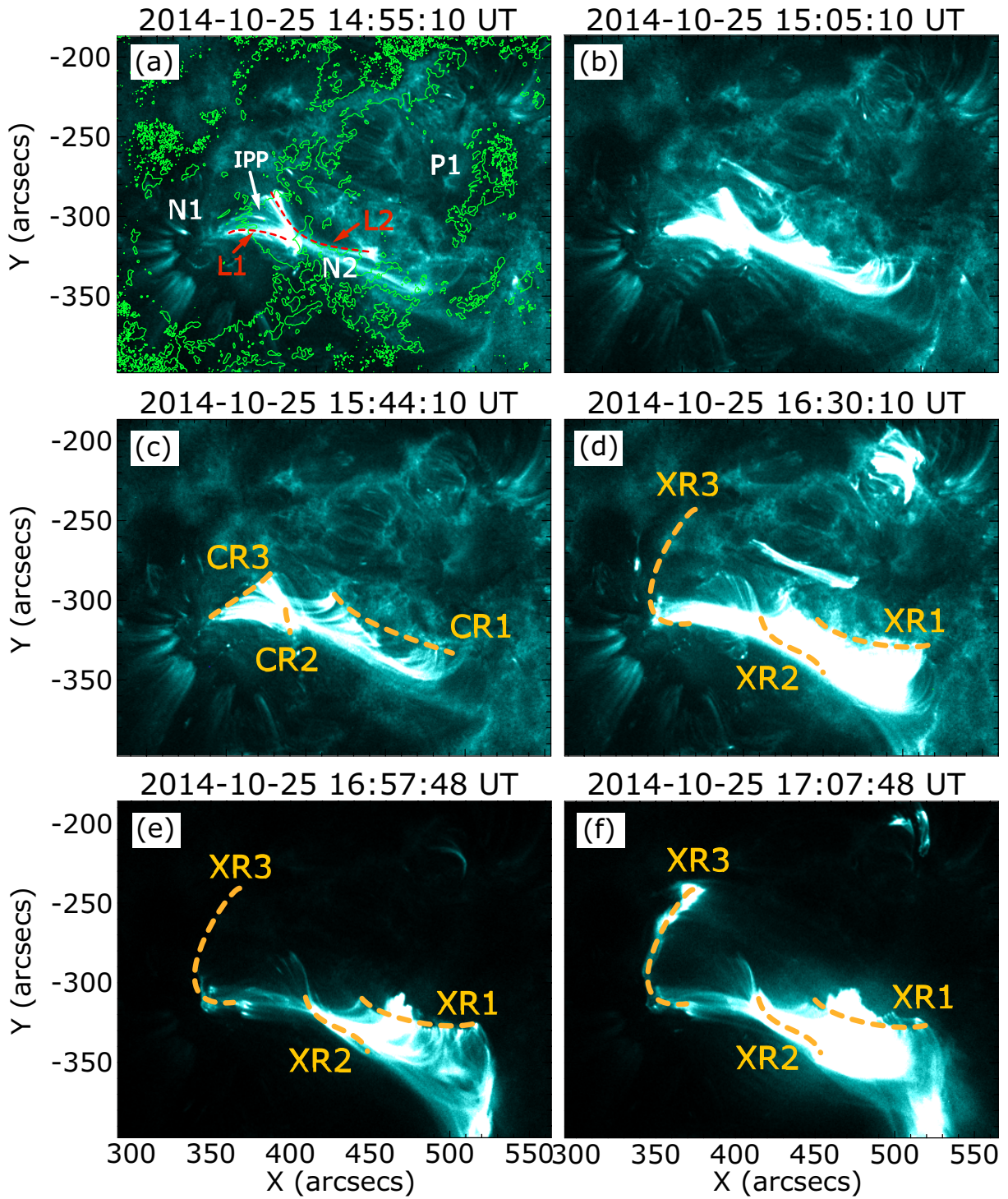
Figure 3.6: Temporal evolution of the coronal loops in AIA 131 Å images. The PILs are over plotted with green lines in panel (a). The intensity scale is $0 - 500 \ DN$. Bright loops L1 and L2, which connect IPP - N1, are outlined by red broken lines in panel (a). The yellow broken lines roughly illustrate the locations of the C9.7 three-ribbons in panel (c) and the locations of the X1.0 three-ribbons in panel (d - f).

Interestingly, the tether-cutting magnetic reconnection process (c.f. Section 1.4 and Figure 1.4) was clearly seen before the C9.7 flare. Figure 3.7 shows AIA 171 Å images with a similar FOV to Figures 3.3 - 3.6. The PILs are over plotted only in panel (a), and there was a filament channel as indicated by the red arrow in panel (b). We could see faint loop structures which intersect at point O, and small brightenings frequently moved along these faint loops as illustrated by sky blue arrows in panel (b). These motion were seen from 13:00 UT, and it became enhanced from 15:00 UT. The motion along the loops became faster and the loops slightly expand between 15:40 UT and 16:00 UT (panel (c)). CR1 and CR3 of the C9.7 flare appeared at the foot points of the faint loops as illustrated by the red broken lines in panel (d), and we could see the three flare ribbons in the chromosphere at that time (see Figure 3.5 (b)). It suggests that the tether-cutting magnetic reconnection occurred in the C9.7 flare around the point O.
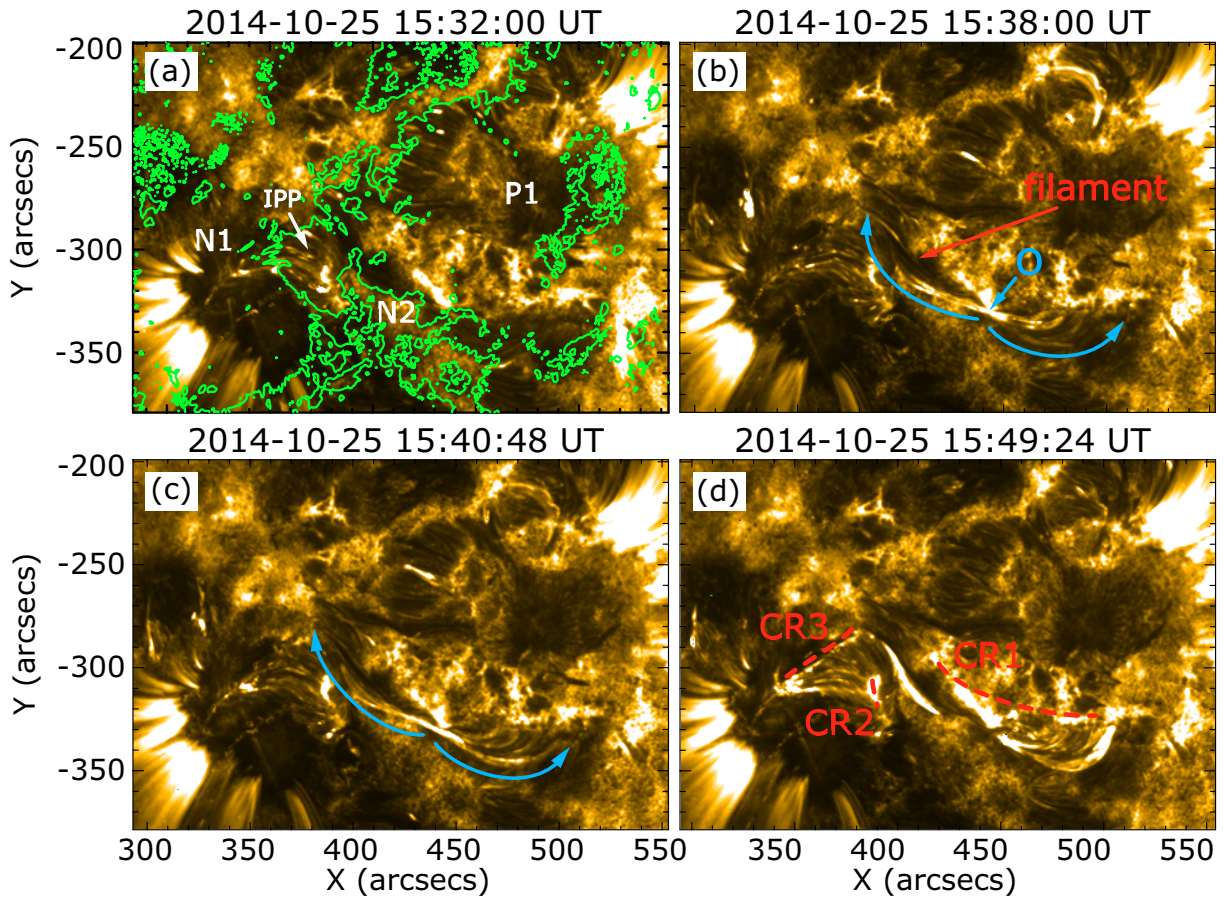
Figure 3.7: Tether-cutting magnetic reconnection on AIA 171 Å images. The FOV is almost the same to in Figures 3.3 - 3.6. The intensity scale range is $0 - 5000$ DN, and the PILs are over plotted as the green lines in panel (a).

3.4.2　Locations of the Flare Ribbons

Figure 3.8 shows the distribution of the C9.7 and the X1.0 flare ribbons. The background images are HMI LOS magnetograms at the onset time of the X1.0 flare (16:31 UT), and the green lines indicate the PILs. The red contour outlines strong brightenings in AIA 1600 Å, such as the flare ribbons at 15:50 UT (just after the C9.7 flare onset), in both panels (a) and (b). The blue contours outline strong brightenings at 16:45 UT (before the X1.0 flare onset) in panel (a) and at 17:06 UT (after the X1.0 flare onset) in panel (b), respectively. XR1, XR2, and XR3 correspond to the X1.0 flare ribbons which were shown in Figure 3.3 (e). The initial flare ribbons of the C9.7 flare and the X1.0 flare are seen in panel (a), and XR1 and XR3 of the X1.0 flare located slightly at the outer side of CR1 and CR3 of the C9.7 flare. XR1 and XR3 expanded to outer side after the X1.0 flare onset as seen in panel (b), while the CR1 and CR3 of the C9.7 flare did not propagate to the outer side with time, as noted in Section 3.4.1. It suggests that the X1.0 flare was an extension of the C9.7 flare, and the X1.0 flare was driven by reconnection of magnetic field anchored in the outer region of the C9.7 flare ribbons.
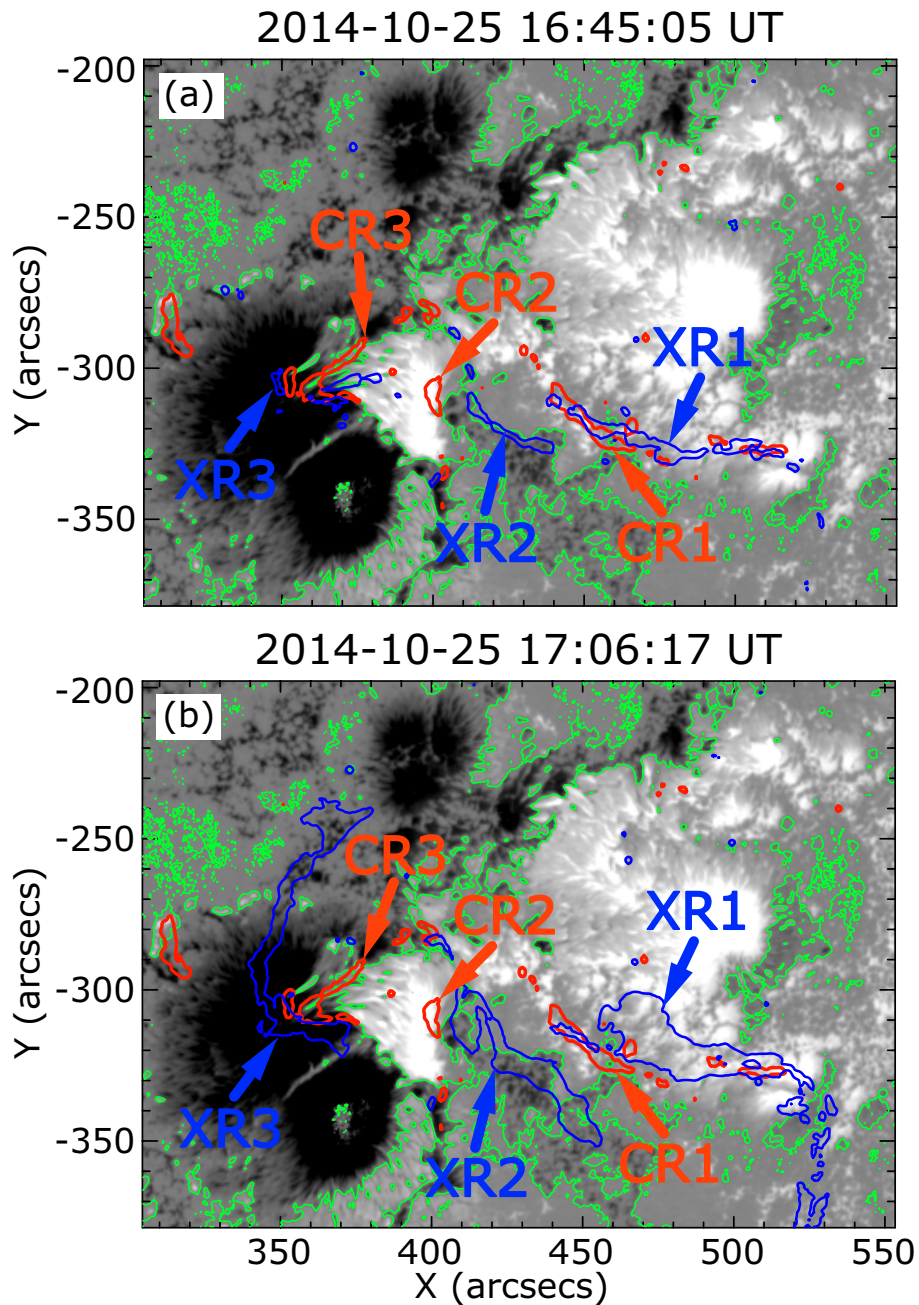
Figure 3.8: The flare ribbons of the C9.7 and the X1.0 flares. The background images are HMI LOS magnetograms at the onset time of the X1.0 flare (16:31 UT on 2014 October 25). The green lines are the PILs, and the red/blue contours outline the flare ribbons in AIA 1600 Å images. The red contour shows the CR1, CR2, and CR3 of the C9.7 flare at 15:50 UT in both panels (a) and (b). The blue contour outlines the initial flare ribbons (XR1, XR2, and XR3) of the X1.0 flare at 16:45 UT in panel (a), while the enhanced flare ribbons at 17:06 UT is outlined in panel (b).

3.4.3 Features of the Magnetic Fields

The vector magnetic field in the central part of the AR was observed by Hinode/SP between 11:00 and 11:44 UT, as shown in Figure 3.9. The background is LOS magnetic field, and the white/black region indicates positive/negative polarity. Green lines indicate the PILs. The transverse magnetic field vectors are over plotted on LOS magnetic field by the red arrows. The transverse field vectors were strongly sheared along the PIL located between P1 and N2. It suggests that the major magnetic helicity along the PIL of the AR was negative. In contrast, the vectors at the west side of the IPP were locally toward the northwest side over the PIL. It is consistent with the shape of the brightening B1 seen in Figure 3.5 (a). In a word, the local magnetic field at the west side of the IPP had positive magnetic helicity, which is opposite to the major magnetic helicity along the PIL.

It was more clearly seen in Figure 3.10, which shows the relative shear angle χ, defined as the angle between the potential field and the transverse field vectors at each point. The black lines indicate the PILs. The relative shear angle χ along the flaring PIL (between P1 and N2) and that in the west side of the IPP are correspond to the shear angle θ_0 of the AR and the azimuth φ_e of the small magnetic disturbance in the KB12 model, respectively (c.f. Section 1.5, Figures 1.7 and 1.8). Obviously, χ was around -90° (blue) along the PIL but χ was 90° (red) at the west side of the IPP. Therefore, the distribution of the relative shear angle χ suggests that the west side of the IPP satisfied the RS-type flare trigger condition of the KB12 model.
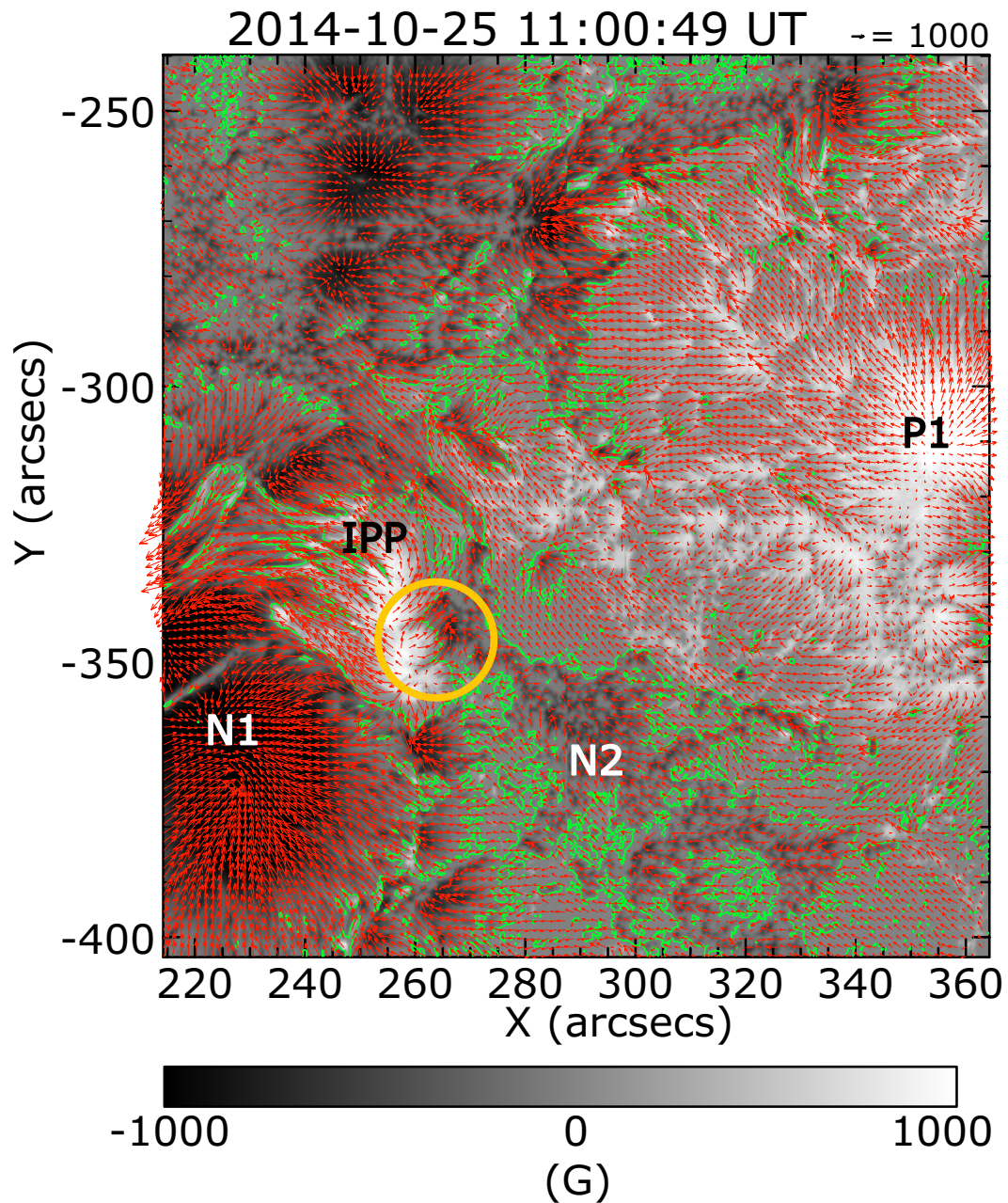
Figure 3.9: The vector magnetic field obtained by Hinode/SP at 11:00 - 11:33 UT on 2014 October 25. The grayscale part corresponds to the positive/negative polarity of the LOS magnetic field at $\pm 2000\ G$. Green lines indicate the PILs, and the red arrows are the transverse magnetic field vectors at each point.
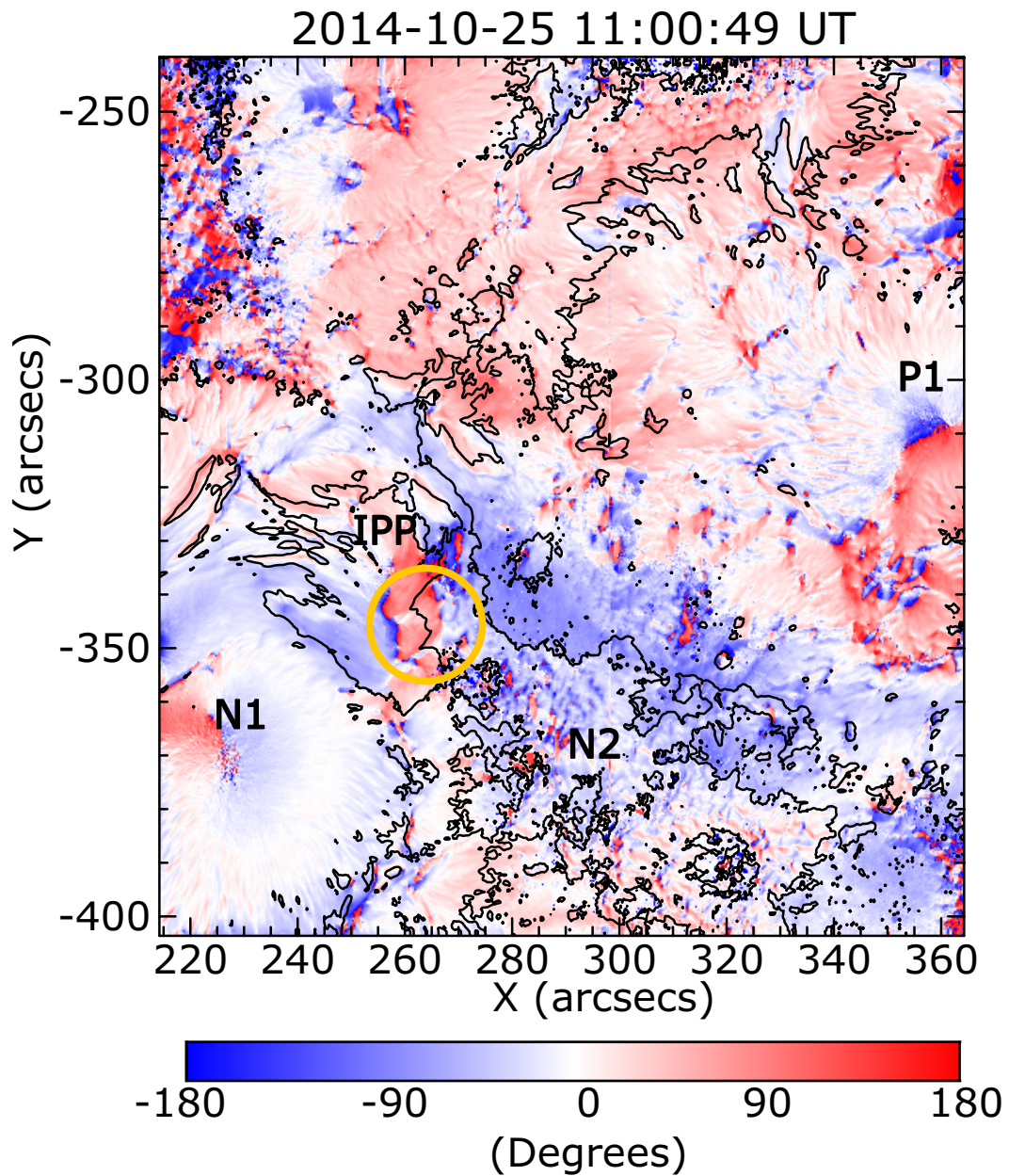
Figure 3.10: Distribution of the relative shear angle χ which is defined as the angle between the potential field vector $\boldsymbol{B}_p$ and transverse field vector $\boldsymbol{B}_t$. The black lines are the PILs which are indicated by green lines in panel (a). The red/blue region corresponds to positive/negative values of χ, i.e. the magnetic helicity. The region where the strong brightening were seen is pointed out by the yellow circle in both panels (a, b).

According to the KB12 model, shear cancellation between the large-scale magnetic field and a small-scale magnetic field can trigger a flare, and the pre-flare brightenings should be observed during the shear cancellation in the flare trigger region. In our case, strong brightenings in the chromosphere and the transition region were observed in the west side of the IPP, where the magnetic shear was reversed to the shear of the global magnetic field along the flaring PIL. It is consistent with the theoretical prediction of the KB12 model. Therefore, we concluded that the west side of the IPP is the location where the flares were triggered in the AR.

3.4.4   Conceivable Scenario and Comparison with the KB12 Model

Here, we considered a flare trigger scenario of the C9.7 and the X1.0 flares from the observed results and the coronal magnetic field structures. We derived the coronal magnetic field using the non-liner force-free field (NLFFF) extrapolation method developed by Inoue et al. [2014]. Figure 3.11 shows the coronal magnetic field lines anchored on the flare ribbons of the C9.7 and the X1.0 flares. The grayscale is an HMI LOS magnetogram taken at 15:00 UT October 25. The red/blue contours outline the brightening (700 DN) in AIA 1600 Å, such as the flare ribbons, observed at 15:50 UT/17:03 UT. The blue and orange tubes represent the coronal magnetic field lines. The orange tubes anchor on the ribbons of the C9.7 flare (CR1, CR2, and CR3), as shown in panels (a, b). In contrast, the sky blue tubes anchor on the three ribbons of the X1.0 flare (XR1, XR2, and XR3), as in panels (c, d). The small magenta tubes indicated by the magenta arrow are the local magnetic field lines at the west side of the IPP.

Obviously, the sky blue magnetic arcades anchored on XR1 - XR3 were located at the outer side of the orange arcades anchored on CR1 - CR3. It is consistent with the observed results shown in Figure 3.8. Moreover, the small magenta

arcades at the west side of the IPP were located under the orange arcades. The magenta arcades satisfied the RS-type flare trigger condition as mentioned in Section 3.4.3. Therefore, the following scenario is conceivable.

First, magnetic shear cancellation occurred between the orange arcades and the magenta arcades at the west side of the IPP, and it caused strong brightening over the region (B1 in Figure 3.5 (a)). This process corresponds to internal magnetic reconnection in the RS-type trigger process of the KB12 model (c.f. Section 1.5). Then the magnetic pressure decreased over the region, and the orange arcades collapsed inward and the first flare reconnection occurred. The plasma flow, which is suggestive of the tether-cutting reconnection, was observed as shown in Figure 3.7 at the time. This was the C9.7 flare and it showed the three flare ribbons CR1, CR2, and CR3 at the foot points of the orange arcades. The long twisted flux ropes (anchor on CR1 and CR3) might be produced under the sky blue arcades by the C9.7 flare reconnection, and it gradually rose upwards and vertically stretched the overlying sky blue arcades. After the magnetic pressure decreased sufficiently, the X1.0 flare reconnection of the sky blue arcades (XR1 - XR2 and XR1 - XR3 arcades) occurred. It produced the other three flare ribbons (XR1, XR2, and XR3) at the foot points of the sky blue arcades. XR1 and XR3 elongated to the southward and northward as magnetic reconnection propagates to the outer field lines. Therefore, the C9.7 and the X1.0 flares were triggered by the magenta arcades at the west side of the IPP in a two-step flare trigger process.
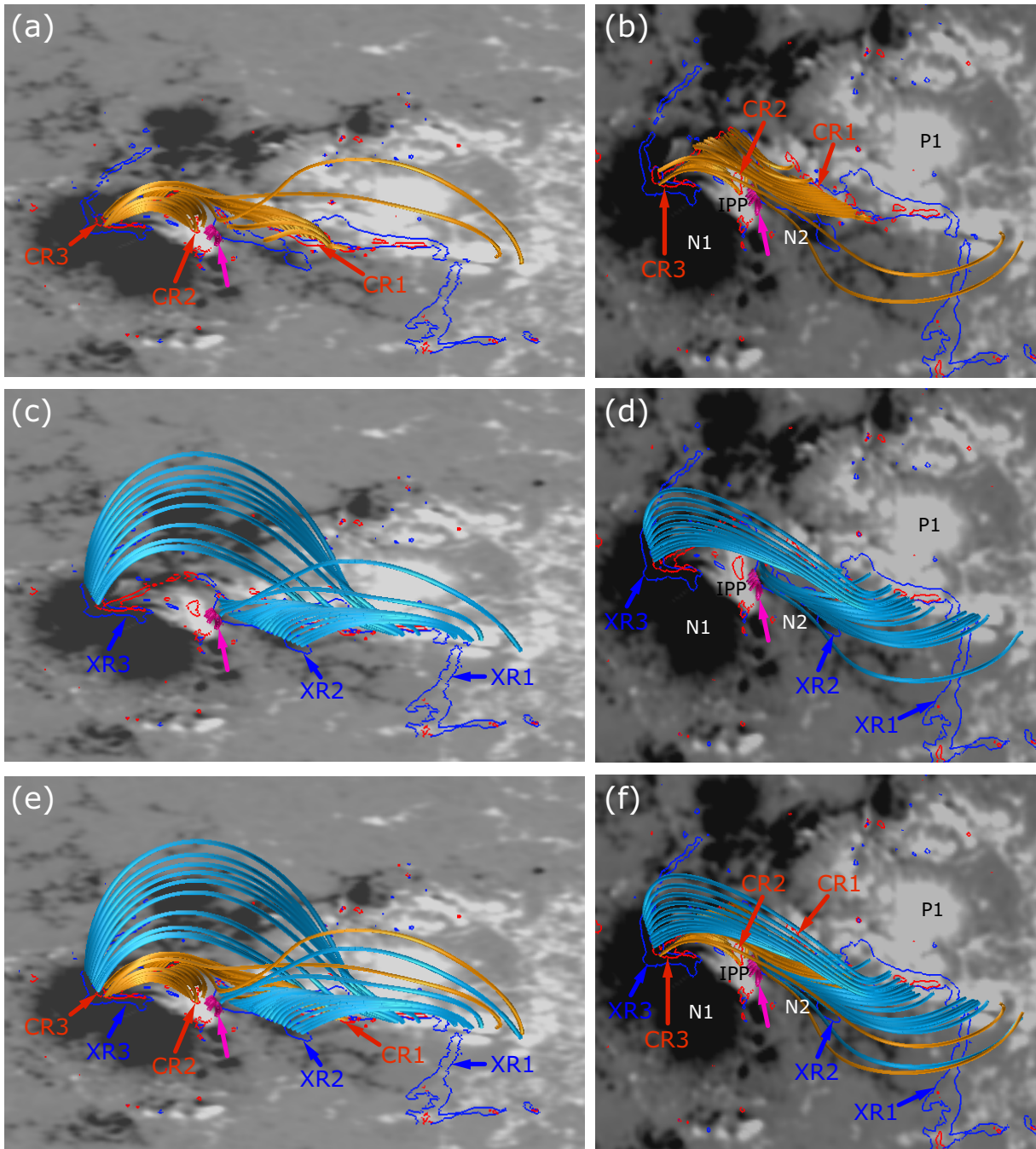
Figure 3.11: The magnetic field lines extrapolated by the NLFFF method (performed by Dr. Satoshi Inoue). The left/right columns show a bird's eye view/top view of the same image. The grayscale images are HMI LOS magnetogram taken at 15:00 UT, October 25. The red/blue contour outlines strong brightenings (700 DN) in AIA 1600 Å such as flare ribbons on 15:50 UT/17:03 UT. The small magenta tubes indicated by the magenta arrows are the local magnetic field lines at the west side of the IPP. The orange/sky blue tubes indicate the coronal magnetic field lines anchored to thee flare ribbons of the C9.7/X1.0 flare in panels (a, b)/(c, d), respectively. All the coronal magnetic field lines are plotted in panels (e, f).

3.5　Summary

In this chapter, we analyzed the C9.7 and the X1.0 flares occurred on 2014 October 25, in AR 12192, in order to evaluate the consistency of the observable features, which are predicted by the KB12 model, to magnetically complicated AR. We analyzed SDO/HMI, AIA, and Hinode/SP data, and compared the analysis results to the coronal magnetic field structures derived by the NLFFF extrapolation method. As a result, we found that the west side of the IPP was the RS-type flare trigger region, and that the C9.7 and the X1.0 flares were triggered in a two-step flare trigger process. In addition, we observed plasma flows suggestive of the tether-cutting magnetic reconnection at almost the same time to the C9.7 flare. Therefore, we confirmed that the flare trigger mechanism is understandable with the KB12 model (and the tether-cutting model), even in a complicated AR.

In the KB12 model, they injected a small-scale bipole field just above the major PIL of the AR, and we actually found the flare trigger fields above the PILs in Chapter 2. In this chapter, we found that the west side of the IPP, which we concluded the flare trigger region, was located slightly off of the major PIL. Therefore, our result indicate that a RS-type flare trigger can work even if the flare trigger region is away from the major PIL in the AR. We will later discuss the displacement between flare trigger field and flaring PIL in Section 4.3.

Chapter 4

Discussion

We confirmed in Chapters 2 and 3 that the photospheric magnetic field structures, which were seen before several flare events, were consistent with those predicted by the KB12 model. We had used pre-flare brightenings, as in the Ca line, as a marker of flare trigger region, in the sense that it is caused by internal reconnection between the pre-existing magnetic field and small-scale flare trigger field. In the first part of this chapter, we quantitatively discuss the plasma dynamics over the flare trigger region with the aim to confirm that pre-flare brightenings are caused by the internal reconnection. We analyze the X1.6 flare occurred in the great sunspot AR 12192, because we have spectroscopic data for the chromosphere over a small bipole field, which seems to be the flare trigger field. We investigate the time variation and the spatial distributions of the velocity of the chromospheric plasma over the flare trigger field, and discuss the plasma dynamics.

In the second part, we propose the possibility of an additional parameter that should be considered as flare trigger conditions. In Chapter 2, we demonstrated that the topological structures of the magnetic field are crucially important for flare triggering, as predicted by the KB12 model. However, the conditions under which flares erupt remain unknown, because the topological properties of magnetic field cannot explain why flares occur at the specific time. Therefore, we

quantitatively investigate the temporal evolution of the "total magnetic flux" in the flare trigger region before the flare onset, and discuss whether it can be a critical parameter.

In the final part, we consider the question: Can various flare events be explained by the KB12 model? We statistically investigate various flare events, which were observed by SDO, and classify them into six independent types based on whether the events satisfy the observable features proposed by the numerical simulation of the KB12 model. From the statistical classification, we discuss the consistency between the events that did not satisfy the observable features, and the flare trigger process proposed by the KB12 model. Furthermore, we realized that more flares had been triggered by the RS-type trigger than that by the OP-type. We discuss the reason why RS-type flare trigger process occurs more frequently, by evaluating the flexibility for displacement of flare trigger field from the flaring PIL.

4.1   Analysis for Internal Magnetic Reconnection

4.1.1   Overview of IRIS and Data Description

Here, we focused on the relationship between the pre-flare brightenings and the internal magnetic reconnection, and analyzed the X1.6 flare occurred on 2014 October 22, in AR 12192. While this is the same AR that was analyzed in Chapter 3, it is a different event from the one analyzed there. The X1.6 flare was the second X-class flare in the AR (cf. Table 3.2), and it was simultaneously observed by Hinode, SDO, and Interface Region Imaging Spectrograph (IRIS; De Pontieu et al. [2014]). The AR was located at S8° - 10° latitude and W20° - E5° longitude during the flare. The X1.6 flare showed simple two flare-ribbons

whereas the X1.0 flare, which was analyzed in Chapter 3, showed complicated three flare-ribbons.

Hinode/SOT observed the flare with filtergraph in the Ca II H line (3968 Å), and important features such as pre-flare brightenings and initial/enhanced flare ribbons were captured well. The cadence was one minute, the FOV was $217'' \times 108''$, and the spatial resolution was $0.2''$. Unfortunately, there was no SP vector magnetogram available within six hours before/after the flare onset. Therefore, we also used magnetograms and filtergrams obtained by SDO/HMI and AIA. We used HMI LOS/vector magnetograms in the Fe I line (6173 Å) to investigate the photospheric magnetic field structures, and AIA filtergrams in the continuum and the C IV line (1600 Å), which is sensitive to emission from the transition region and upper chromosphere (cf. Table 3.1). The cadence for LOS magnetograms, vector magnetograms, and AIA 1600 Å images were 45 *sec.*, 12 *min.*, and 24 *sec.*, respectively. We summarize the parameters for Hinode/SOT, SDO/HMI and AIA in Table 4.1.

Instrument	Hinode	SDO
	SOT/BFI	AIA [a]
FOV	$218'' \times 109''$	$2000'' \times 2000''$
Spatial Resolution	$0.2''$	$1.5''$
Cadence	1 min.	24 sec.
Wavelength	3968 Å	1600 Å
Primary Ion(s)	Ca II H	C IV + continuum
Object(s)	lower chromospheric emission	transition region and upper photospheric emission

Instrument	SDO	
	HMI (LOS magnetograms [b])	HMI (vector magnetograms [c])
FOV	$2000'' \times 2000''$	$300'' \times 200''$
Spatial Resolution	$1.0''$	
Cadence	45 sec.	12 min.
Wavelength	6173 Å	
Primary Ion(s)	Fe I	
Object(s)	lower photospheric magnetic field	

Table 4.1: Summary of parameters for Hinode/SOT and SDO/HMI, AIA

IRIS (Figure 4.1) consists a 19 cm diameter Cassegrain telescope and spectrograph. It is on the polar Sun-synchronous orbit, which is similar to that of Hinode, with $620 - 670$ km altitude, and it can continuously observe the Sun seven to eight months per year. The satellite obtains spectra in passbands from $1332 - 1358$ Å, $1389 - 1407$ Å, and $2783 - 2834$ Å, including bright spectral lines formed in the chromosphere (Mg II h 2803 Å and Mg II k 2796 Å) and transition region (C II 1334 Å and 1335 Å). Moreover, it takes slit-jaw images (SJIs) in for passbands (C II 1330 Å, Si IV 1400 Å, Mg II k 2796 Å, and Mg II wing 2830 Å). These passbands of IRIS are sensitive to emission from 5000 K to 10 MK plasmas. The maximum FOV of SJI is $175'' \times 175''$, and spectral rasters can cover $130'' \times 175''$ region.

---

[a] `aia.lev1_uv_24s` series
[b] `hmi.M_45s` series
[c] `hmi.sharp_cea_720s`: SHARP (Spaceweather HMI Active Region Patch) data series

Figure 4.1: The IRIS satellite (copyright by NASA).

IRIS successfully scanned a small magnetic structure that seems to be a flare trigger region. We used IRIS spectra and SJIs in the period of 10:00 UT (four hours before the flare onset) to 16:00 UT (two hours after the flare onset). The SJIs were obtained in the C II (1330 Å) and Mg II k (2796 Å) lines every 33 *sec.* with a FOV of $167'' \times 174''$. The spatial resolution was $0.33''$ and $0.4''$ for C II and Mg II k images, respectively. The spectra were also obtained with coarse raster scan, and we used C II (1330 Å), Si IV (1400 Å), and Mg II k (2796 Å) lines in this study. The spectra were taken in eight positions of $2''$ slit every 16.4 *sec.*, i.e. it took ~ 2 *min.* to scan 8 steps ($14'' \times 174''$ FOV). The spectral resolution was 50 mÅ and 80 mÅ, and the spatial resolution was $0.33''$ and $0.4''$ for far-ultraviolet (FUV; C II, Si IV) and near-ultraviolet (NUV; Mg II k) images, respectively. We summarize the observation parameters in Table 4.2.

Instrument	IRIS	
Data Type	Slit Jaw Images	Raster Scan
FOV	167″ × 174″	14″ × 174″
Spatial Resolution	0.33″ (FUV), 0.4″ (NUV)	
Cadence	33 sec.	16.4 sec. (for each step)
Wavelength	1330 Å, 2796 Å	1330 Å, 1400 Å, 2796 Å
Primary Ion(s)	C II, Mg II k	C II, Si IV, Mg II k
Temperature (log(T))	4.3, 4.0	4.3, 4.8, 4.0
Steps	-	8 × 2″
Spectral Resolution	-	50 mÅ (FUV), 80 mÅ (NUV)

Table 4.2: Summary of parameters for IRIS

4.1.2   Analysis Method

4.1.2.1   Analysis Method for Imaging Data
(Hinode/SOT, SDO/HMI, AIA and IRIS SJIs)

We used the same analysis methods as those explained in Chapters 2 and 3, for Hinode/SOT and SDO/HMI, AIA data. The analysis method for Hinode/SOT Ca II H line images is explained in Section 2.3, while the method for SDO/HMI filter magnetograms and AIA images is explained in Section 3.3.1. Here, we only explain the analysis method for IRIS SJIs.

We used IRIS level 2 data, in which dark-current subtraction, flat fielding, and geometrical correction are taken into account. We performed co-alignment between HMI LOS magnetograms and IRIS SJIs, via co-alignment between IRIS SJIs and AIA 1600 Å images. AIA 1600 Å images and HMI LOS magnetograms were already co-aligned using the `aia_prep` procedure, and we can align the IRIS SJIs and AIA 1600 Å using large-scale structure such as sunspots. Then, we drew the PILs of HMI LOS magnetograms onto IRIS SJIs to check the spatial

and temporal correlation between the scanning region, pre-flare brightenings, and magnetic field structures.

4.1.2.2 Analysis Method for SDO/HMI Vector Magnetogram

We also investigated the distribution of the relative shear angle χ over the AR before the flare onset, using the analysis method explained in Section 3.3.2. In Section 3.3.2, we developed the method for Hinode/SP data. Here, we applied the method to HMI vector magnetograms, i.e., the Spaceweather HMI Active Region Patch (SHARP: `hmi.sharp_cea_720s`), because there were no SP data available. The SHARP series has been already calibrated assuming the Milne-Eddington atmosphere, and 180° ambiguity in the transverse component of the image-plane vector is resolved using a minimum energy method (Metcalf [1994]; Leka et al. [2009, 2012]). In this chapter, we use the SHARP vector magnetogram taken at 13:35 UT on 2014 October 22, when it is closest in time to the last pre-flare brightening over the flare trigger region in SDO/AIA or Hinode/Ca II H images.

4.1.2.3 Analysis Method for IRIS Spectrum Data

We calculated the Doppler velocities for the Si IV line, using coarse scan data. First, we performed wavelength calibration using a photospheric line (S I, 1401 Å). We decided the central value λ_{SI_obs} of the observed wavelength for the S I line by the single Gaussian fitting. Here, we integrated the observed line profile over the region that was relatively quiet and out of the sunspot umbra. We applied the single Gaussian fitting to the integrated line profile and repeated the process for the time period of 11:00 UT to 12:00 UT on October 22. Figure 4.2 shows the integrated S I line profile at 11:00 UT on October 22 with a solid line. The broken curve represents the fitted line profile by the single Gaussian, and the vertical broken line is the fitted line center of the S I line at that time. We

averaged the fitted line center value over the time period of 11:00 UT to 12:00 UT, and obtained the observed line center λ_{SI_obs}. Then, we obtained dw by subtracting λ_{SI_obs} from λ_{SI_lab}, which is the laboratory wavelength of the S I line (1401.51 Å) and is indicated by the vertical solid line in Figure 4.2:

$$
\begin{aligned}
dw &= \lambda_{SI\_lab} - \lambda_{SI\_obs} \\
&= -0.0747 \ [\text{Å}]
\end{aligned}
$$
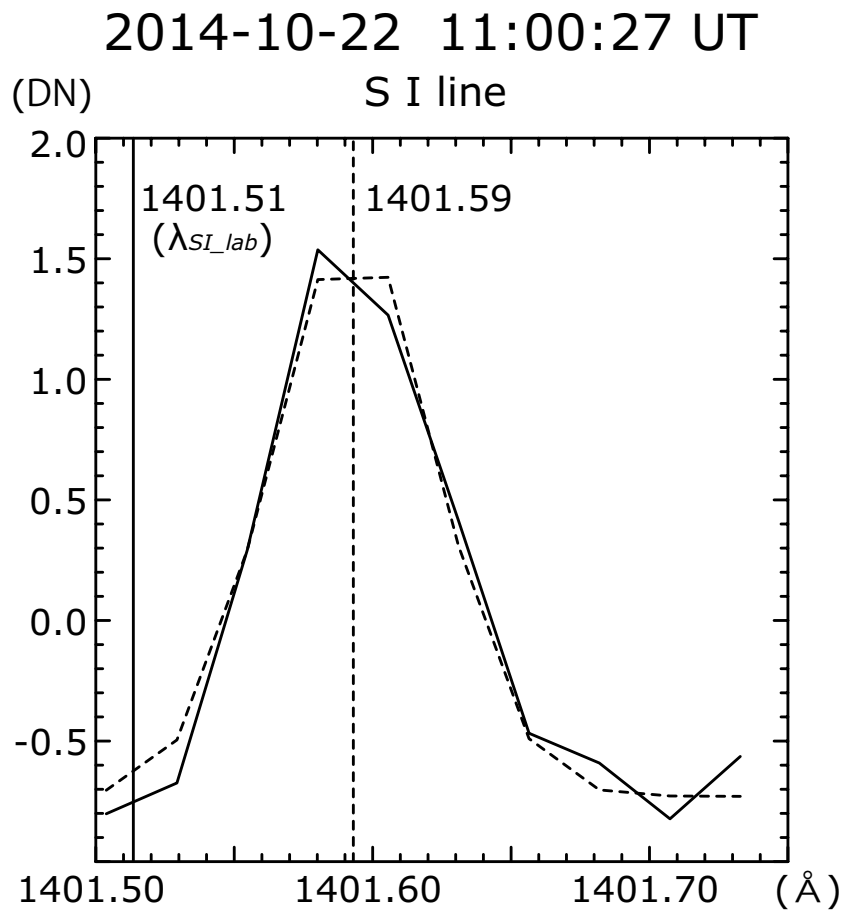
Figure 4.2: The observed line profile (solid line curve) and the Gaussian fitting profile (broken line curve) for the S I line at 11:00:27 UT on October 22. The vertical solid and broken lines indicate the S I laboratory wavelength λ_{SI_lab} and the fitted line center at that time.

Using dw, we calibrated the Si IV line as follows:

$$\lambda_{0,SiIV} = \lambda_{SiIV\_lab} - dw,$$

where λ_{SiIV_lab} is the laboratory wavelength of the Si IV line (1402.769 Å), from the CHIANTI line list[1]; Landi et al. [2012]), and $\lambda_{0,SiIV}$ is the reference wavelength of Si IV in the IRIS raster scan observation.

Next, we identified the center of observed the Si IV line λ_{SiIV_obs} using `eis_auto_fit` procedure in SSW package. Then, we calculated the Doppler velocities as follows:

$$v = \frac{\Delta\lambda_{SiIV}}{\lambda_{0,SiIV}}c,$$

where $\Delta\lambda_{SiIV} = \lambda_{0,SiIV} - \lambda_{SiIV\_obs}$ and c is the speed of light. We measured the Doppler velocities in the period of 10:00 UT to 16:00 UT on October 22, and made maps of the Doppler velocities, intensities, line width for Si IV line using `eis_get_fitdata` procedure (as can be seen in Figure 4.7).

With regard to C II and Mg II k lines, we displayed the spectrum images and line profiles, which were converted from wavelength (Å) to velocity (km/s). Basically, we applied the wavelength calibration also for C II and Mg II k lines using the S I line, as explained in the previous paragraph, and we obtained the reference wavelengths as follows.

$$\begin{aligned} \lambda_{0,CII} &= \lambda_{CII\_lab} - dw \\ \lambda_{0,MgIIk} &= \lambda_{MgIIk\_lab} - dw \end{aligned}$$

We defined $\lambda_{0,CII}$ and $\lambda_{0,MgIIk}$ as 0 km/s, and display the spectrum images (Figure 4.8) and line profiles (Figures 4.9 and 4.10) at each time for each slit and each position along the slit. Using these spectrum images and line profiles, we

---

[1]The CHIANTI is an atomic database for spectroscopic diagnostics of astrophysical plasmas developed by George Mason Univ., Univ. of Michigan, and Univ. of Cambridge (`http://www.chiantidatabase.org/chianti.html`). In this study, we chose the laboratory wavelength for the S I, Si IV, C II, and Mg II k lines from the spectral line list of the CHIANTI version 7.0.

roughly discuss the Doppler velocities for the C II and Mg II k lines.

4.1.3 Results

4.1.3.1 Identification of the Flare Trigger Region

Figure 4.3 shows the filtergrams in the Ca II H line obtained by Hinode/SOT. In the pre-flare phase, transient brightenings in the penumbral region that is indicated by the red circle were intermittently seen from 12:00 UT on October 22. The last brightening was the most brightest, as seen in panel (a), and it was seen from 13:30 UT, about 30 *min.* before the flare onset. Then the brightening disappeared, and the initial flare ribbons gradually appeared, as seen in panel (b). In particular, two initial flare ribbons in the following sunspot, which are indicated by the red arrows, appeared on both sides of the region where the last pre-flare brightening was seen. These initial flare ribbons enhanced, as seen in panel (c).

(a) pre-flare brightening (2014-10-22 13:39:49 UT)
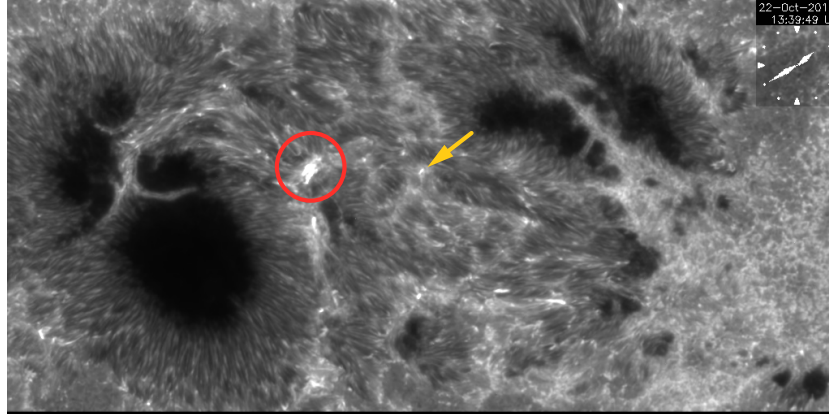
(b) initial flare ribbons (2014-10-22 14:04:49 UT)
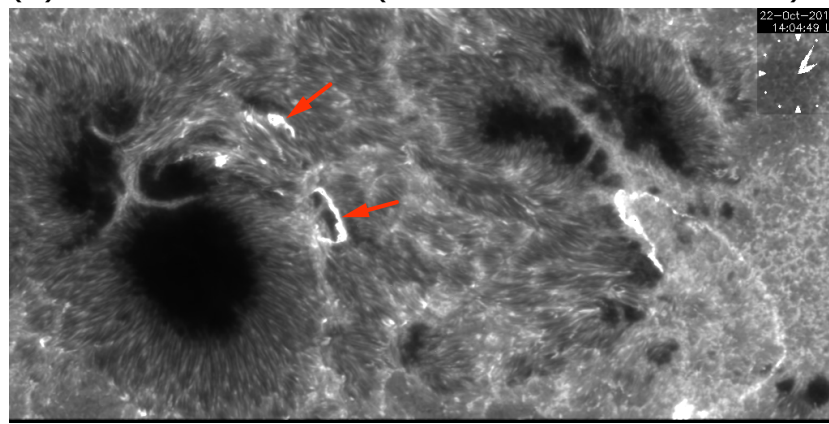
(b) flare ribbons (2014-10-22 14:10:48 UT)
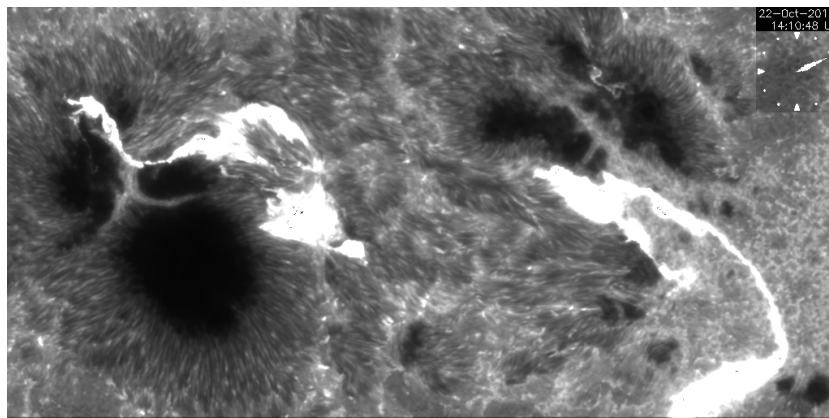
Figure 4.3: Hinode/SOT filtergrams in the Ca II H line for the X1.6 flare in AR 12192. (a) Pre-flare brightening about 30 min. before the flare onset (in the red circle) is marked by the red circle, and it corresponds to the brightening seen in TR1 in Figure 4.4 (a). The yellow arrow indicates the tiny brightening seen in TR2 in Figure 4.4 (a). (b) Initial flare ribbons. Red arrows indicate initial flare ribbons appearing on both sides of the region where the last pre-flare brightening was seen. (c) Enhanced flare ribbons about 5 min. after the onset.

Almost the same features are seen in the AIA 1600 Å images. We overlaid contours of strong brightenings in AIA 1600 Å onto HMI LOS magnetograms, as can be seen in Figure 4.4. The white/black region indicates positive/negative polarity of LOS magnetic field, and green lines and red contours outline the PIL and the strong emission in AIA 1600 Å images, respectively. In panel (a), two small magnetic structures TR1 and TR2 are marked by the yellow circles, and pre-flare brightenings were seen over the southwest PIL of both TR1 and TR2. The isolated positive region TR1, which is located in the negative sunspot (NS), emerged from October 19. The pre-flare brightenings were seen over the southwest PIL, and these started from 12:00 UT and strengthened around 13:40 UT. The brightening in TR1 corresponds to that in the region marked by the red circle in Figure 4.3 (a). In contrast, TR2 also emerged as an isolated region from October 21, but it gradually merged into the positive sunspot (PS). Very tiny brightenings were intermittently seen over the southwest PIL from 10:00 UT, and it also seen in the Hinode/SOT Ca II H line image, as indicated by the yellow arrow in Figure 4.3 (a). The brightening in TR2 continued to be bright until 3 $min.$ before the initial flare ribbons appeared, whereas the brightening in TR1 disappeared after it strengthened around 13:40 UT. Then the initial flare ribbons appeared, as indicated by the yellow arrows in Figure 4.4 (b), and these were enhanced and two flare ribbons clearly appeared, as seen in Figure 4.4 (c).
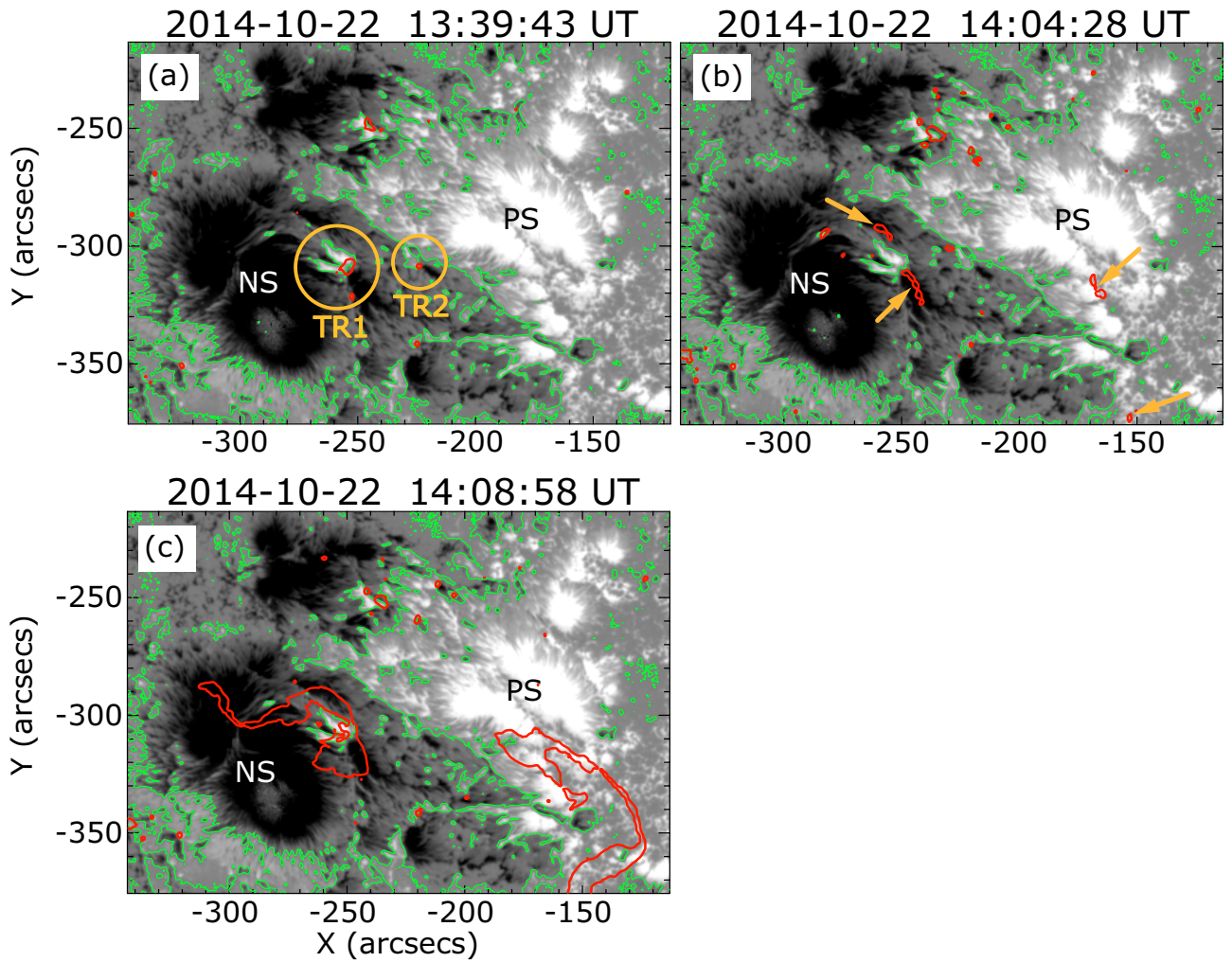
Figure 4.4: Temporal evolutions of LOS magnetic field and pre-flare brightenings seen in AIA 1600 Å. White/black indicates positive/negative polarity of the LOS magnetic field, and the intensity scale is ± 1000 G. Green lines indicate the PILs, and the red contours outline the strong emission in AIA 1600 Å images with an intensity of 2000 DN. TR1 and TR2, the region where the strong emissions were seen, is pointed out by the yellow circles in panel (a).

These features from Hinode/SOT and SDO/HMI, AIA observations suggest that both TR1 and TR2 might be a trigger of the X1.6 flare. Therefore, we quantitatively investigated the distribution of the relative shear angle χ using a HMI vector magnetogram. We defined the relative shear angle χ as the angle between the potential field vector $\boldsymbol{B}_p$ and transverse field vector $\boldsymbol{B}_t$, as explained in Section 3.3.2. Figure 4.5 shows the distribution of χ at 13:35 UT, when the strong brightening was seen over TR1. The red/blue region corresponds to positive/negative values of χ, and the black lines indicate the PILs. The values of χ along the flaring PIL (between NS and PS) and that in the southwest side of TR1 and TR2 correspond to the shear angle θ_0 of the AR and the azimuth φ_e of the small magnetic disturbance of KB12 model, respectively. χ was around $-90°$ (blue) along the flaring PIL, while it was around $90°$ (red) at the southwest side of TR1 and TR2, as indicated by the green arrows. Therefore, the distribution of the relative shear angle χ suggests that the southwest side of TR1 and TR2 satisfies the RS-type flare trigger condition of the KB12 model.

The KB12 model proposed that the shear cancellation between the global magnetic field and a small magnetic field structure can trigger a flare. Pre-flare brightening should be observed in the solar atmosphere during the shear cancellation over a small magnetic field structure. In our case, strong brightenings in the chromosphere and the transition region were observed at the southwest side of TR1 and TR2 where the magnetic shear was reversed to the shear of the global magnetic field along the flaring PIL. However, as seen in Figure 4.5, the region where χ was around $90°$ was very small in TR2, while that in TR1 was more clearly seen. In contrast, it is inferred that TR2 was located under the highly sheared magnetic arcade along the flaring PIL, whereas TR1 was seemed to be located at almost the NS-side foot point of the magnetic arcade. Therefore, it is difficult to identify whether TR1 or TR2 was the trigger region for the X1.6 flare, and both TR1 and TR2 could be a flare trigger region. In the following text, we focus on TR1 because IRIS scanned over only TR1.
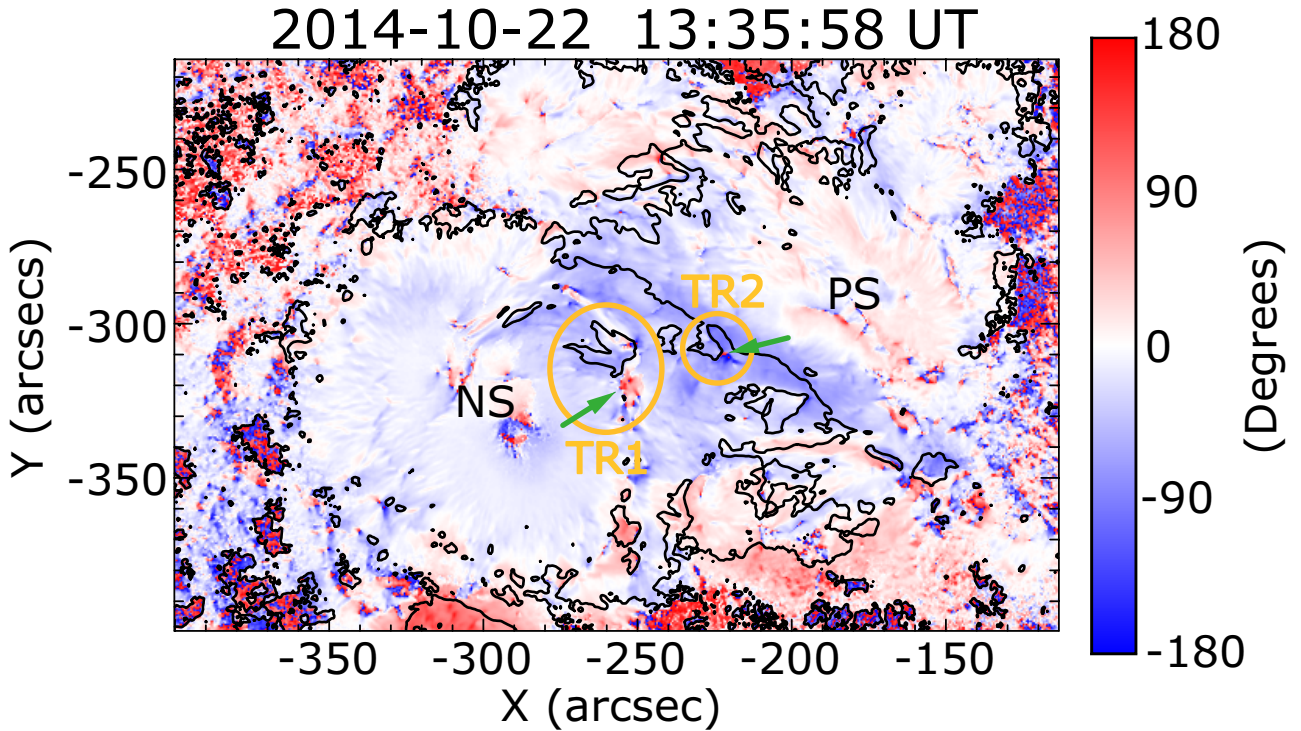
Figure 4.5: Distribution of the relative shear angle χ which is defined as the angle between the potential field vector $\boldsymbol{B}_p$ and transverse field vector $\boldsymbol{B}_t$. The black lines represent the PILs, and the red/blue region corresponds to positive/negative values of χ, i.e. the magnetic helicity. TR1 and TR2, the region where the strong emissions were seen, is pointed out by the yellow circles. The green arrows indicate the region where χ is around $90°$.

4.1.3.2 Doppler Velocities, Intensities, Line Width

Figure 4.6 shows IRIS SJIs at 13:36 UT (about 30 $min.$ before the flare onset). We overlaid the PILs of HMI LOS magnetogram, which was closest to the SJI in time, with green line. The eight slit positions for spectroscopic observation are indicated by gray and blue lines. IRIS successfully scanned over TR1, and we observed strong blue shift signals which were simultaneously seen with the last pre-flare brightening in southwest of TR1.
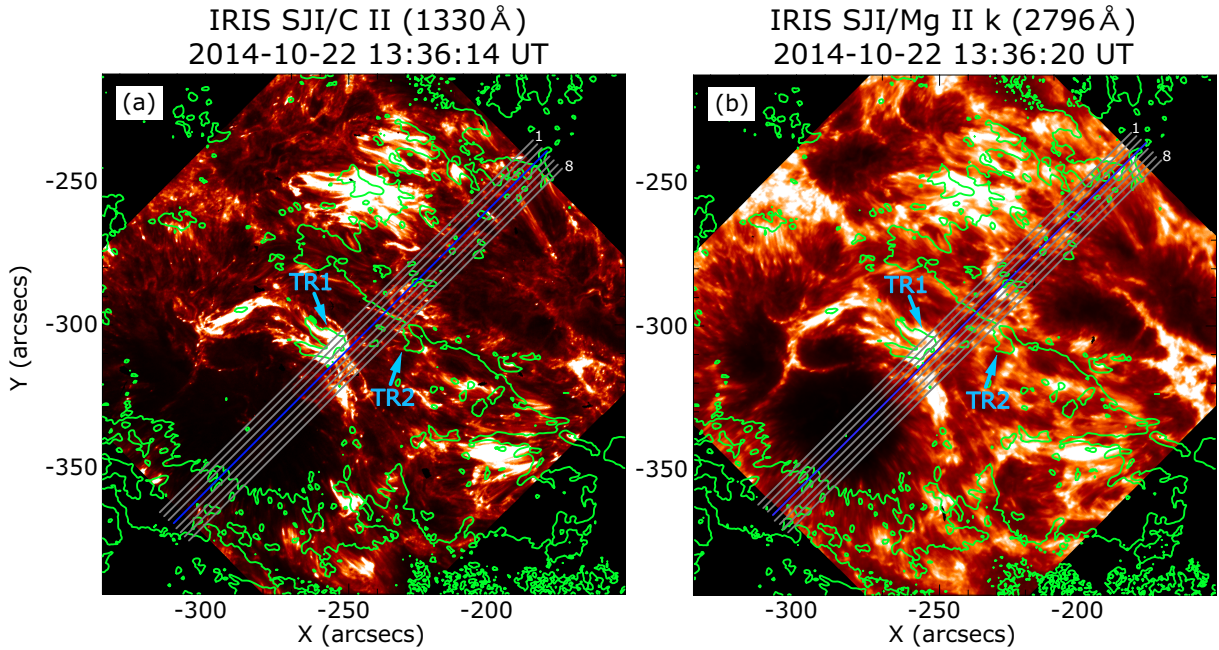
Figure 4.6: IRIS/SJIs of C II and Mg II k lines. Green lines indicate the PILs in HMI LOS magnetogram, and gray lines show the slit positions (only the fourth slit position is indicated by the blue line). The intensity scales are $0 - 250$ DN for C II and $0 - 800$ DN for Mg II k, and TR1 and TR2 are indicated by sky blue arrows in both panels (a, b).

Figure 4.7 shows the intensities, Doppler velocities, and line width for the Si IV line. The brightening in TR1, as seen in Figures 4.3 and 4.4, are marked by the yellow circle in each intensity image (left column). There were no significant red/blue shift and line broadening in TR1 before the flare, although the transient brightenings were intermittently seen in the region (Figure 4.7 (a)). However, a significant blue shift was observed just after the last pre-flare brightening appeared in the southwest side of TR1, as seen in panel (b). The location of the significant blue shift had been slightly off to southwest (toward the right in the middle image of Figure 4.7 (b)) from the pre-flare brightening. The blue shift was weakened in the brief period of 2 $min.$ (panel (c)), and further 7 $min.$ later, a red shift signal was observed in the same region (panel (d)). The averaged velocity of the blue shifted region in panel (b) and the red shifted region in panel (d) was ~ 50 km/s and ~ 25 km/s, respectively. Line broadenings were continuously observed when the last pre-flare brightening were seen.
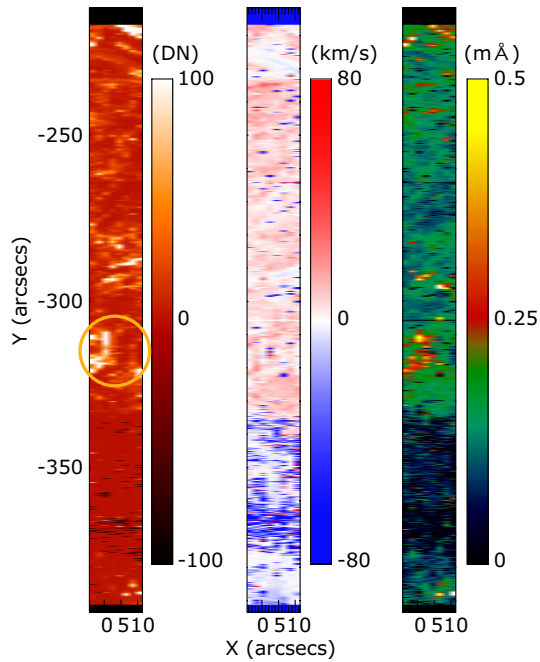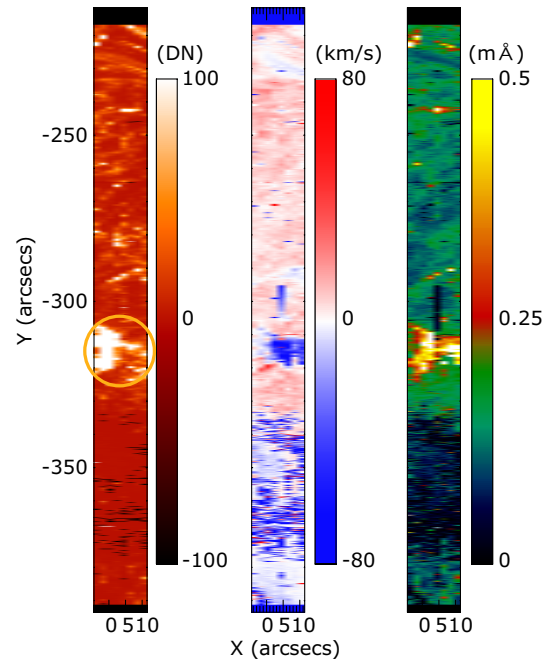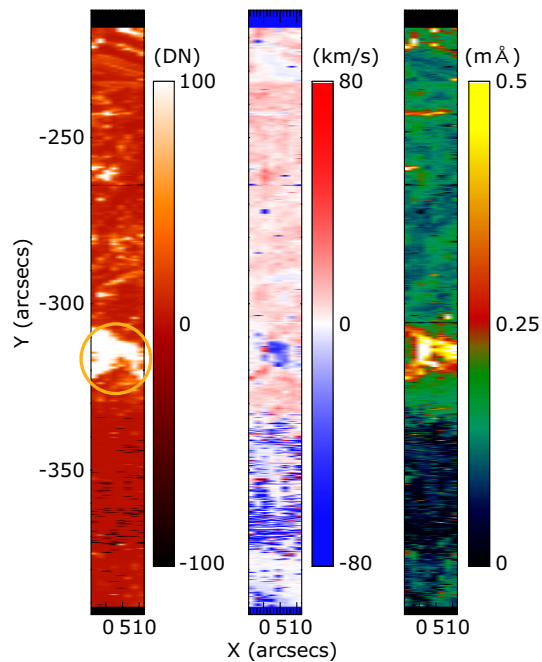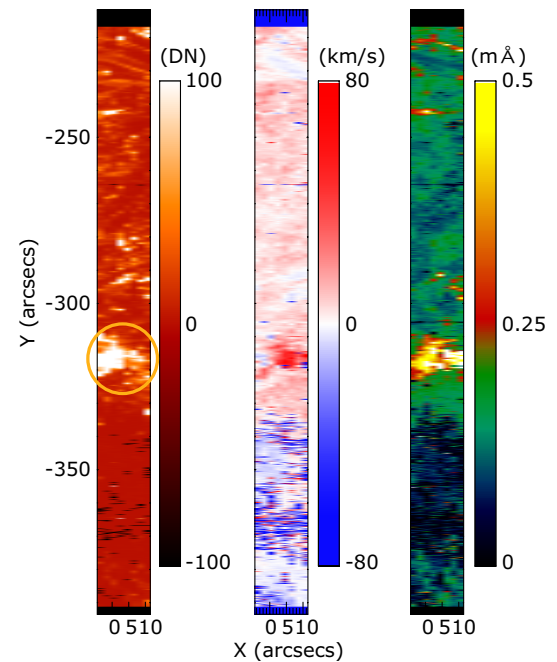
Figure 4.7: Intensities (left), Doppler velocities (middle), and line width (right) for the Si IV line over TR1 around the time of the last pre-flare brightening. The brightening in TR1, as seen in Figures 4.3 and 4.4, is marked by the yellow circle in each intensity image. (a) No significant blue shift was observed in TR1. (b, c) Blue shift was observed at the southwest side (the right side in the images) of TR1 simultaneously with the last pre-flare brightening. (d) Weak red shift was also observed in the same region just after the blue shift was observed.

Figure 4.8 displays the spectral images of the Si IV, C II, and Mg II k lines. These spectra were taken in the fourth slit (indicated by the blue line in Figure 4.6) and just over the region that satisfied the RS-type condition at 13:35:31 UT, when the last pre-flare brightening was seen. We defined the reference wavelengths $\lambda_{0,SiIV}$, $\lambda_{0,CII}$, and $\lambda_{0,MgIIk}$ as 0 km/s, as explained in Section 4.3.3. The spectra clearly show blue shifted intensities, as indicated by the yellow arrows, and the locations of the blue shifted part were consistent with those of the last pre-flare brightening in TR1 around 13:40 UT. At that time, the velocities were more than 50 km/s in each line, i.e. from the chromosphere to the transition region, and these were comparable the speed of sound in the chromosphere.
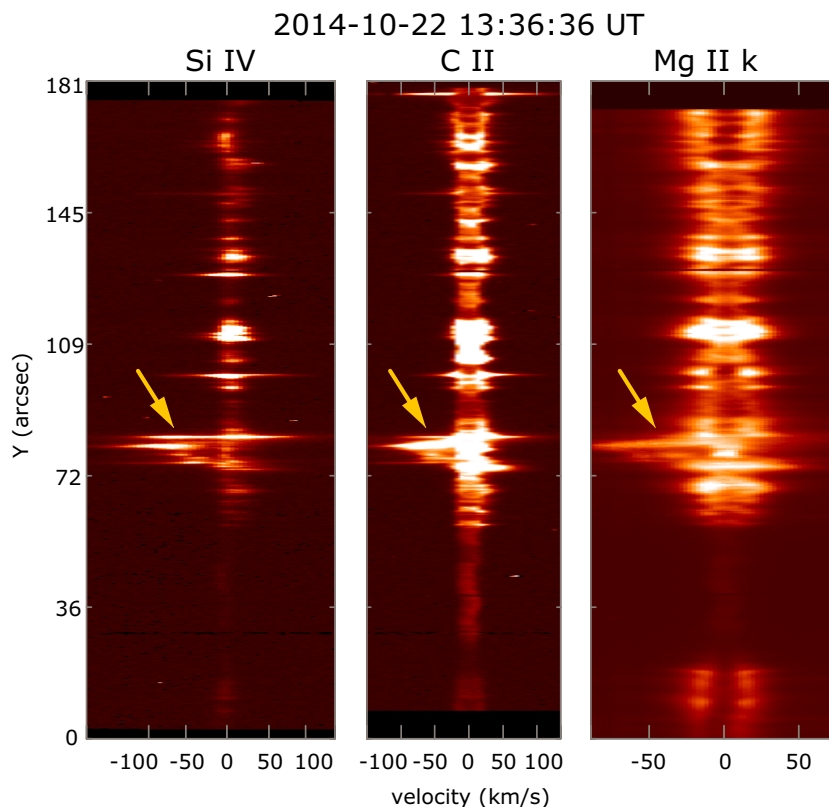
Figure 4.8: IRIS spectral images of the Si IV (left), C II (middle), and Mg II k (right) lines. The spectra were taken in the fourth slit and just over the region that satisfied the RS-type condition at 13:35:31 UT. The reference wavelength for each line $\lambda_{0,SiIV}$, $\lambda_{0,CII}$, and $\lambda_{0,MgIIk}$ was defined as 0 km/s. Blue shift parts are indicated by the yellow arrows, and the velocities were likely more than 50 km/s at that time.

Figures 4.9 and 4.10 show the blue- and red-shifted spectral line profiles taken in the fourth slit. The solid lines are the profiles at the point where the blue and red shifts were seen in TR1, at 13:36:36 UT in Figure 4.9 and at 13:45:21 UT in Figure 4.10. The horizontal axes were converted from the wavelength (Å) to the velocity (km/s). The reference wavelengths $\lambda_{0,SiIV}$, $\lambda_{0,CII}$, and $\lambda_{0,MgIIk}$ were defined as 0 km/s, as explained in Section 4.1.2.3, and the zero velocities are indicated by the vertical broken lines.

In Figure 4.9, all spectral line profiles were clearly blue shifted, as indicated by the black arrows. We can see the double intensity peak in the Si IV line profile although Si IV usually shows a single intensity peak profile. The apparent peak, which is indicated by the black arrow, was the blue-shifted part and the velocity was almost 70 km/s at that time at the point. C II and Mg II k lines usually have a double intensity peak, and the reference wavelength is the center of the absorption part in the middle of two emission part. In Figure 4.9, it was difficult to identify where is the center of the absorption part, because both C II and Mg II k lines profiles are different from the usual profiles. Even though, both C II and Mg II k line profiles are likely blue shifted.

In Figure 4.10, the significant red shift can be seen in Si IV and C II lines as indicated by the black arrows. In particular, the Si IV line profile showed clear two intensity peaks and the velocity of red-shifted part was almost 40 km/s at that time at the point. The C II line profile had been vary greatly from the usual two intensity peaks, again, but it was likely red-shifted. The Mg II k line profile was relatively similar to its usual profile, and it was likely blue-shifted at a glance. However, we are not able to exclude the possibility that the Mg II k line was slightly red-shifted, because the peak intensity of the emission line on the side of a long wavelength (i.e. on the right side in the profile in Figure 4.10) was lower than that of the emission line on the short wavelength side.
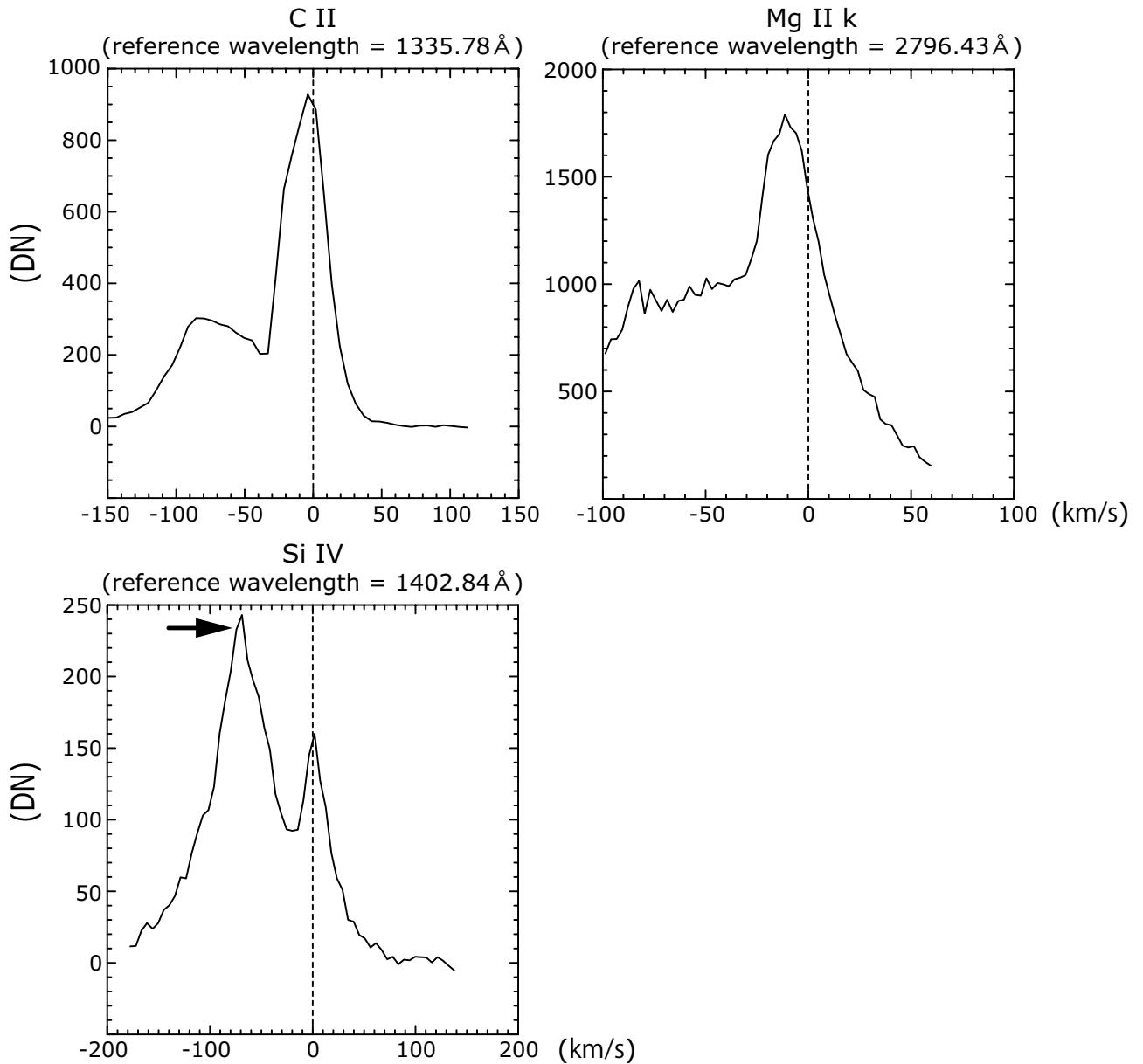
Figure 4.9: Blue-shifted profiles of the Si IV, C II, and Mg II k lines taken at 13:36:36 UT at the fourth slit (solid lines). The vertical broken lines indicate the zero velocity, which is defined as the reference wavelength of each line.
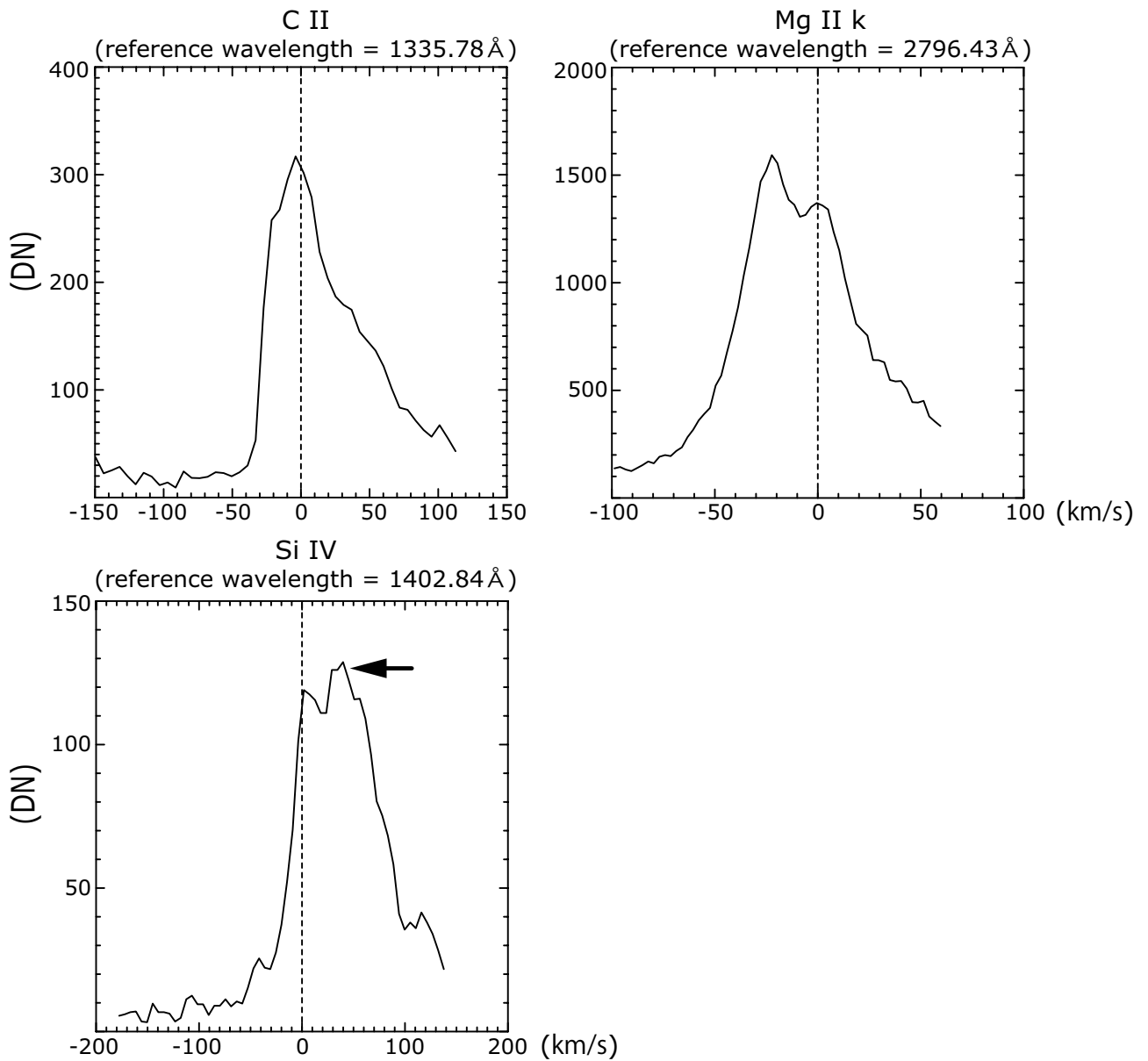
Figure 4.10: Red-shifted profiles of the Si IV, C II, and Mg II k lines taken at 13:45:21 UT at the fourth slit (solid lines). The vertical broken lines indicate the zero velocity, which is defined as the reference wavelength of each line.

4.1.4 Conceivable Scenario and Comparison with KB12 Model

We considered a flare trigger scenario of the X1.6 flare from the observed results, as shown in Section 4.1.3. We illustrate a conceivable scenario in Figure 4.11. First, internal reconnection occurred between the overlying sheared magnetic arcade (red arcade) and small-scale magnetic arcade (blue arcade) in TR1, which satisfies the geometrical condition of the RS-type flare trigger region (see panel (a)). Pre-flare brightening and significant blue shift were observed in the chromospheric lines at that time (almost 30 $min.$ before the flare onset), as seen in Figures 4.3 (a) and 4.4 (a). The internal reconnection cancelled the magnetic shear over TR1, and it made small magnetic loops, as illustrated by the sky blue arcade in panel (b). Then, the pre-existing magnetic arcade (red arcade) collapsed inward into the region where the magnetic pressure was decreased by shear cancellation. Finally, flare reconnection occurred between the red arcade, and initial flare ribbons appeared at the four foot points of the red arcade and were enhanced, as shown in Figure 4.4 (b, c).

In Section 4.1.3.2, we found that the Si IV line was significantly blue-shifted just beside (in the southwest side) of TR1, and that the averaged velocity was almost 50 km/s. C II and Mg II k lines were also likely blue-shifted at the same location and simultaneously with the Si IV line, although we were not able to decide the velocities for these two lines. It suggests that the energy input, such as internal magnetic reconnection, occurred in more lower temperature region than middle of the chromosphere, and that the jet launching chromospheric plasma was observed at the blue shift over TR1. We should consider also the possibility that internal reconnection occurred in the corona, because the pre-flare brightenings were also seen in AIA 131Å and 94Å images, which are sensitive to high temperature plasma (log (T) $\sim 5.6, 7.0$ and 6.8). However, if the internal reconnection occurred in the corona and the chromospheric evaporation was caused, we might observe redshifted emission in lower temperature lines, such as Si I

V, C II and Mg II k lines. Here, we should note that we assume the stratified atmosphere and energy input by the thermal conduction.

A picture of the internal reconnection over TR1 is inferred as shown in Figure 4.12. Our results suggest that the internal reconnection occurred at the foot point of the overlying sheared arcade (red arcade in Figure 4.11) in the negative polarity region. Reconnection jets (green arrows), which have the Alfvén velocity, were created on both sides of the reconnection region (green diagonal line part). Then, the chromospheric plasma was launched upwards, as illustrated by the blue arrow in Figure 4.12, and we observed this as the blue shift with IRIS. Then, the cool materials descended, as illustrated by the red arrow, but these might not have intruded into the dense and lower chromosphere (formation temperature region of Mg II k line) because their speed was slower than that of the blue shift. Therefore, the Mg II k line did not significantly red shift in Figure 4.10. Thus, it is inferred that the three-dimensional geometrical condition of the X1.6 was similar to that studied by Yokoyama & Shibata [1995, 1996]. When we assume a half-round loop, the loop top reaches around $2,000\ km$ because the size of the magnetic field in TR1 was almost $5''$, and the internal reconnection might occur from an altitude of a few hundred to a few thousand kilometers. Then the magnetic configuration also supports the results that the internal reconnection occurred in lower chromosphere.
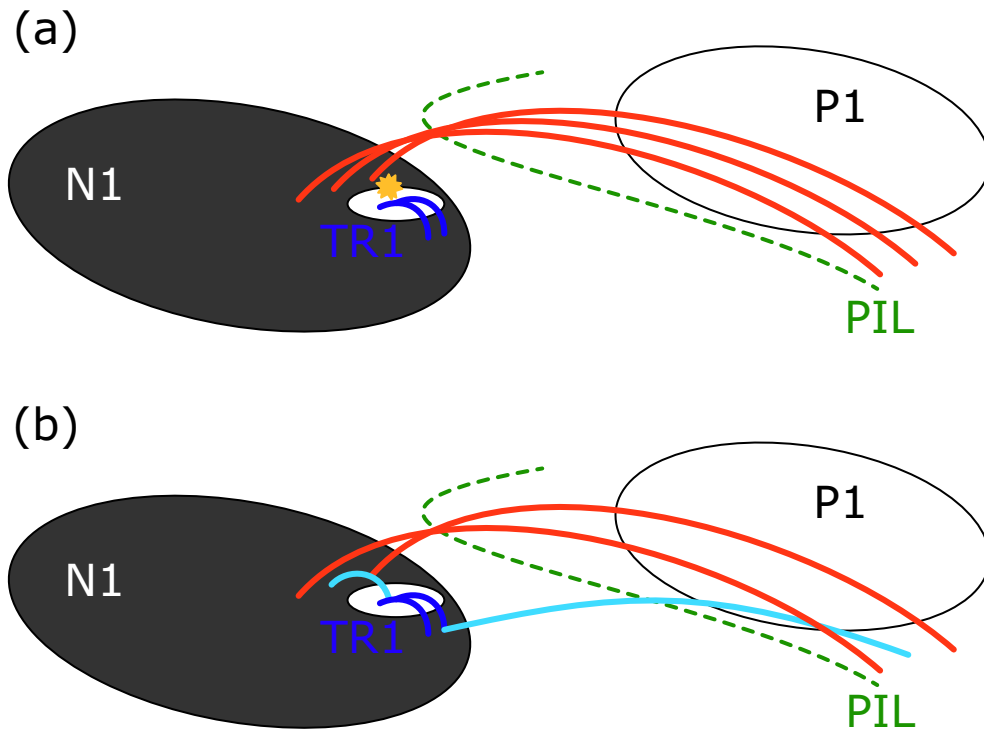
Figure 4.11: Conceivable scenario of the X1.6 flare in AR 12192. (a) Shear cancellation (internal reconnection) occurred between TR1 and the overlying sheared magnetic field. (b) Overlying arcade collapse to the region where the magnetic pressure decreased by the shear cancellation, and flare reconnection occurred.
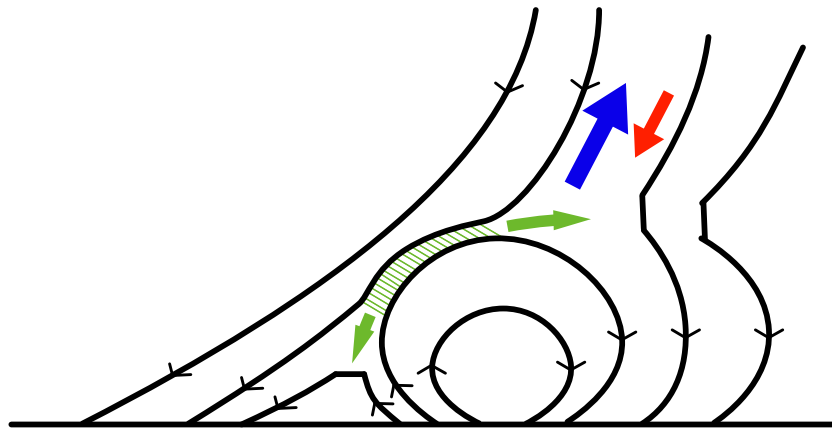
Figure 4.12: Image of internal reconnection in TR1 (cf. Yokoyama & Shibata [1995, 1996]). Internal reconnection (shear cancellation) occurred in the green diagonal line part. Green arrows indicate the reconnection jet (comparable to the Alfvén velocity). The observed plasma up flow (blue shift) and down flow (red shift) are illustrated by the blue and red arrows, respectively.

Therefore, we confirmed that pre-flare brightenings are caused by the internal magnetic reconnection between the pre-existing sheared magnetic field and a small-scale flare trigger field. It indicates that using pre-flare brightenings as a marker of the flare trigger field is meaningful. According to the KB12 model, the possible altitude of the internal reconnection is different between the OP- and RS-types. In case of the RS-type flare trigger process, internal reconnection i.e. magnetic shear cancellation between the flare trigger field and the pre-existing magnetic field can occur anywhere from the photosphere to the corona. In contrast, in the OP-type flare trigger process, internal reconnection should occur in the lower atmosphere because two pre-existing sheared magnetic arcades should reconnect via the OP-type flare trigger field to form long twisted flux ropes. Therefore, the altitude of the internal reconnection is more critical for flare triggering in the OP-type case, and we still need to confirm it using high spatial and temporal resolution spectroscopic observation data, such as IRIS.

4.2 Possibility of an Additional Parameter

4.2.1 Posing a Problem

Next, we propose the possibility of an additional parameter that should be considered as flare trigger conditions. We confirmed that the four flare events satisfies the specific combination of the two parameters θ_0 and φ_e, in Chapter 2. Figure 4.13 displays a time series of Stokes-V/I images and pre-flare brightenings in AR 10930 over the four hours leading to the X3.4 flare, which were analyzed as Event 1 in Chapter 2. Clearly, a magnetic structure topologically consistent with the OP-type flare trigger region had already appeared at 20:00 UT on December 12 (see panel (a)). At 00:24 UT December 13, the strong brightening was precisely centered on the OP-type magnetic field (indicated by B1 in panel (c)). The geometric structures of the magnetic field and pre-flare brightening fitted the flare trigger scenario of an OP-type magnetic field. However, the brightening could not be followed by flaring at this stage because it was immediately diminished (panel (d)) and followed by another transient brightening (panel (e)). The other brightening occurred at 02:06 UT (B2 in panel (g)), where it persisted and evolved to the X3.4 flare (Event 1). These results imply that the magnetic field must satisfy not only the geometrical conditions but also some additional property in order to trigger flares.
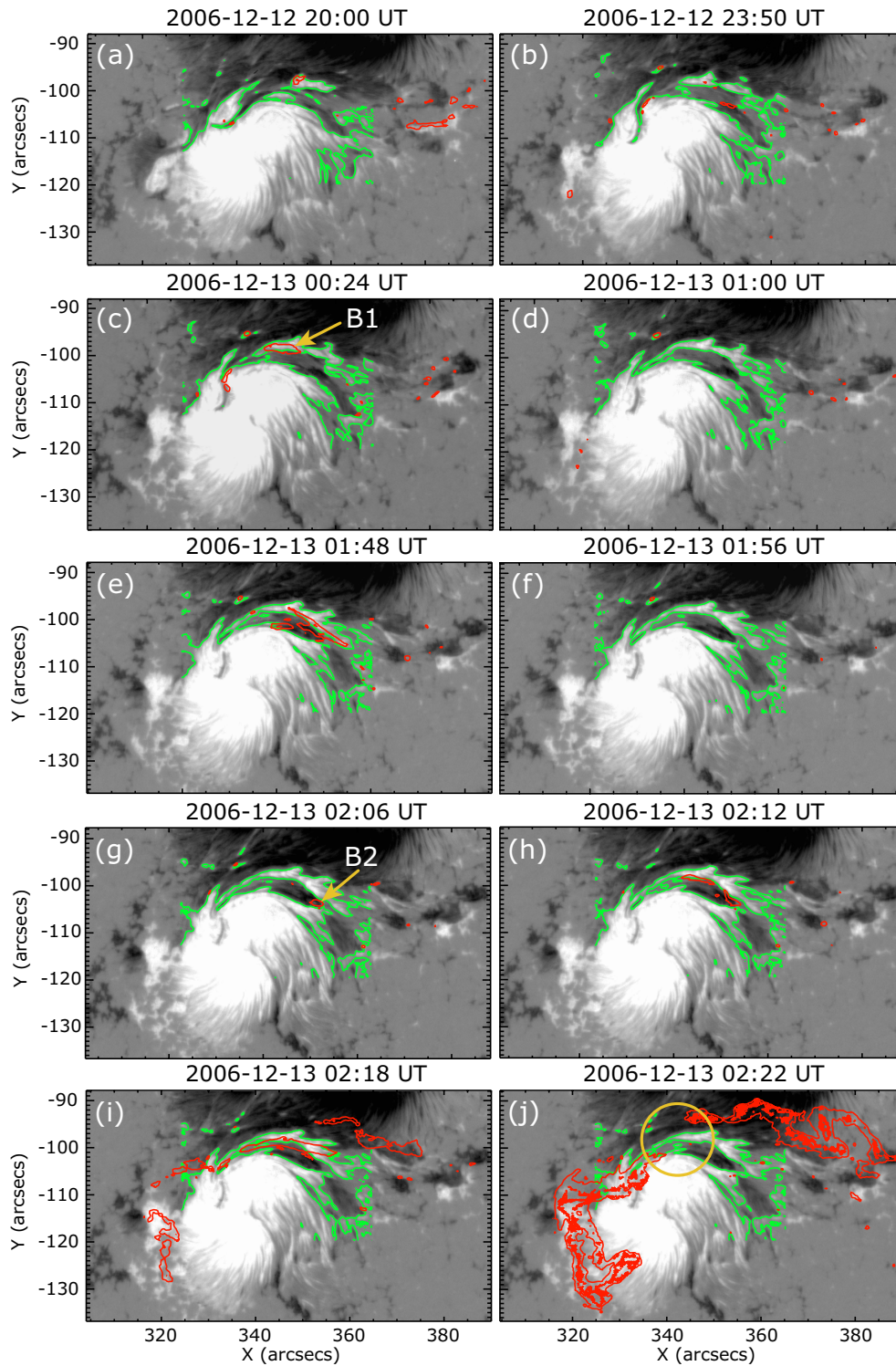
Figure 4.13: Temporal variations in Stokes-V/I images preceding the X3.4 flare (Event 1) on 2006 December 13. The images are formatted as described for Figure 2.4, and the yellow circle in panel (j) indicates the flare trigger region. The transient brightening B1, located at the center of the flare trigger region in panel (c), did not by itself induce a flare. In contrast, the brightening B2, located offset from the flare trigger region, ultimately led to the flare onset.

Here, let us propose that the "total magnetic flux" contained in the flare trigger field of either topology (OP or RS) contributes to the critical conditions for flare triggering. This hypothesis is feasible because very small magnetic islands could not inject sufficient magnetic flux into the flux tube to destabilize it for flare onset. To examine this hypothesis, we investigated the temporal evolution of magnetic flux in the flare trigger region for the X3.4 OP-type flare and the M6.6 RS-type flare (Event 3 in Chapter 2).

4.2.2 Analysis Method and Results

We converted the Stokes-V/I signal to a magnetic field in Gaussian units using the LOS magnetogram scanned at 04:00 - 05:36 UT on 2006 December 13 by Hinode/SOT SP and the filtergram at 04:44 UT December 13. Figure 4.14 (a) shows the scatter plots for them with the linear fitting line (red line). For AR 10930 data obtained in 2006, we converted the Stokes-V/I signals because FG stokes Stokes-I and V signals independently. In contrast, for AR 11158 data obtained in 2011, the Stokes-V/I signals were calculated and it converted to magnetic field strength on board of Hinode. However, the magnetic field strength is not accurate because FG measured the Stokes-V/I signals at only one wavelength point sifted from Na I D1 line by 140 mÅ. Therefore, we needed to convert also the imitation magnetic field strength for AR 11158 to accurate magnetic field in Gaussian units using the LOS magnetogram scanned at 16:00 - 16:32 UT and the filtergram obtained at 16:15 UT on 2011 February 13. The correlation map between the LOS magnetic field by SP and the imitation magnetic field strength by filtergram is shown with the linear fitting line in Figure 4.14 (b). We converted the FG Stokes-V/I signal to magnetic intensity B (G) using the regression line in Figure 4.14, and calculated the magnetic flux $F = \int f B dS$ (Mx) plotted in Figure 4.15, where the integration was taken over the positive magnetic flux

region shown by the yellow rectangle in Figure 4.15 (a). Here, f is the filling factor of the magnetic field.

(a) NOAA AR 10930

(b) NOAA AR 11158
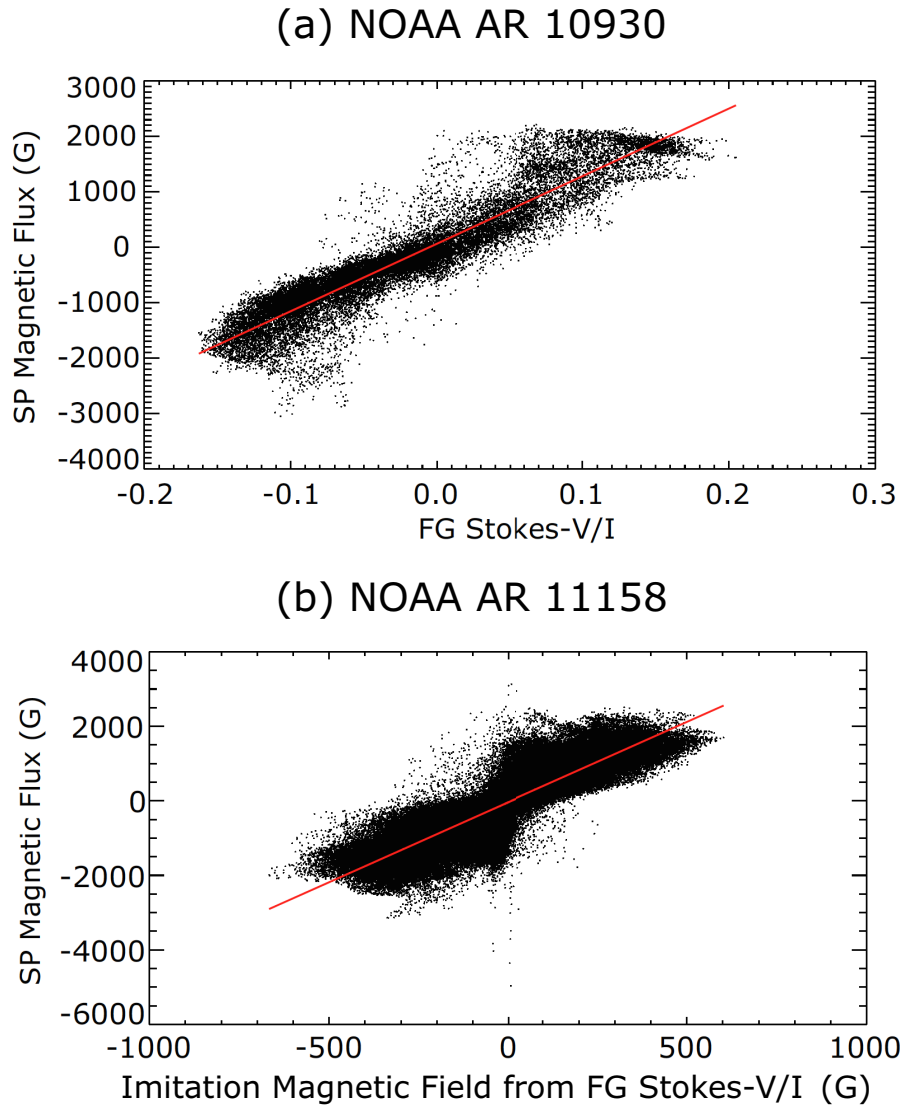
Figure 4.14: Intensity of LOS magnetic field by Hinode/SP plotted against the Stokes-V/I signal by Hinode/FG for (a) X3.4 flare on AR 10930 and (b) M6.6 flare on AR 11158. The Stokes-V/I signals were measured at a wavelength point sifted from Fe I line by -120 mÅ/from Na I D1 line by 140 mÅ for AR 10930/AR 11158, respectively. The intensity of the Stokes-V/I signal was calibrated according to Ichimoto et al. [2008]. The red lines were obtained by linear fitting. In (a), the LOS magnetogram scanned at 04:30 - 05:36 UT and the filtergram at 04:12 UT 2006 December 13 were used. In (b), the LOS magnetogram scanned at 16:00 - 16:32 UT and the filtergram at 16:15 UT 2011 February 13 were used. The horizontal axis indicates the imitation magnetic field, which was calculated from the Stokes-V/I signals.

From this conversion, we derived the LOS component of the magnetic field with a two-minute cadence and integrated it over the regions of positive magnetic polarity in the magnetic island (yellow rectangle in Figure 4.15 (a)). The magnetic flux is plotted with the green line in Figure 4.15 (b). The vertical solid line indicates the onset of the X3.4 flare (02:14 UT December 13), while the vertical dashed line represents the time of the precedent brightening (B1 in Figure 4.13 (c), 00:24 UT December 13). In this figure, the magnetic flux in the positive regions of the magnetic island continuously increased from three hours prior to the flare onset. This confirms our hypothesis that magnetic flux must be built to a critical level before a flare can be triggered. Figure 4.15 (b) also plots the light curve of total Ca-line emission over the yellow rectangles shown in Figure 4.13 (a). Here, it is noteworthy that all three pre-flare brightening events (at 00:20, 01:40, and 02:05 UT) followed a rapid magnetic flux increase denoted by the yellow arrows. This result may be explained by assuming that the rapid emerging of magnetic fluxes favor internal reconnection with the overlying magnetic arcade. Therefore, the flare trigger field must satisfy both geometrical and quantitative magnetic flux conditions. In addition, to enable flare triggering, the flare trigger field should rapidly expand to drive the internal reconnection.
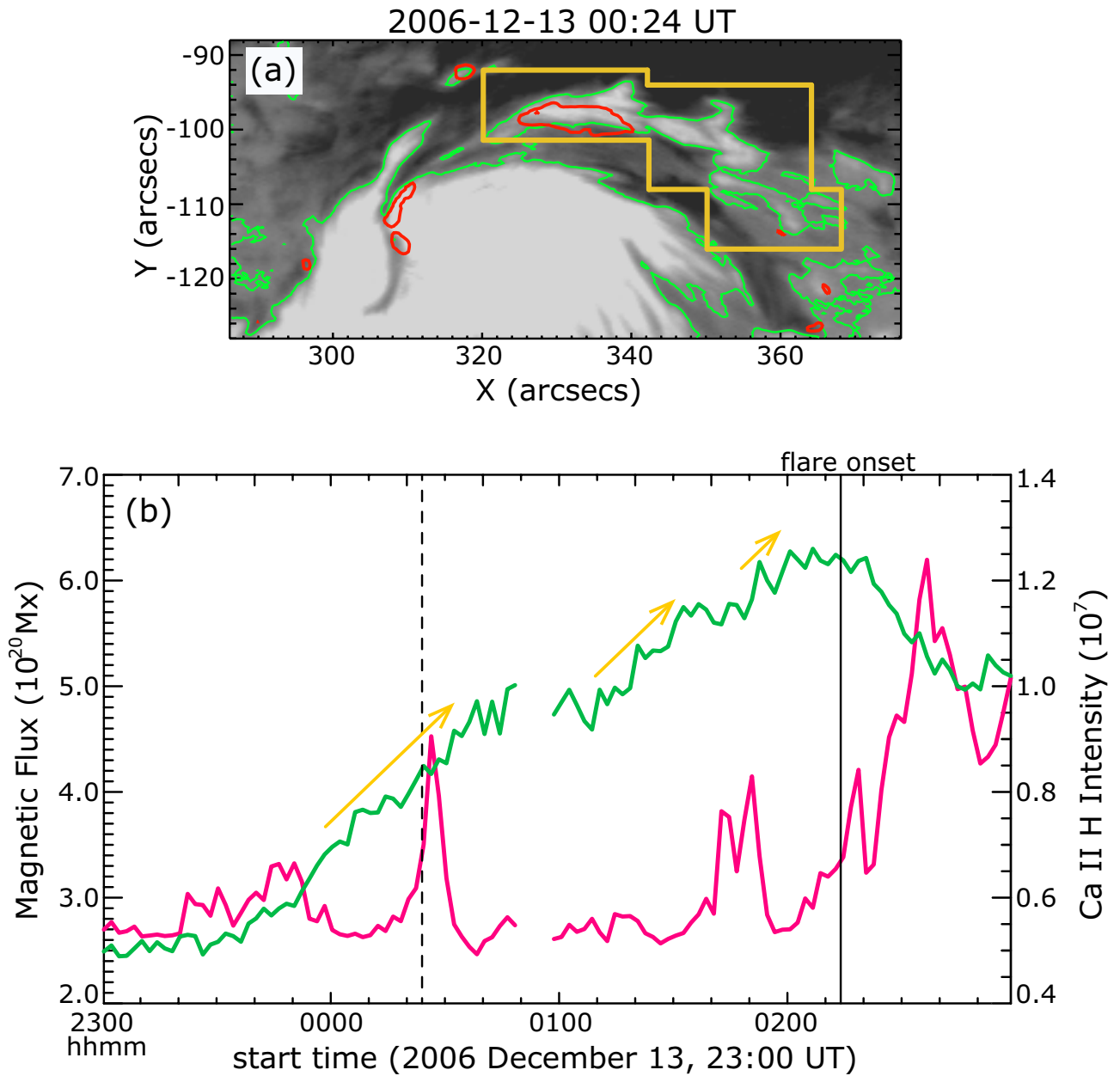
Figure 4.15: (a) LOS magnetic field in the flare trigger region of Event 1. The Stokes-V/I signals were converted to magnetic intensity, and the intensity scale is ± 1000 G. The yellow rectangle indicates the region where magnetic flux and Ca-line intensity are integrated. The green lines represent the PILs, and the red contours indicate strong brightenings in the Ca-line. (b) Time evolution of positive magnetic flux and Ca-line intensity integrated in the yellow rectangle in panel (a). The vertical solid line marks the onset time of the flare, 02:14 UT 2006 December 13, and the dashed line corresponds to the time of panel (a). The green and pink lines plot positive magnetic flux and Ca-line intensity, respectively.

Similar properties apply to the M6.6 flare in AR 11158 (Event 3). Figure 4.16 is a time series of Stokes-V/I images overlaid by Ca-line emissions in Event 3. Here, we observed that the growth of the wedge-like structure on the PIL (within the yellow rectangle) was followed by the M6.6 flare (Figure 4.16 (f)). To quantify the growth of the flare trigger field, we calculated the magnetic flux over the regions of positive polarity within the yellow rectangles of Figure 4.16.

We plot the magnetic flux and Ca-line intensity from six to zero hours preceding the onset of the M6.6 flare onset in Figure 4.17. Although SOT/FG data between 13:15 and 15:00 UT were missing, the magnetic flux in the flare trigger field clearly increased by 20 - 30% between 13:15 UT and 15:20 UT, as has been investigated in detail by Toriumi et al. [2013]. They found that the flux increases were associated with a small, positive island traveling from the north into a wedge-like region. The Ca-line emission on the wedge-like structure was extended northward and southward along the island displacement (indicated by the arrow in Figure 4.16 (b)). The supply of positive flux into the wedge-like region almost ceased before 16:30 UT, and the Ca-line emission in this region also weakened at that time. The Ca-line emission reappeared after 16:35 UT. Although the bright region on the PIL (indicated by the arrow in Figure 4.16 (d)) weakly expanded until 17:05 UT, it diminished thereafter (see Figure 4.16 (e)) followed by a sudden flare (Figure 4.16 (f)).
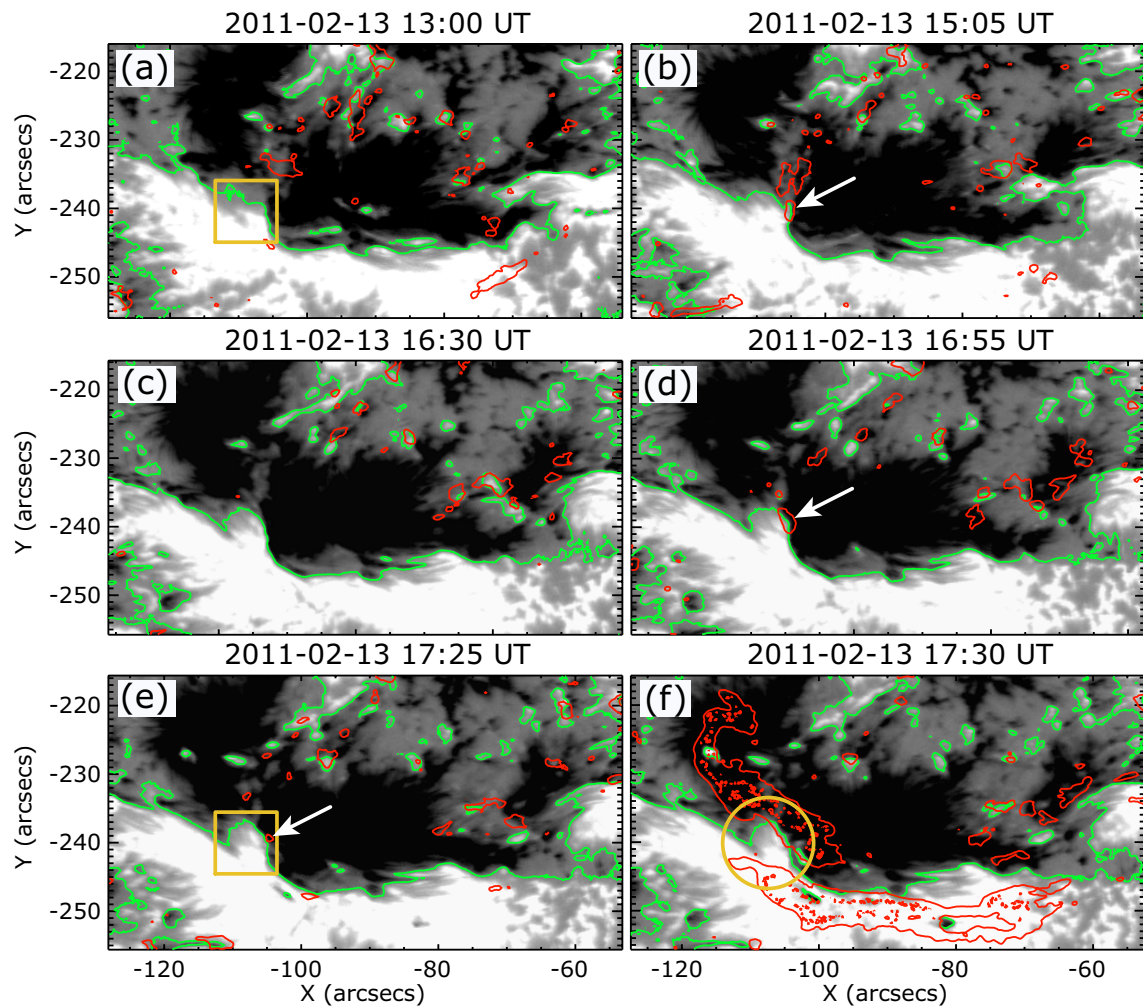
Figure 4.16: Temporal variations in Stokes-V/I images preceding the M6.6 flare (Event 3) on 2011 February 13. The images are formatted as described for Figure 2.4, and the yellow circle in panel (f) indicates the flare trigger region. The yellow squares in panels (a, e) identify the region of positive magnetic flux and Ca-line intensity (plotted in Figure 4.17).
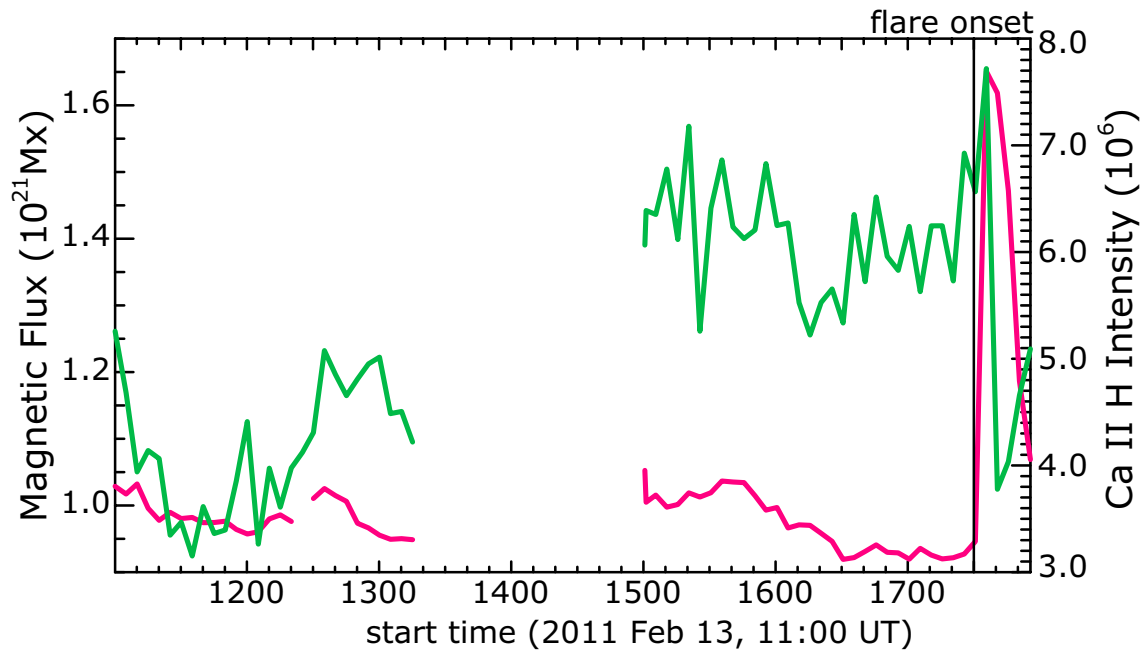
Figure 4.17: Temporal evolution of positive magnetic flux and Ca-line intensity prior to the M6.6 flare onset. The vertical solid line marks the onset time of the flare, 16:30 UT 2011 February 13. The image is formatted as described for Figure 4.15 (b). The region of positive magnetic flux and Ca-line intensity is delineated by the yellow squares in Figure 4.16 (a, e).

4.2.3   Interpretation and Consideration

We should note that, in Event 3, the magnetic flux in the flare trigger field peaked two hours prior to the M6.6 flare onset (at 15:20 UT in Figure 4.17). By contrast, in Event 1, the flux in the flare trigger field continuously increased and peaked immediately before the X3.4 flare onset (see Figure 4.15). This difference between Events 1 and 3 is attributable to the differences in the flare trigger processes, which are initiated by OP and RS magnetic field types, respectively. The former directly destabilizes the twisted flux by internal reconnection, whereas the latter indirectly forms a twisted flux by magnetic shear cancellation, and results in subsequent internal collapse of the magnetic arcade. Because reconnection between the normal and RS fields cannot instantaneously cancel the magnetic shear, flaring in RS fields occurs somewhat later than the evolution of magnetic flux to critical conditions. In contrast, because the larger flux in OP fields can

directly generate a high twisted flux, which may become destabilized by the torus mode instability, the flare immediately results once the flare trigger field exceeds criticality.

Moreover, the critical magnetic flux in the flare trigger field differs among events, as we summarized in Table 2.3. The flare trigger fields in Event 2 (X1.5 flare on 2006 December 14 in AR 10930) and Event 4 (X2.2 flare on 2011 February 15 in AR 11158) are much smaller than those in Events 1 and 3, although both pairs of events occurring in the same ARs were triggered by the same type of magnetic field (OP in Events 1 and 2, and RS in Events 3 and 4). The critical perturbation amplitude required to trigger the instability depends on the proximity of the system to the unstable state. If the stability of the system is precarious, even small perturbations can induce instability, whereas tenaciously stable systems will not destabilize unless the perturbations are large. Therefore, the magnetic fields in the pre-flare phases of Events 2 and 4 were likely to be less stable than those of Events 1 and 3. For instance, the X-ray and EUV observations[2] revealed that a highly sheared loop was formed in the pre-flare stage of Event 2, whereas it was not seen in Event 1 (Su et al. [2007]). This result suggests that the sheared loop was long enough to generate instability developed prior to the flare in Event 2.

If the internal reconnection is not activated magnetic connectivity, which is determined by the bipolarity of the originally emerging flux, and a long sheared loop cannot fully develop. Eventually, a long sheared loop may be formed by the internal reconnection on the PIL. Therefore, the critical size of the flare trigger field likely changes during the evolution of the ARs. The size relationship between the flare trigger fields of Events 1 and 2 and those of Events 3 and 4 is consistent with this notion. However, an extended statistical study is required to elucidate the factors underlying the critical fluxes of the flare trigger fields.

---

[2]These were collected by Hinode/X-ray Telescope (XRT) and Transition Region and Coronal Explorer (TRACE), respectively.

4.3 Statistical Analysis

4.3.1 Statistical Classification

We next consider whether the KB12 model can explain the trigger process of various flare events. We used SDO data selected by the following criteria, which are almost the same to those used in Chapter 2, and we classified the events into independent six types including OP- and RS-types.

1. The GOES class was larger than M5.0.

2. The event was observed by SDO/HMI and AIA 1600 Å from 2010 February 11 to 2014 February 28, and both pre-flare and main flare phases were covered by SDO observation.

3. The flaring site was located within $\pm$ 750″ from the solar disk center.

Then, we selected 32 events (11 X-class and 21 M-class flares), and the aligned PIL and contours of strong brightenings in AIA 1600 Å onto HMI LOS magnetograms by the same method described in Sections 2.3.1 and 3.3.1.

We classified the 32 events in the method summarized in Figure 4.18. First, Type-D, which did not show clear sheared two-ribbon structures in the initial flare phase, branched. We evaluated the events that were not classified into Type-D, to determine whether the pre-flare brightenings were seen on the PIL at the center of sheared two-ribbon flares before the flare onset. Here, we defined pre-flare brightenings as transient brightenings in AIA 1600 Å, which were seen in at least two frames (i.e. at least over a period of $\sim$ 1.5 $min.$) from one hour before the flare onset, because pre-flare brightenings were seen within one hour before

the flare onset and continued at least few minutes in Chapter 2 as summarized in Table 2.3. If there were no pre-flare brightenings before the flare, it branched to a Type-C event. Finally, we determined the flare trigger region and measured the shear angle θ_0 of the global magnetic arcade and the azimuthal angle φ_e of the flare trigger region using the method described in Section 2.3.2. As a result of measurement of θ_0 and φ_e, we classified the events into the OP- or RS-types, or the other Type-A, which occurred under the "no-flare" condition, as indicated by the open squares in the Flare Phase Diagram (Figure 1.8). We should note that we considered Type-B for the case in which there was no HMI SHARP data series (vector magnetograms) necessary for measuring the angles θ_0 and φ_e.
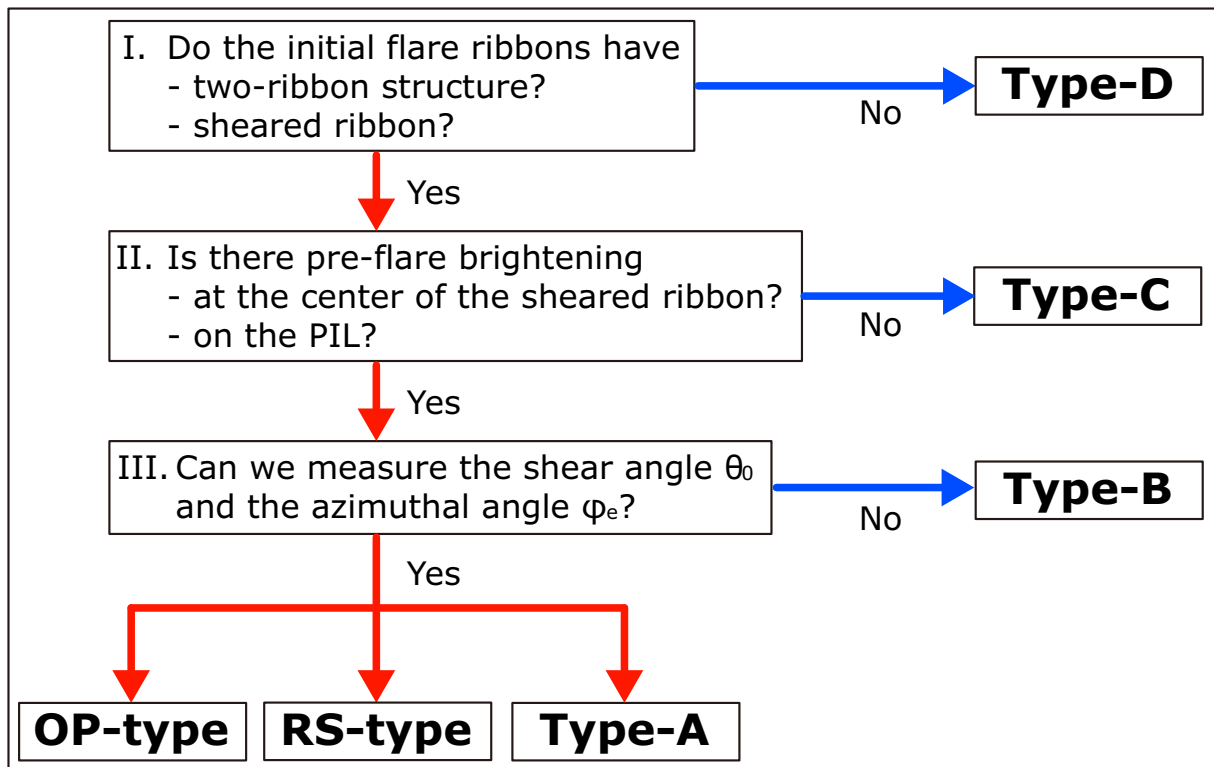
Figure 4.18: Classification chart of SDO events.

The selected X-class and M-class flares are listed in Tables 4.3 and 4.4, respectively, with the classification result. The X2.2 flare on 2011 February 15 (Event 4 in Chapter 2) and M6.6 flare on 2011 February 13 (Event 3 in Chapter 2) are also listed as event Nos. 1 and 12, respectively. Table 4.5 summarizes the classification. First, no flare event occurred under the condition of the combinations of the angles θ_0 and φ_e which indicates "no-flare" in the KB12 model (i.e. with the condition indicated by the "□" symbol in Figure 1.8). It means that there was no event clearly inconsistent with the flare trigger condition proposed by the KB12 model. Second, the selected events did not include the OP-type and Type-A, and six events (19% of the entire events) were classified into the RS-type. Three events (9% of the all) were Type-B, i.e. we could not measure the angles θ_0 and φ_e because of the lack of SHARP data, but the qualitative features of these three events were consistent with the RS-type. Finally, it is the most noteworthy that 23 events (72%) were classified into Types-C or D. In other words, more than 70% of the selected events did not show the theoretically predicted features such as sheared two-ribbon flares and pre-flare brightenings. Therefore, it is important to investigate the consistency between the KB12 model and the events classified into Types-C and D, in order to evaluate the consistency between the model and the observations.

No.	Date	Onset (UT)	Class [1]	AR [2]	Type
1	2011 February 15	01:44	X2.2	11158	RS ($\theta_0 \sim 86°, \varphi_e \sim 331°$)
2	2011 March 9	23:13	X1.5	11166	D
3	2011 September 6	22:12	X2.1	11283	C
4	2011 September 7	22:32	X1.8		D
5	2012 March 5	02:30	X1.1		C
6	2012 March 7	00:02	X5.4	11429	RS ($\theta_0 \sim 108°, \varphi_e \sim 313°$)
7	2012 March 7	01:05	X1.3		RS ($\theta_0 \sim 68°, \varphi_e \sim 295°$)
8	2012 July 12	15:37	X1.4	11520	C
9	2013 November 5	22:07	X3.3	11890	D
10	2013 November 8	04:20	X1.1		C
11	2014 January 7	18:04	X1.2	11944	C

Table 4.3: Event list and classification results for X-class flares

No.	Date	Onset (UT)	Class [1]	AR [2]	Type
12	2011 February 13	17:28	M6.6	11158	RS ($\theta_0 \sim 88°, \varphi_e \sim 344°$)
13	2011 August 3	13:17	M6.0	11261	B (RS-like)
14	2011 August 4	03:41	M9.3		D
15	2011 September 6	01:35	M5.3	11283	C
16	2011 September 8	15:32	M6.7		D
17	2012 January 23	03:38	M8.7	11402	B (RS-like)
18	2012 March 9	03:22	M6.3	11429	RS ($\theta_0 \sim 74°, \varphi_e \sim 333°$)
19	2012 March10	17:15	M8.4		RS ($\theta_0 \sim 98°, \varphi_e \sim 312°$)
20	2012 May 10	04:11	M5.7	11476	D
21	2012 July 2	10:43	M5.6	11515	D
22	2012 July 4	09:47	M5.3		C
23	2012 July 5	11:39	M6.1		D
24	2012 November 13	01:58	M6.0	11613	D
25	2013 April 11	06:55	M6.5	11719	C
26	2013 October 24	00:21	M9.3	11877	D
27	2013 November 1	19:46	M6.3	11884	C
28	2013 November 3	05:16	M5.0		C
29	2013 December 31	21:45	M6.4	11936	C
30	2014 January 1	18:40	M9.9		D
31	2014 January 4	10:07	M7.2	11944	C
32	2014 February 4	03:57	M5.2	11967	B (RS-like)

Table 4.4: Event list and classification results for M-class flares

Type	Number of events	Ratio
OP	0	0 %
RS	6	19 %
A	0	0 %
B	3	9 %
C	12	38 %
D	11	34 %

Table 4.5: Summary of the statistical classification

---

[1]These are defined from GOES X-ray observation.
[2]NOAA AR number

4.3.2 Consideration of Type-D Case

Many of the Type-D events showed very complicated flare ribbons. However, some of them could be understood by investigating the relevance to filament eruption or other flare events in the same region. Here, we show an example of the M5.6 flare (No. 21 listed in Table 4.4) occurred on 2012 July 2 in AR 11515. Figure 4.19 shows the temporal evolution of the LOS magnetograms and brightenings in AIA 1600 Å. The M5.6 flare occurred in the weak negative polarity region between the leading sunspot (LS) and the satellite spot (SS), not the central PIL of the AR. We classified the event into Type-D because the initial flare ribbons, which are seen in Figure 4.19 (e), were complicated and we could not clearly distinguish between positive and negative ribbons. Moreover, the M5.6 flare followed filament eruption and the other C2.9 flare in the same region (see Figure 4.20). Louis et al. [2014] studied about the relevance between the filament eruption followed by the C2.9 and the M5.6 flares and the sunspot evolution such as flux emergence, cancellation, and sunspot rotation, using SDO images and Hα (6562.8 Å) images observed by the chromospheric Telescope (ChroTel; Kentischer et al. [2008]) at the Observatorio del Teide, Tenerife, Spain. Their conclusion is that the splitting motion of the LS triggered the filament eruption, but we interpreted that the M5.6 flare was triggered by the RS-like small magnetic structure, which was located at the foot point of the filament.

According to Louis et al. [2014], there was a filament was rooted in the rear part of the LS and weak negative region, as illustrated in Figure 4.19 (a, b) by blue arcs. We found a tiny brightening near the southern root of the filament (the region surrounded by the yellow square in panel (a)), as can be seen in extended image in panel (a), and it started from 10:10 UT on 2012 July 2. Louis et al. [2014] pointed out that magnetic flux cancellation occurred in the region from 10:11 UT to 10:42 UT. The brightening region gradually extended (as seen in panel (b)), and the C2.9 flare occurred at 10:33 UT (panel (c)). The flare

ribbons of the C2.9 flare were also complicated as seen in panel (d). The M5.6 flare started at 10:43 UT (panel (e)) from the slightly northwest region of the C-class flare region, and then, the two clear ribbons appeared at the latter phase (panel (f)). The filament seemed to start eruption between 10:42 - 10:43 UT, but it was difficult to distinguish whether the C2.9 flare or the filament eruption began earlier.
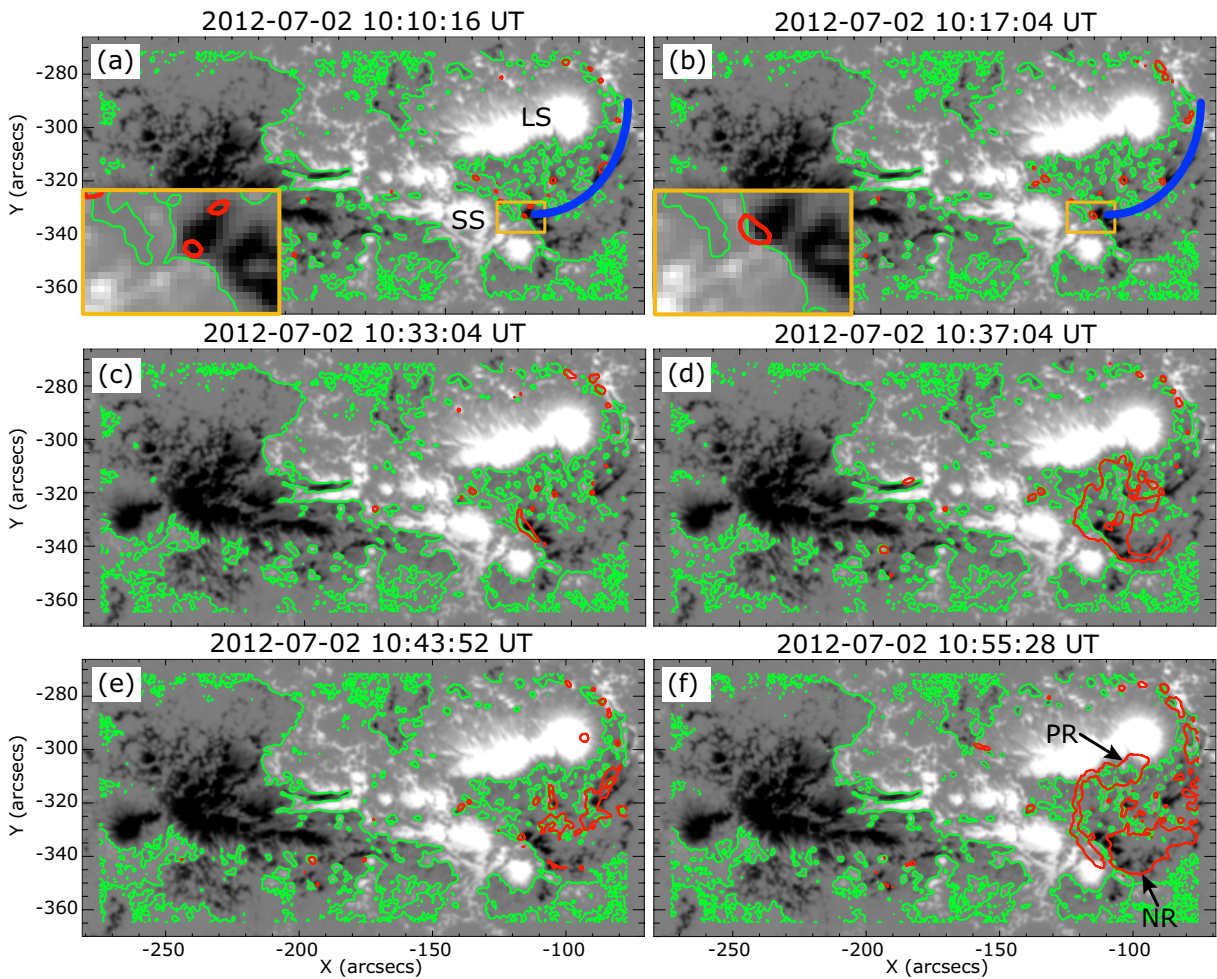
Figure 4.19: Time series of HMI LOS magnetogram for M5.6 flare in AR 11515. Grayscale indicates the LOS magnetic field at $\pm$ 1000 G, and green and red lines outline the PIL and the strong brightenings in AIA 1600 Å images with an intensity of 2000 DN. The extended images of the regions, surrounded by the yellow rectangles, are displayed in panels (a, b). The blue arc roughly represents the filament shape in the Hα images in Louis et al. [2014].
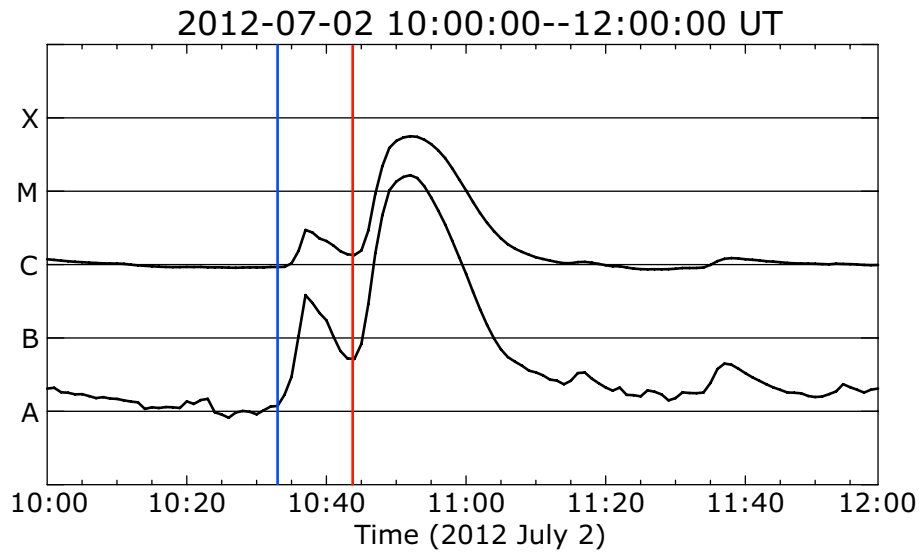
Figure 4.20: The soft X-ray light curve observed by GOES (1 - 8 Å and 0.5 - 4 Å) from 10:00 UT to 12:00 UT on 2012 July 2. The blue/red vertical line indicates the onset time of the C2.9 (10:33 UT)/M5.6 (10:43 UT) flare, respectively.
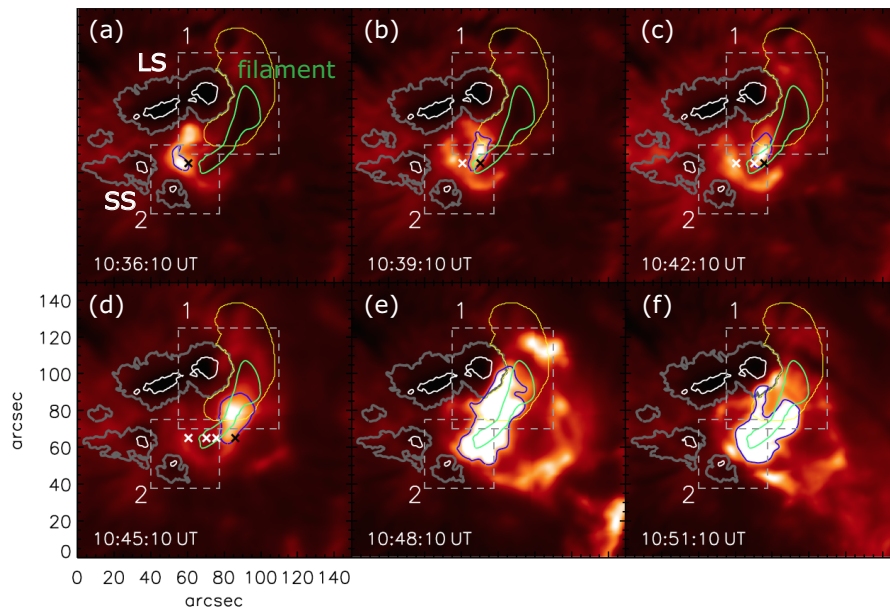
Figure 4.21: Time series of Hα images for M5.6 flare (reprinted from Louis et al. [2014]). The green and blue contours outline the filament and strong brightenings, respectively. The white and grey contours correspond to the sunspot umbra-penumbra and penumbra-quiet Sun boundary, respectively. The black and white crosses indicate the position of the leading edge of the brightness front in the current and previous frames, respectively.

113

Figure 4.21 shows the temporal evolution of the Hα images, which were reprinted from Louis et al. [2014]. These are extended images of the region around the LS and the SS, and the white/grey contour corresponds to the sunspot umbra-penumbra/penumbra-quiet Sun boundary. The green and blue contours outline the filament and strong brightenings, respectively, and the black/white crosses indicate the position of the leading edge of the brightness front in the current/previous frames. In panel (a), the blue contour outlines the most brightest point in the C2.9 flare ribbon, and it is shaped similar to the strong AIA 1600 Å brightening on the PIL in Figure 4.19 (c). The brightening moved eastward, i.e. to the southern root of the filament (see Figure 4.21 (a - c)). Then, the M5.6 flare started at 10:43 UT (between panels (c, d)) in the slightly western region from the C2.9 flaring site, and the filament erupted southwestward while the brightening enhanced (see panels (e, f)). Therefore, from the Hα observation of Louis et al. [2014], it is suggested that both the filament eruption and the C2.9 flare seem highly correlated to the M5.6 flare generation.

Referring back to Figure 4.19, and we can see the enhanced flare ribbons of the M5.6 flare in panel (f). In this phase, we could distinguish the positive and negative flare ribbons (PR and NR, respectively), and it was clearly sheared. Moreover, the small-scale brightening was on the southern PIL of the small wedge-like structure in the extended image of panel (a). Therefore, we could measure the quantitative flare trigger condition θ_0 and φ_e before the C2.9 flare and eruption onset, assuming that the large-scale magnetic field structure around the SS had not changed. The result of the measurement was $(\theta_0, \varphi_e) = (126°, 351°)$, and this was consistent with the RS-type condition. From this, we interpreted that the M5.6 flare seemed to be triggered by the RS-type magnetic field structure in a three-step process, including the C2.9 flare and the filament eruption.

In Chapter 3, we analyzed the X1.0 flare, which showed three flare ribbons and were triggered in a two-step process from the preceding the C-class flare,

and the event can also be classified into Type-D. In this case, complicated three flare ribbons were caused by the complexity of the magnetic field in which the flare trigger region was away from the flaring PIL. Many of the Type-D events likely relate with complexity of the photospheric magnetic field or chromospheric structures, such as the M5.6 flare in AR 11515 and the X1.0 flare in AR 12192. We further investigated whether the pre-flare brightenings were seen on a PIL in the region where the flare-ribbon appeared. Table 4.6 is the list of the Type-D events and existence of pre-flare brightenings, and pre-flare brighitenings on a PIL were observed in eight events out of the 11 Type-D events. Therefore, there is a high probability that we can identify the flare trigger region for the Type-D events, by precisely analyzing the spatial and temporal relevances between the magnetic field structures, chromospheric structures such as a filament and pre-flare brightenings.

No.	Date	Onset (UT)	Class [1]	AR [2]	Pre-flare Brightenings[3]
2	2011 March 9	23:13	X1.5	11166	Yes
4	2011 September 7	22:32	X1.8	11283	No
9	2013 November 5	22:07	X3.3	11890	Yes
14	2011 August 4	03:41	M9.3	11261	Yes
16	2011 September 8	15:32	M6.7	11283	Yes
20	2012 May 10	04:11	M5.7	11476	No
21	2012 July 2	10:43	M5.6	11515	Yes
23	2012 July 5	11:39	M6.1		Yes
24	2012 November 13	01:58	M6.0	11613	Yes
26	2013 October 24	00:21	M9.3	11877	Yes
30	2014 January 1	18:40	M9.9	11936	No

Table 4.6: The list of Type-D events and their pre-flare responses

---

[1]These are defined from GOES X-ray observation.

[2]NOAA AR number

[3]Pre-flare brightenings were seen in AIA 1600 Å at least two frames (i.e. at least over a period of ~ 1.5 *min.*) from one hour before the flare onset.

4.3.3　Consideration of Type-C Case

In case of Type-C events, the initial flare ribbons were clearly sheared, as seen in the two examples, M6.5 flare in AR 11719 (No. 25 in Table 4.4) and M7.2 flare in AR 11944 (No. 31 in Table 4.4), in Figure 4.22. These events occurred in the relatively magnetically simple region compared to Type-D events. The top two panels (a, d) are HMI magnetograms for each event, in which the contours of the strong brightening in AIA 1600 Å are over plotted. The bottom four images (b, c, e, f) are AIA 1600 Å images with the PIL, and strong emission contours. In panels (a, b) and (d, e), we can see the initial flare ribbons, respectively, and these were enhanced at the almost the same location, as seen in panels (c, f). We could infer that the location of the flare trigger region is at the center of the initial flare ribbons. Actually, there were the characteristic magnetic structures as indicated by the yellow arrows in panels (a, d), although these were very tiny structures. However, no pre-flare brightening was seen in the central region of the sheared flare ribbons, in AIA 1600 Å images, at least from sit hours before the flare onset.

Many of the Type-C events showed the similar behavior that the initial flare ribbons did not widely propagated, and there were characteristic magnetic field structures but it was very tiny or very faint (i.e. very weak magnetic field). In most cases of the Type-C events, the flare ribbons suddenly appeared as bright points, and it enhanced at almost the same location (i.e. it did not widely propagate), as seen in the two events in Figure 4.22. According to the KB12 model, the flare ribbons widely propagate to the outer side while the foot points of the long twisted flux ropes gradually become longer in the OP-type case. In contrast, in the RS-type case, the flare ribbons are enhanced at the same location to the initial flare ribbon. Therefore, the magnetic field structures and the flare ribbons of many of the Type-C events are qualitatively consistent with the RS-type case. However, it is difficult to conclude that these events are consistent

with the KB12 model, because there was no pre-flare brightening that can be a proxy of the internal reconnection (cf. Section 4.1).
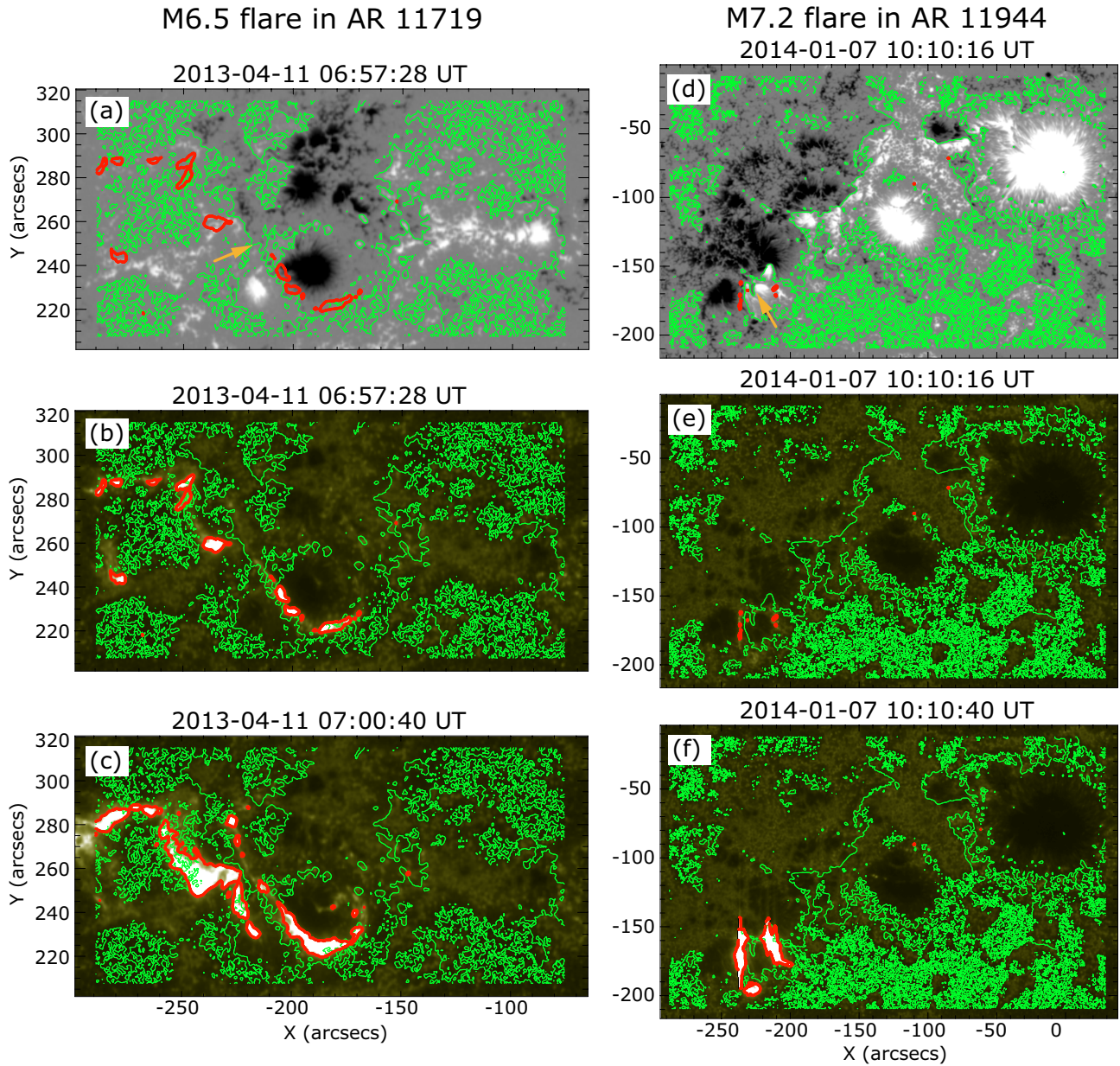
Figure 4.22: Examples of Type-C events. The left and right columns are the M6.5 flare in AR 11719 (No. 25 in Table 4.4) and the M7.2 flare in AR 11944 (No. 31 in Table 4.4), respectively. Top two images (panels (a, d)) are HMI LOS magnetograms at $\pm 1000 G$, in which the contours of the strong brightening ($2000 DN$) in AIA 1600 Å are over plotted. Bottom four images (panels (b, c, e, f)) are AIA 1600 Å images with the PIL and the strong emission contours. The yellow arrows in panels (a, d) indicate the characteristic magnetic field structure which can be a flare trigger region.

Another possibility is that these Type-C events were triggered by a different physical process from the OP- or RS-types. For example, it is conceivable that long twisted flux rope is trapped by the overlying magnetic field and the overlying field is weakened by any cause, such as an emerging flux. This is consistent with the Case-B of Chen & Shibata [2000]. In this case, pre-flare brightening may be seen at the foot point of the overlying field, where may be away from the flaring region. Otherwise, a gradual magnetic flux cancellation at a foot point of the overlying field also may weaken it. In order to examine the possibility, we should confirm the existence of the long twisted flux rope, and should investigate how the flux rope is formed in the AR evolution, using the observational data in high temperature, such as taken by Hinode/XRT.

Therefore, regarding the Type-C events, we can consider the possibility of a different flare trigger process from the OP- or RS-type. However, we did not find out the observed features, which contradict the OP- and the RS-type flare trigger of the KB12 model. We can say the same thing also to the some events of the Type-D, which did not show the pre-flare brightenings, as summarized in Table 4.6. Some extended studies are required to clarify the trigger process of the flare events without pre-flare brightenings.

4.3.4 Difference of the incidence between the OP and RS flare trigger

The statistical investigation in Section 4.3.1 indicated that the OP-type flare trigger is rare compared to the RS-type flare trigger. In fact, in this thesis, we found only two OP-type flare events (Events 1 and 2 analyzed in Chapter 2), whereas 7seven events (including the X1.0 flare analyzed in Chapter 3) were classified into the RS-type. Here, we consider the difference in the incidence between the OP-type and the RS-type flares. One possibility is that the difference is de-

rived from the flexibility of the altitude of internal magnetic reconnection leading to flare reconnection. As was discussed in Section 4.1.4, internal reconnection in the RS-type case is flexible for altitudes, and it can occur more frequently than internal reconnection triggered by the OP-type structure. Another possibility is that the difference corresponds to the displacement of the flare trigger region from the flaring PIL. In Chapter 3, we examined that the RS-type flare trigger could work even if it is located slightly away from the flaring PIL, even though the KB12 model had injected the flare trigger just above the PIL. From the observational results, we here investigated the flexibility of the OP- and RS-type triggers for the displacement from the PIL. The following numerical simulations with different conditions were performed by Dr. Kanya Kusano.

We used the same simulation method and setups as those reported in Kusano & Bamba et al. [2012]. We injected the small bipole field that satisfied the OP or RS condition, and we displaced the bipole field away from the PIL. Figure 4.23 shows the simulation result, and the upper six images and the bottom three images correspond to the OP and the RS cases, respectively. "d" is defined as the distance between the PIL and the small bipole field. For example, $d = 0$ or 0.25 where the center of the small bipole field is located on the PIL or the edge of the positive region, respectively. The result of $d = 0$ cases (left column) are the same as those from the previous simulation in Kusano & Bamba et al. [2012] (Figures 1.10 and 1.11). In case of $d = 0.1$, we slightly displaced the small bipole away from the PIL, and flares were triggered both in the OP and RS cases. Note that the physical processes of the OP-type with the condition of $d = 0.1$ was different from that in case of $d = 0$. The flare reconnection preceded eruption of the twisted flux rope, as in the RS-type flare trigger process, although the normal OP-type ($d = 0$ case) trigger process is "eruption-induced-reconnection". The most noteworthy result is that the OP-type process could not trigger a flare in case of $d = 0.15$, whereas the RS-type process could trigger a flare even in case of $d = 0.2$.

In the OP-type case, the pre-existing large-scale magnetic arcades should be directly reconnected with the flare trigger field, in order to form long twisted flux ropes. Therefore, the twisted flux rope, which will erupt and trigger large-scale flare reconnection, could not form if the small bipole is away from the PIL. Conversely, in the RS-type case, magnetic shear cancellation, i.e. internal magnetic reconnection between the pre-existing magnetic field and the trigger field, can occur as long as the small bipole exists under the pre-existing sheared magnetic arcades. Thus, the large-scale magnetic arcade can collapse and flare reconnection can be triggered by the shear cancellation. However, it is still unclear how a distant field that is away from the PIL can trigger flares in the OP and RS cases on the actual solar surface, and we need to statistically investigate the distance between the flaring PILs and the flare trigger fields using observational data. Even so, the RS-type case is definitely more flexible for displacement of the flare trigger field from the flaring PIL, and thus, more flares can be triggered by the RS-type trigger than that by the OP-type trigger. This is consistent with our statistical classification result in Section 4.3.1.

OP type numerical simuration with offset

| d=0 (flare occurred) | d=0.1 (flare occurred) | d=0.15 (No flare) |

t=8   t=15   t=9

t=23   t=40   t=37

RS type numerical simuration with offset

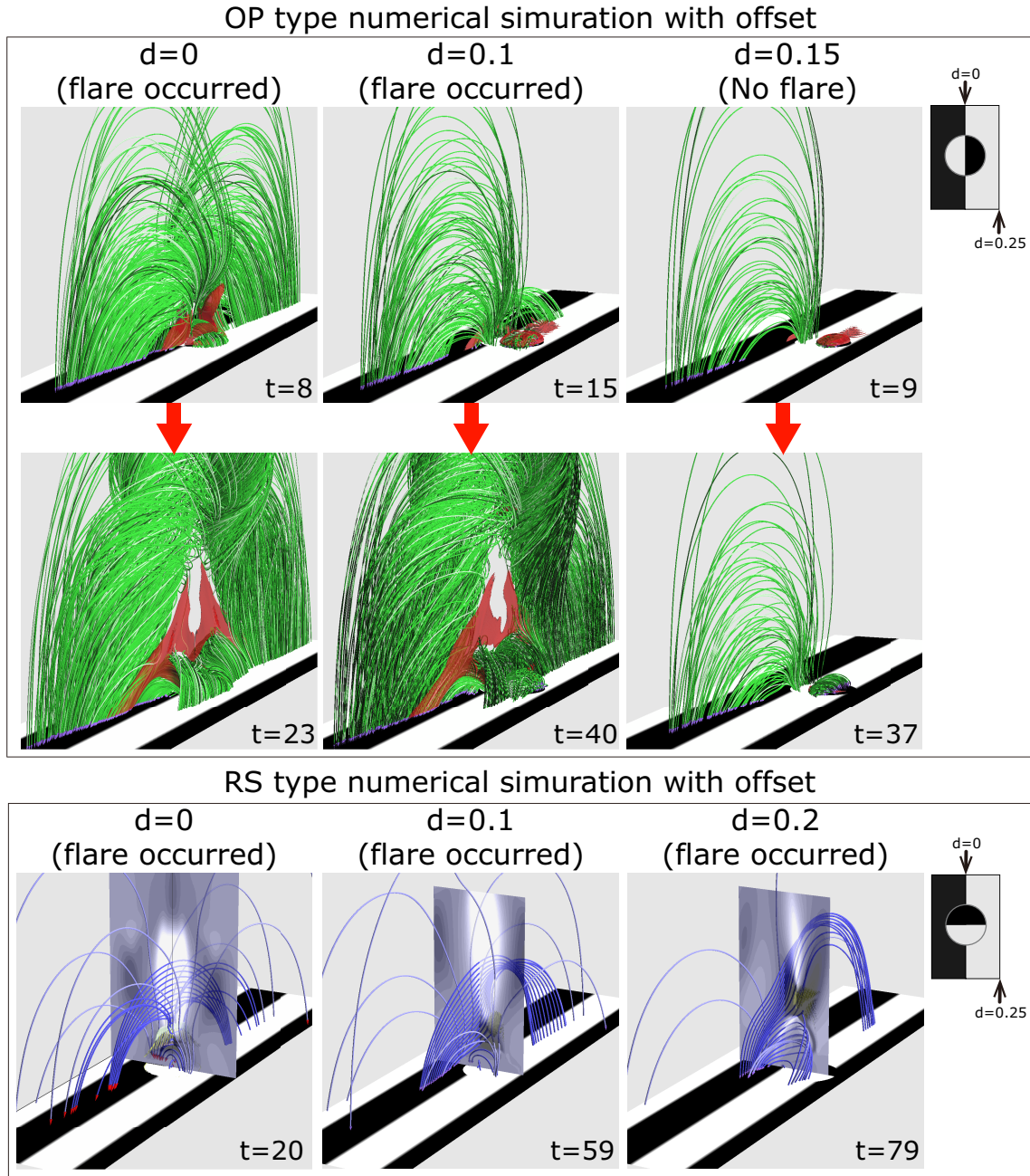| d=0 (flare occurred) | d=0.1 (flare occurred) | d=0.2 (flare occurred) |

t=20   t=59   t=79

Figure 4.23: Images of the numerical simulation of the KB12 model with offset from PIL (performed by Dr. K. Kusano, unpublished data (cf. Kusano & Bamba et al. [2015])). The white/black part corresponds to positive/negative polarity of the LOS magnetic field. We injected the OP- or RS-type small-scale bipole magnetic field on different locations from $d = 0$ (on the PIL) to $d = 0.25$ (on the edge of the positive region). The upper six images show the OP-type case with the condition of $(\theta_0, \varphi_e) = (180°, 77.5°)$. The green tubes represent the magnetic field lines of reconnected magnetic field, and the red contours correspond to strong electric currents produced by magnetic reconnection. The bottom three panels are images of the RS-type case. The blue tubes represent the reconnected magnetic field lines, and the yellow isosurfaces correspond to strong electric currents. The gray scales of the central vertical plane correspond to the released kinetic energy, and the white color represents a large energy release.

Chapter 5

Conclusion and Future Direction

In this thesis, we aimed to examine the flare trigger condition proposed by the KB12 model by comparing the simulation results with actual solar flares observed by Hinode, SDO, and IRIS. We identified the flare trigger regions, and quantitatively measured the triggering conditions for several major flares in Chapters 2 and 3. The flare trigger regions satisfied the geometrical conditions of either the Opposite Polarity or the Reversed Shear types, which are classified by the shear angle θ_0 of a large-scale magnetic arcade and the azimuth angle φ_e of a small-scale flare trigger field. Also, the shapes and timing of the pre-flare brightenings and initial flare ribbons corresponded to the strong electric current sheets formed by magnetic reconnection before and during flares, as the numerical simulation results of the KB12 model. Therefore, our conclusion is that the topological conditions of magnetic field (either OP or RS), which were proposed by the KB12 model, are suitable as the flare trigger condition.

We developed a method to identify the flare trigger region using the initial flare ribbons and the pre-flare brightenings as a proxy. We showed that the flare trigger region can be identified using the method, even in magnetically complicated ARs, such as analyzed in Chapter 3 and the Type-D events in Section 4.3.2. Moreover, using our method, which divide the magnetic field structure in the flaring AR into large- and small-scale structures, we are able to measure the

two parameters θ_0 and φ_e. Our results suggest that to evaluate the quantitative values of the parameters (θ_0, φ_e) and their combinations is significant, also from the perspective of an application for flare forecasting.

In Section 4.2, we discussed the possibility of an additional parameter for flare triggering in order to consider why flares occur at specific time. We proposed that the "total magnetic flux" contained in the flare trigger field contributes to the critical conditions for flare triggering. We quantitatively investigated the temporal evolution of the total magnetic flux in the flare trigger region, and we found that the total magnetic flux clearly increased from several hours before to the flare onset time in both OP and RS cases. Therefore, our hypothesis, that both the geometrical condition of (θ_0, φ_e) and the "total magnetic flux" contained in the flare trigger field were critical for flare triggering, is feasible. It is inferred that the critical fluxes required to trigger instability depends on the proximity of the system to an unstable state, and it likely changes during the AR evolution. An extended statistical study is required to elucidate the factors underlying the critical fluxes of flare trigger fields.

We found that the RS-type flare trigger could work even if it is located slightly away from the PIL, in Chapter 3. Led by our analysis result, the numerical simulation of the KB12 model was performed afresh with the displacement of the small bipole from the PIL in Section 4.3.4. The simulation showed that the RS-type flare trigger field is more flexible for the displacement from PIL than the OP-type trigger. This is caused by the difference of the physical process among the OP- and RS-types, leading the internal magnetic reconnection via the flare trigger field. This was consistent with the trend of the statistical classification that more events were classified into the RS-type rather than OP-type. However, it is still unclear how distant field away from the PIL is able to trigger flares in each OP and RS cases on the actual solar surface. We need to statistically investigate the distance between the flaring PILs and the flare trigger fields using observational data.

From the statistical classification in Section 4.3, we found many events which did not show the important features to identify the flare trigger region. In some cases, it was difficult to estimate the flare trigger region, because the initial flare ribbons had very complicated shapes. Even in these cases, we identified the flare trigger region by carefully analyzing the spatial and temporal relationship between magnetic field, pre-flare brightening, filament structure, and another flare event in the same region. We believe that we are able to understand the triggering process regardless of the complexity of the flare ribbons provided that the pre-flare brightenings are seen in the flaring region. However, there were some events which did not show any pre-flare brightening in the flaring region. Some of these events were interpretable by the KB12 model, from the features of time evolutions of flare ribbons and magnetic structures. However, other models, such as emerging flux model and kink mode destabilization model, also can explain these events. Therefore, we need to consider the possibility of other flare trigger process, although we did not find out the observed features which contradict the OP- and the RS-type flare trigger of the KB12 model. Some extended studies are required to clarify the trigger process of the flare events without pre-flare brightenings.

In the KB12 model, the sheared magnetic field, which stored magnetic free energy, goes into feedback process of magnetic reconnection and instability by any disturbances (P1 in Figure 5.1). In this thesis, we considered OP- or RS-type small-scale bipole magnetic field as a disturbance. However, there are some flares and/or CMEs sometimes occur in the region that is almost a quiet region, mostly related to filament eruption. In these cases, we need to consider also different disturbance(s) and other physical process, in which the system voluntarily becomes unstable without any triggers. Some theoretical model based on numerical simulations, in which the magnetic flux ropes are strongly twisted and destabilized by photospheric horizontal motion, have been proposed as mentioned in Section 1.2 (Fan & Gibson [2003]; Török & Kliem [2005]). Furthermore, it is still

unclear what generates solar explosive/eruptive phenomena from the feedback process in Figure 5.1 P2. X-class flares are often associated with CMEs as reported in Yashiro et al. [2006], but they do not occur together every time. The feedback process of the KB12 model can also explain the mutual relationship between flares and CMEs without regard to order, but we now do not have the parameter(s) that determine the generation of flares and/or CMEs. The decay index $n = -d(ln\ B_{am})/d(ln\ R)$ of the ambient magnetic field B_{am} is used to evaluate the equilibrium state of the magnetic flux rope of major radius R, and flux rope can erupt when n reaches the critical range 1.3 - 1.5 (Kliem & Török [2006]; Zuccarello et al. [2015]). However, the critical value of the decay index is different among different MHD simulations. From the perspective of space weather forecast, it is important to find out the observable parameters and the combinations of their quantitative values that determine the generation of flares and/or CMEs.

Even so, we considered that the KB12 model can explain the fundamental physical process in a multitude of solar flares. The parameters θ_0 and φ_e can be suitable parameters for flare forecast, although it seems that other parameters should be considered to predict a variety of explosive/eruptive phenomena on the solar surface. It is expected in the near future that the suitable parameters and the combinations of their values will be determined using the KB12 model for practicable space weather forecast.
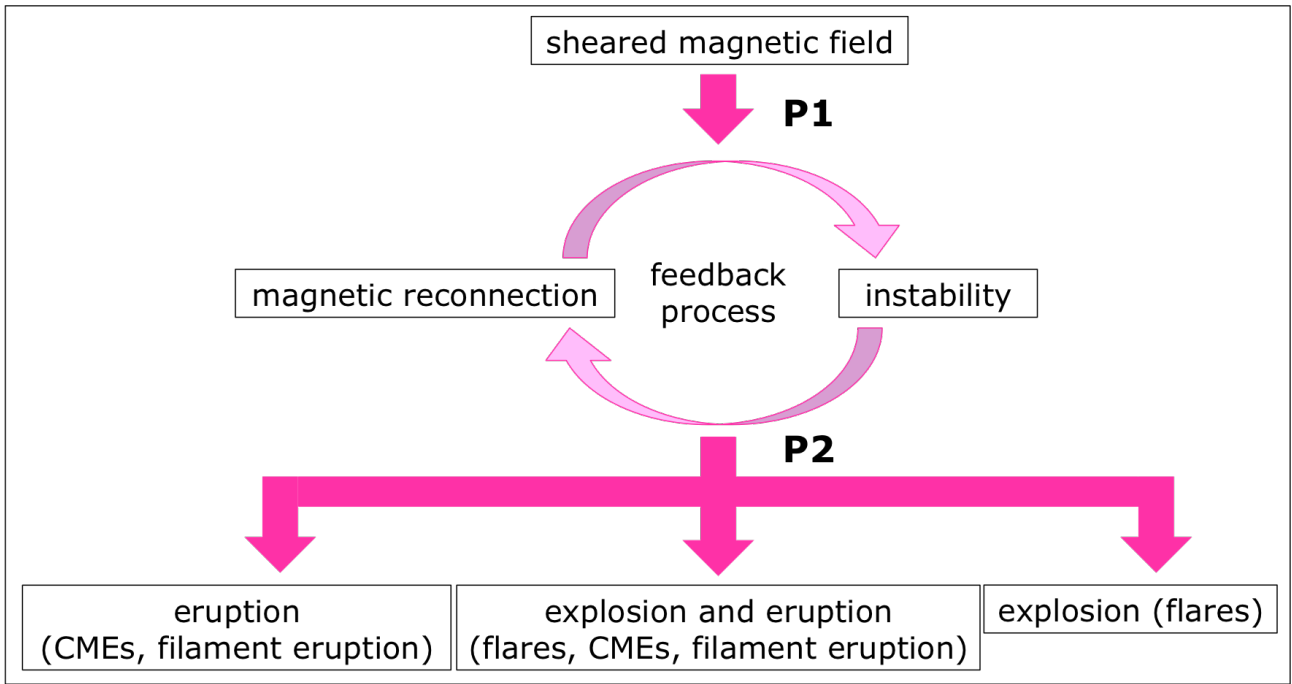
Figure 5.1: Chart illustrating physical process from the sheared magnetic field to solar explosive and/or eruptive phenomena.

References

Aly, J. J. 1991, *ApJL*, 375, L61

Antiochos, S. K., DeVore, C. R., & Klimchuk, J. A. 1999, *ApJ*, 510, 485

Antonucci, E., Gabriel, A. H., Acton, L. W., et al. 1982, *Solar Phys.*, 78, 107

Antonucci, E., Gabriel, A. H., & Dennis, B. R. 1984, *ApJ*, 287, 917

Baker, D. N., Li, X., Pulkkinen, A., Ngwira, C. M., Mays, M.L., Galvin, A. B., & Simunac, K. D. C., *Space Weather*, 2013, 11, 585

Bamba, Y., Kusano, K., Yamamoto, T. T., & Okamoto, T. J. 2013, *ApJ*, 778, 48

Bamba, Y., Kusano, K., Imada, S., & Iida, Y. 2014, *PASJ*, 66, S16

Carrington, R. C. 1859, *MNRAS*, 20, 13

Carmichael, H. 1964, NASA Special Publication, 50, 451

Chen, P. F., & Shibata, K. 2000, *ApJ*, 545, 524

De Pontieu, B., Title, A. M., Lemen, J. R., et al. 2014, *Solar Phys.*, 289, 2733

Fan, Y., & Gibson, S. E. 2003, *ApJL*, 589, L105

Hagyard, M. J., Teuber, D., West, E. A., & Smith, J. B. 1984, *Solar Phys.*, 91, 115

Hale, G. E. 1908, *ApJ*, 28, 315

Heyvaerts, J., Priest, E. R., & Rust, D. M. 1977, *ApJ*, 216, 123

Hirayama, T. 1974, *Solar Phys.*, 34, 323

Hodgson, R. 1859, *MNRAS*, 20, 15

Ichimoto, K., Lites, B., Elmore, D., et al. 2008, *Solar Phys.*, 249, 233

Inoue, S., Magara, T., Pandey, V. S., et al. 2014, *ApJ*, 780, 101

Jing, J., Park, S.-H., Liu, C., et al. 2012, *ApJL*, 752, L9

Kaiser, M. L. 2005, *Advances in Space Research*, 36, 1483

Kentischer, T. J., Bethge, C., Elmore, D. F., et al. 2008, *SPIE*, 7014, 701413

Kippenhahn, R., & Schlüter, A. 1957, *ZAp*, 43, 36

Kliem, B., Török, T. 2006, *Physical Review Letters*, 96, 255002

Kosugi, T., Matsuzaki, K., Sakao, T., et al. 2007, *Solar Phys.*, 243, 3

Kopp, R. A., & Pneuman, G. W. 1976, *Solar Phys.*, 50, 85

Kubo, M., Yokoyama, T., Katsukawa, Y., et al. 2007, *PASJ*, 59, 779

Kusano, K., Maeshiro, T., Yokoyama, T., & Sakurai, T. 2004, *ApJ*, 610, 537

Kusano, K., Bamba, Y., Yamamoto, T. T., et al. 2012, *ApJ*, 760, 31

Kusano, K., Bamba, Y., and Shiota, D., 2015, *Spring Meeting of the Astronomical Society of Japan*, M16b

Landi, E., Del Zanna, G., Young, P. R., Dere, K. P., & Mason, H. E. 2012, *ApJ*, 744, 99

Leka, K. D., Barnes, G., Crouch, A. D., et al. 2009, *Solar Phys.*, 260, 83

Leka, K. D., Barnes, G., Gary, G. A., Crouch, A. D., & Liu, Y. 2012, *Solar Phys.*, 276, 441

Lemen, J. R., Title, A. M., Akin, D. J., et al. 2012, *Solar Phys.*, 275, 17

Lites, B. W., Low, B. C., Martinez Pillet, V., et al. 1995, *ApJ*, 446, 877

Lites, B. W., Akin, D. L., Card, G., et al. 2013, *Solar Phys.*, 283, 579

Lites, B. W., & Ichimoto, K. 2013, *Solar Phys.*, 283, 601

Lin, R. P., Dennis, B. R., Hurford, G. J., et al. 2002, *Solar Phys.*, 210, 3

Liu, C., Deng, N., Liu, R., et al. 2012, *ApJL*, 745, L4

Louis, R. E., Puschmann, K. G., Kliem, B., Balthasar, H., & Denker, C. 2014, *A&A*, 562, A110

Masuda, S., Kosugi, T., Hara, H., Tsuneta, S., & Ogawara, Y. 1994, *Nature*, 371, 495

Metcalf, T. R. 1994, *Solar Phys.*, 155, 235

Moore, R. L., Sterling, A. C., Hudson, H. S., & Lemen, J. R. 2001, *ApJ*, 552, 833

Ogawara, Y., Acton, L. W., Bentley, R. D., et al. 1992, *PASJ*, 44, L41

Ohyama, M., & Shibata, K. 1998, *ApJ*, 499, 934

Pesnell, W. D., Thompson, B. J., & Chamberlin, P. C. 2012, *Solar Phys.*, 275, 3

Rust, D. M., & Kumar, A. 1996, *ApJL*, 464, L199

Schou, J., Scherrer, P. H., Bush, R. I., et al. 2012, *Solar Phys.*, 275, 229

Schou, J., Borrero, J. M., Norton, A. A., et al. 2012, *Solar Phys.*, 275, 327

Shimizu, T., Katsukawa, Y., Matsuzaki, K., et al. 2007, *PASJ*, 59, 845

Shimizu, T., Nagata, S., Tsuneta, S., et al. 2008, *Solar Phys.*, 249, 221

Shiota, D., Isobe, H., Chen, P. F., et al. 2005, *ApJ*, 634, 663

Socker, D. G., Howard, R. A., Korendyke, C. M., Simnett, G. M., & Webb, D. F. 2000, *PROCSPIE*, 4139, 284

Sturrock, P. A. 1966, *Nature*, 211, 695

Sturrock, P. A. 1991, *ApJ*, 380, 655

Su, Y., Golub, L., van Ballegooijen, A., et al. 2007, *PASJ*, 59, 785

Suematsu, Y., Tsuneta, S., Ichimoto, K., et al. 2008, *Solar Phys.*, 249, 197

Tanaka, Y. 1983, *Solar Phys.*, 86, 3

Toriumi, S., Iida, Y., Bamba, Y., et al. 2013, *ApJ*, 773, 128

Török, T., & Kliem, B. 2005, *ApJ*, 630, L97

Tsuneta, S., Hara, H., Shimizu, T., et al. 1992, *PASJ*, 44, L63

Tsuneta, S., Ichimoto, K., Katsukawa, Y., et al. 2008, *Solar Phys.*, 249, 167

Wang, S., Liu, C., Liu, R., et al. 2012, *ApJL*, 745, L17

Watanabe, K., Krucker, S., Hudson, H., et al. 2010, *ApJ*, 715, 651

Watanabe, K., Masuda, S., & Segawa, T. 2012, *Solar Phys.*, 279, 317

Yashiro, S., Akiyama, S., Gopalswamy, N., & Howard, R. A. 2006, *ApJL*, 650, L143

Yokoyama, T., & Shibata, K. 1995, *Nature*, 375, 42

Yokoyama, T., & Shibata, K. 1996, *PASJ*, 48, 353

Yokoyama, T., Akita, K., Morimoto, T., Inoue, K., & Newmark, J. 2001, *ApJL*, 546, L69

Zuccarello, F. P., Aulanier, G., & Gilchrist, S. A. 2015, *ApJ*, 814, 126

Publications

Kusano, K., **Bamba, Y.**, Yamamoto, T., T., Iida, Y., Toriumi, S., & Asai, A. (2012), "Magnetic Field Structures Triggering Solar Flares and Coronal Mass Ejections", *ApJ*, 760, 31

Bamba, Y., Kusano, K., Yamamoto, T. T., & Okamoto, T. J. (2013), "Study on the Triggering Process of Solar Flares based on Hinode/SOT Observations", *ApJ*, 778, 48

Bamba, Y., Kusano, K., Imada, S., & Iida, Y. (2014), "Comparison between Hinode/SOT and SDO/HMI, AIA data for the study of the solar flare trigger process", *PASJ*, 66, S16

Bamba, Y., Kusano, K., Inoue, S., & Shiota, D., "Two-step Triggering Process of the X1.0 Three-ribbons Flare in the Great Active Region NOAA 12192", submitted to *ApJ*